Constraining Microwave Emission from Extensive Air Showers via the MIDAS Experiment

By

Matthew Douglas Richardson

Dissertation

Submitted to the Faculty of the

Graduate School of Vanderbilt University

in partial fulfillment of the requirements

for the degree of

DOCTOR OF PHILOSOPHY

in

PHYSICS

May 2017

Nashville, Tennessee

Approved:

Andreas Berlind, Ph.D.

Paolo Privitera, Ph.D.

Kelly Holley-Bockelmann, Ph.D.

Keivan Stassun, Ph.D.

Thomas Weiler, Ph.D.

DEDICATION

To my mother, whose love, support, and steady hands navigated me through the turbulent waters of early life and set me on a path of prosperity.

To my grandmother, whose love, prayers, and words of wisdom served as beacons of hope during dreary times.

To my sister, whose, love, support, and advice kept me leveled minded during times of emotional distress.

To my wife and children, whose unwavering love, constant support, astounding patience, and encouragement have been vital to my professional development and personal growth.

ACKNOWLEDGMENTS

This work has been made possible by funding from the National Science Foundation, and utilizes data acquired by the Pierre Auger Laboratory.

I am grateful to the Fisk-Vanderbilt Bridge Program for not only giving me the opportunity to turn my dream of attaining a Ph.D. in astrophysics into reality, but also providing me with the basic skills required to be a good researcher.

I would like to express my highest gratitude and respect for both Dr. Keivan Stassun and Dr. Andreas Berlind whose instruction and advise have been instrumental in helping me hone my research skills while also helping me find balance between work and family.

Lastly, I would like to acknowledge the Vanderbilt astronomy department. Whether it was sitting through one of my astronomy journal club presentations, listening to me stumble through explaining my research during a group meeting, or taking the time to have a conversation, I would like to thank the entire Vanderbilt astronomy department for helping me on my journey to obtaining my Ph.D.

TABLE OF CONTENTS

LIST OF FIGURES

CHAPTER 1

INTRODUCTION: COSMIC RAYS

Cosmic rays are energetic charged particles that originate from high energy processes in the universe. The cosmic ray energy spectrum, Figure 1.1, as determined by several experiments, indicates that these particles exhibit kinetic energies over several orders of magnitude, including energies that exceed 10^{20} eV (100 EeV, 1 EeV = 10^{18} eV). The observed energy range and features seen in the cosmic ray energy spectrum has raised many questions, some of which have been answered and others that are still a mystery.

The spectrum can essentially be divided into three sections based on cosmic ray origin. The lowest energy cosmic rays are attributed to solar processes and are commonly referred to as solar energetic particles. Typical kinetic energies for these types of cosmic rays range from 10^7 to 10^8 eV, but can reach energies as high as 10^9 to 10^{10} eV (Sharma (2008), chapter 18). The intermediate energy cosmic rays are of galactic origin beyond the solar system, and have been shown to be byproducts of processes occurring within supernovae remnants (Ackermann *et al.* (2013)); however, it is unclear if supernovae remnants are the only source of galactic cosmic rays. While galactic cosmic rays may have energies as low as 10^9 eV, these low energy galactic cosmic rays experience significant deflections due to the Sun's magnetic field as well as interplanetary magnetic fields resulting in many never reaching Earth's atmosphere. In the spectrum around 3×10^{15} eV there is a break in the power law, referred to as the "knee" in Figure 1.1, that is thought to be a consequence of typical supernovae remnant acceleration limitations (Beatty and Westerhoff (2009)). Cosmic rays that exhibit energies in the region between the so-called "knee" and "ankle" in Figure 1.1 are considered to be of either Galactic or extragalactic origin. The highest energy cosmic rays, known as the ultra high-energy cosmic rays (UHECRs) and the focus

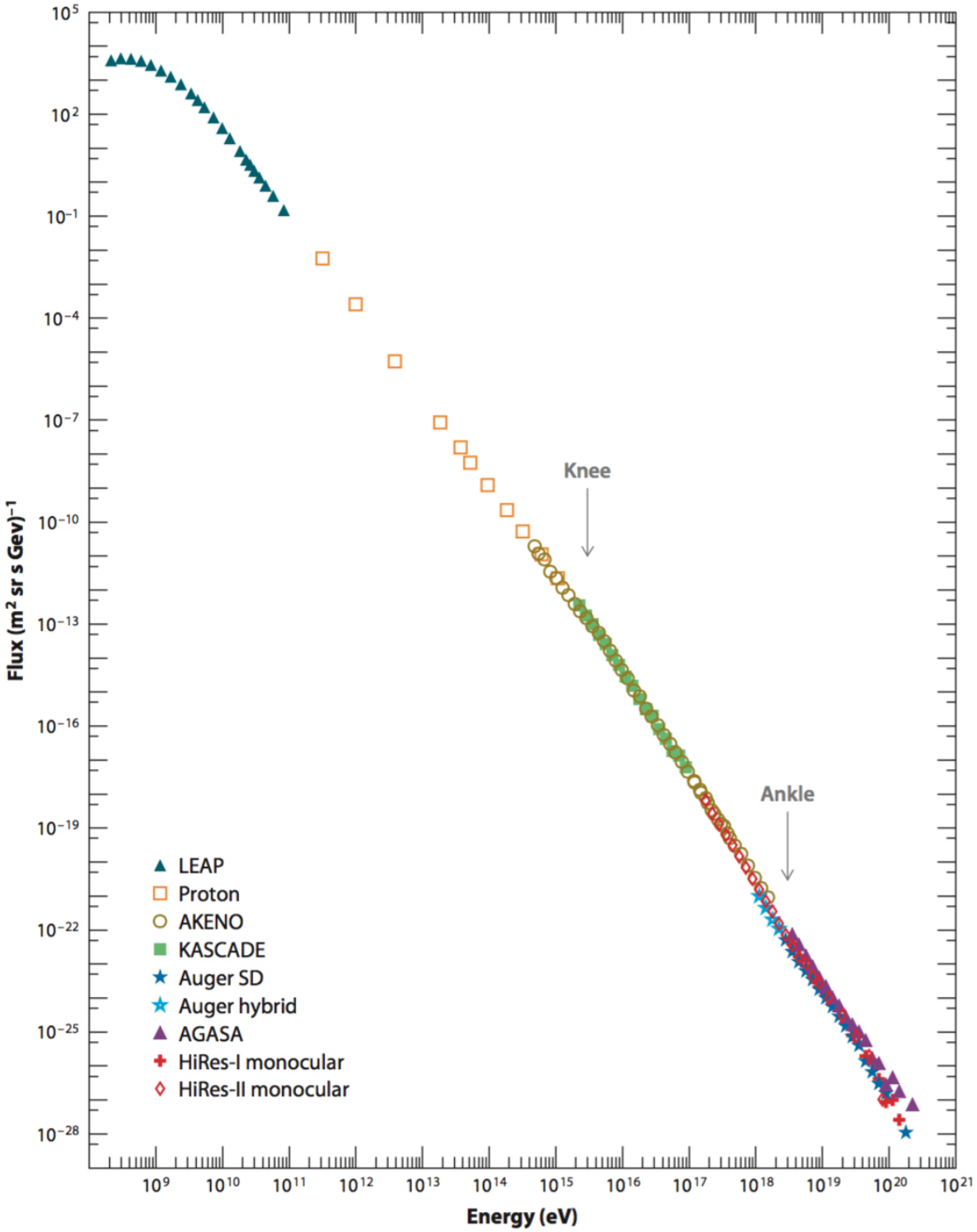

Figure 1.1: The cosmic ray energy spectrum. Approximate energies of the breaks in the spectrum, the "knee" and "ankle", are indicated by arrows. Data are from LEAP, Proton, AKENO, KASCADE, Auger surface detector, Auger hybrid, AGASA, HiRes-I monocular, and HiRes-II monocular. LEAP proton-only data has been scaled to the all-particle spectrum. Figure acquired from Beatty and Westerhoff (2009). See references therein for description of data sets.

of our work, are believed to be of extragalactic origin, and have energies beyond 10^{18} eV. As a result of the highly infrequent detection of these particles, with a flux on the order of 1 particle per km^2 per century near 10^{19} eV, we know little about them. In particular, we know very little about the astrophysical processes that impart energy to, i.e. accelerate, these highly energetic particles, and exactly where these processes occur in the universe.

In this thesis, a brief review on the origin, propagation, air shower development, detection, and anisotropy of the UHECRs is given in § 1. In § 2, the theory of microwave emission from extensive air showers is discussed. In § 3, we discuss the Microwave Detection of Air Shower experiment and its role in characterizing microwave emission from extensive air showers. In § 4, . Lastly, a summary and outlook for the field of cosmic ray research is given in § 5.

1.1 Ultra High Energy Cosmic Rays Astrophysical Sources

At energies greater than 10^{18} eV, the energetics of cosmic rays become comparable to the energetics of macroscopic objects, e.g. a 3×10^{20} eV cosmic ray has the same kinetic energy as a football moving at a speed of 53 km h^{-1} (33 mph). This naturally implies that the astrophysical source must not only be an extremely energetic event, but, more importantly, have an acceleration mechanism whose relevant physics is plausible. There exists an argument formulated by Hillas (1984) that imposes a restriction on the possible source candidates capable of accelerating UHECRs. The condition requires that the physical size of the accelerating region, of source radius r_s, be at least as large as the orbit, the gyration radius r_g, established by a particle confined by a typical magnetic field:

$$r_g = \frac{E}{cqB_\perp} \leq r_s, \tag{1.1}$$

where E is the energy of the cosmic ray, c is the speed of light, q is the charge of the cosmic ray, and $B_\perp$ is the magnetic field component perpendicular to the cosmic ray's momentum.

The charge of the cosmic ray may be given by q = Ze (Z and e are the atomic number and electron charge, respectively). Therefore, the maximum energy that can be obtained by the cosmic ray is

$$E_{max} = cZeB_{\perp}r_s, \tag{1.2}$$

and is known as the Hillas criterion.

Although Eq. 1.2 is a theoretical point of view, it offers a simple line of logic for determining possible sources of UHECRs; we may assume that the maximum energy of the cosmic ray can be confined by an acceleration site having the right combination of physical size, r_s, and magnetic field, B, that yield a product that satisfies Eq. 1.2. In Figure 1.2 we see that few astrophysical sources meet the conditions necessary for acceleration of protons up to 10^{20} eV (top diagonal line in Figure 1.2). While the Hillas criterion is a requirement that must be satisfied, it is not enough to describe the acceleration mechanism that achieves the observed energy spectrum for UHECRs (Kotera and Olinto, 2011). In general, the acceleration mechanism must adequately account for the geometry of the source (Hillas criterion), energy losses that occur during acceleration, accompanying radiation produced during acceleration, while also yielding the observed power laws obtained after propagation (Ptitsyna and Troitsky, 2010).

One particular theoretical mechanism for accelerating cosmic rays was proposed by Fermi (1949). Commonly known as the second-order Fermi acceleration, the theory is described by a charged particle entering a magnetized interstellar cloud, moving at a velocity v, and interacting with the random motions of the cloud's internal magnetic field. The randomly oriented magnetic fields will essentially act like "magnetic mirrors" causing the particle to "reflect" upon interaction. Particle acceleration will occur if the magnetic mirror is advancing towards the particle, and deceleration will occur if the mirror is receding. Fermi argued that on average, taking into consideration all the interactions between the

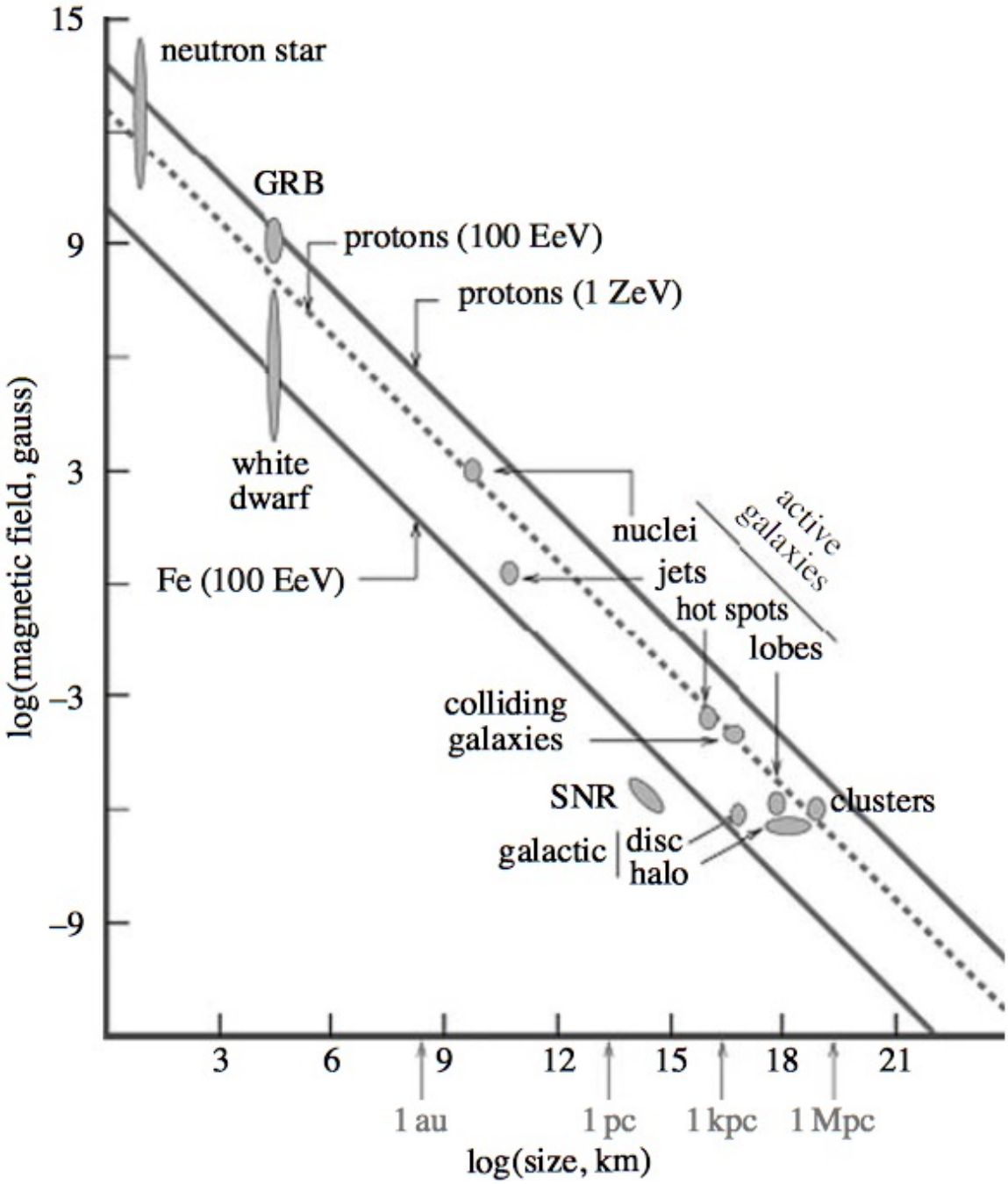

Figure 1.2: The Hillas plot showing magnetic field versus size of astrophysical objects. The diagonal lines represent lines of constant energy, E_{max}, satisfying Hillas's criterion for an iron nuclei (Z = 26) and two protons (Z = 1) of different energy. Note that the region above any given line corresponds to B-R phase space capable of confining a cosmic ray of charge Z and energy E_{max}. Figure acquired from Fraschetti (2008).

particle and mirrors, the particle will have been accelerated upon leaving the cloud. The average energy gained per collision is given by $<\Delta E/E> \sim \beta^2$, where β is the velocity of the cloud in terms of the speed of light c.

Although the second-order acceleration mechanism yields a power law, $N(E) \sim E^{-\gamma}$, the energetics of the second-order Fermi mechanism are too slow to accelerate high energy cosmic rays, i.e. the time required to significantly accelerate a cosmic ray greatly exceeds the average lifetime, 15 ± 1.6 Myr (Lipari, 2014), of a cosmic ray. This is due to small gains in energy by the charged particle and a low interaction rate between the charged particle and magnetic clouds. However, diffusive shock acceleration, referred to as the first-order Fermi acceleration, is more efficient than the second-order mechanism. The average energy gained is given by $<\Delta E/E> \sim \beta$, where β is the shock velocity, the environments, like that of a supernova shock, yields interactions in which all "collisions" between the magnetic mirrors and the particle are head-on (Fraschetti (2008)). This particular scenario is favored for the acceleration of galactic cosmic rays, but appears to encounter problems in accelerating cosmic rays to the highest energies that have been observed.

Studies have been done to test the feasibility of accelerating protons to energies corresponding to the UHECRs in the vicinity of neutron stars, AGN, and radio galaxies (see e.g. Fraschetti and Melia (2008), Rieger (2008), Kotera and Olinto (2011), and Bhattacharjee and Sigl (2000) and references therein). Neutron stars appear to be poor acceleration sites of UHECRs due to synchrotron losses and GZK-like photo reaction losses while attempting to accelerate the cosmic ray. The environment surrounding AGN is not conducive to the propagation of UHECRs, even though AGN appear to be capable of accelerating protons to the energy regime of UHECRs. Hot-spots of radio galaxies, however, meet the physical requirement, imposed by Hillas's criterion, and energetic requirements to produce UHECRs. The only concerns with radio-galaxies as sources is their location. Due to the GZK effect, as explained in § 1.2.2, the particles would not survive the trip from their source to Earth. This is due to a spacial correlation between the observed UHECRs and radio galaxies at

distances >100 Mpc. At the moment, it is still unclear where the UHECRs originate.

1.2 Ultra High Energy Cosmic Ray Propagation

While propagating through the vast space of the interstellar and intergalactic mediums, UHECRs past by a variety of stars, gas and dust, and other interstellar objects. Due to the travel speed of UHECRs and the relatively low density of the majority of the objects that are "seen" during their journey, there is very little to no chance of interaction. However, UHECRs do interact with intergalactic and interstellar magnetic fields and the cosmic microwave background (CMB).

1.2.1 Interaction with Intergalactic and Interstellar Magnetic Fields

Figure 1.3 shows the deflection of a charged particle in a uniform magnetic field. From the schematic we may derive the following formula

$$\sin\theta = \frac{L_{eff}}{r_g} \tag{1.3}$$

where θ is the angle of deflection, L_{eff} is the linear length over which the charged particle, the cosmic ray, interacts with the uniform magnetic field, B, and r_g is the gyration radius (see Eq. 1.1). In the case where the angle of deflection is small, which is generally true at energies corresponding to UHECRs, we may approximate the angle of deflection using the small angle approximation

$$\Delta\theta \simeq \frac{L_{eff}}{r_g} = \frac{cZeL_{eff}B_{\perp}}{E}. \tag{1.4}$$

The magnetic field strength of the interstellar and intergalactic medium are taken to be $\sim 10^{-6}$ and $\sim 10^{-9}$ with coherence lengths of $\sim$ 100 pc and $\simeq$ 1 Mpc, respectively (Elyiv and Hnatyk (2004) and Achterberg *et al.* (1999)). In light of this knowledge coupled with

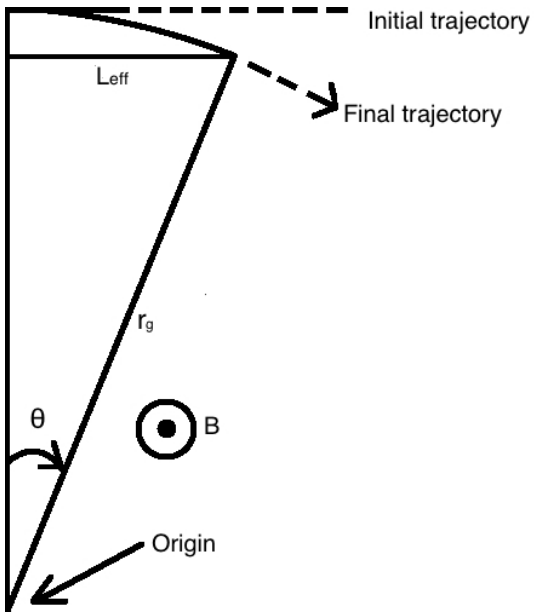

Figure 1.3: Deflection of a charged particle due to interaction with a uniform magnetic field.

Eq. 1.4, we obtain the following for deflection of UHECRs in the intergalactic medium

$$\Delta\theta_{\rm IGM} \approx 0.5^\circ Z \left(\frac{E}{10^{20}\ {\rm eV}}\right)^{-1} \left(\frac{\rm L_{eff}}{1\ {\rm Mpc}}\right) \left(\frac{\rm B_\perp}{10^{-9}\ {\rm G}}\right). \tag{1.5}$$

Deflection due to the Galactic field under the assumptions stated above (i.e. $\rm L_{eff}$ = 100 pc and $\rm B_\perp = 10^{-6}$ G) for a proton with energy 10^{20} eV yields a deflection $\Delta\theta_{\rm ISM} \approx 0.05^\circ$. With such small deflections expected within the Galaxy, UHECR sources within the Galaxy should yield detections that are clustered on the sky in the direction of the Galactic center. However, this is not the case as the highest energy cosmic rays appear to come from sources away from the Galactic center and are not as clustered as one would expect under the condition of Galactic sources. For this reason, UHECRs are generally believed to be of extragalactic origin.

Another important aspect of the interaction between the UHECRs and magnetic fields is the time delay it imposes on cosmic rays traveling from their source to Earth. The time

delay is given by

$$t_{delay} = \frac{1}{v}(s - L_{eff}) \tag{1.6}$$

where v is the velocity of the cosmic ray ($v \sim c$), s is the path length of the arc traversed by the cosmic ray, and L_{eff} represents the ballistic path the cosmic ray would have traveled if uninfluenced by the magnetic field. For small angles ($s << r_g$), we obtain

$$t_{delay} = \frac{1}{24c}\frac{L_{eff}^3}{r_g^2} = \frac{c}{24}\frac{q^2 B_\perp^2 L_{eff}^3}{E^2} \tag{1.7}$$

The angular deflection and time delay due to interactions with interstellar and intergalactic magnetic fields are important concepts that must be taken into consideration when performing detailed studies of possible UHECR sources.

1.2.2 Interaction with Cosmic Microwave Background

Through interactions with the photons of the CMB, cosmic rays can suffer significant energy losses. For heavy nuclei, i.e. $Z > 1$, nuclear photo-disintegration occurs, a process in which a heavy atomic nucleus absorbs a photon causing the nucleus to go into an excited state and immediately decay through the emission of a subatomic particle. This process yields energy losses comparable to photo-pion production of cosmic ray protons (Beatty and Westerhoff, 2009)) explained below. At the highest cosmic ray energies, and assuming the primary particle is a proton, there are primarily two mechanism responsible for energy attenuation: pair production and photo-pion production.

At cosmic ray proton energies no lower than 2.1×10^{18} eV, the pair production threshold energy has been attained and the creation of electron-positron pairs becomes possible

through the interaction between a cosmic ray proton and CMB photon

$$p + \gamma_{CMB} \rightarrow p + e^+ + e^-. \tag{1.8}$$

At increasingly higher cosmic ray proton energies, $> 10^{19.5}$ eV (E_{GZK}), energy losses due to pair production start to become insignificant and the attenuation of energy is largely due to photo-pion production defined by the interaction

$$p + \gamma_{CMB} \rightarrow \Delta^+ \rightarrow p + \pi^0 \tag{1.9}$$

$$\rightarrow \Delta^+ \rightarrow n + \pi^+ \tag{1.10}$$

Greisen (1966), Zatespin and Kuz'min (1966) (GZK) postulated that cosmic rays greater than this energy will suffer large energy losses, e.g. $\sim 20\%$ at 5×10^{19} eV over a length of 1 Mpc, due to pion production. At energies exceeding $10^{20.5}$ eV, the energy loss length is roughly 10 Mpc (Achterberg *et al.*, 1999). These conditions impose a limit on how far away the UHECR protons originate, no farther than $\sim$ 100 Mpc, and should cause a complete flux suppression at energies $\geq E_{GZK}$ at Earth's atmosphere.

1.3 Ultra High Energy Cosmic Ray Extensive Air Showers

After traversing the relatively low particle densities of intergalactic and interstellar space, UHECRs that survive the journey to Earth's atmosphere immediately transition to a high density environment and collide into an atmospheric molecule. This first interaction, which is initiated at 10's of km high in the atmosphere, produces a cascade of particles and light commonly referred to as an extensive air shower (EAS).

EAS generated by a 10^{19} eV proton will produce $\sim 10^{10}$ particles at sea level, and cover a ground area of roughly a few km^2. A large majority of the particles, about 99%, are photons, electrons, and positrons, where the photon to electron/positron ratio is about 6

to 1. The individual energies of these particles are in the range 10^6 to 10^7 eV and account for 85% of the total energy. The composition of the remaining 15% of the total energy is a combination of muons, pions, neutrinos, and baryons, with 10% and 4% of the total energy comprised by muons and pions, respectively (Letessier-Selvon and Stanev (2011)). A longitudinal profile of the multiplicities of shower particles is shown in Figure 1.4.

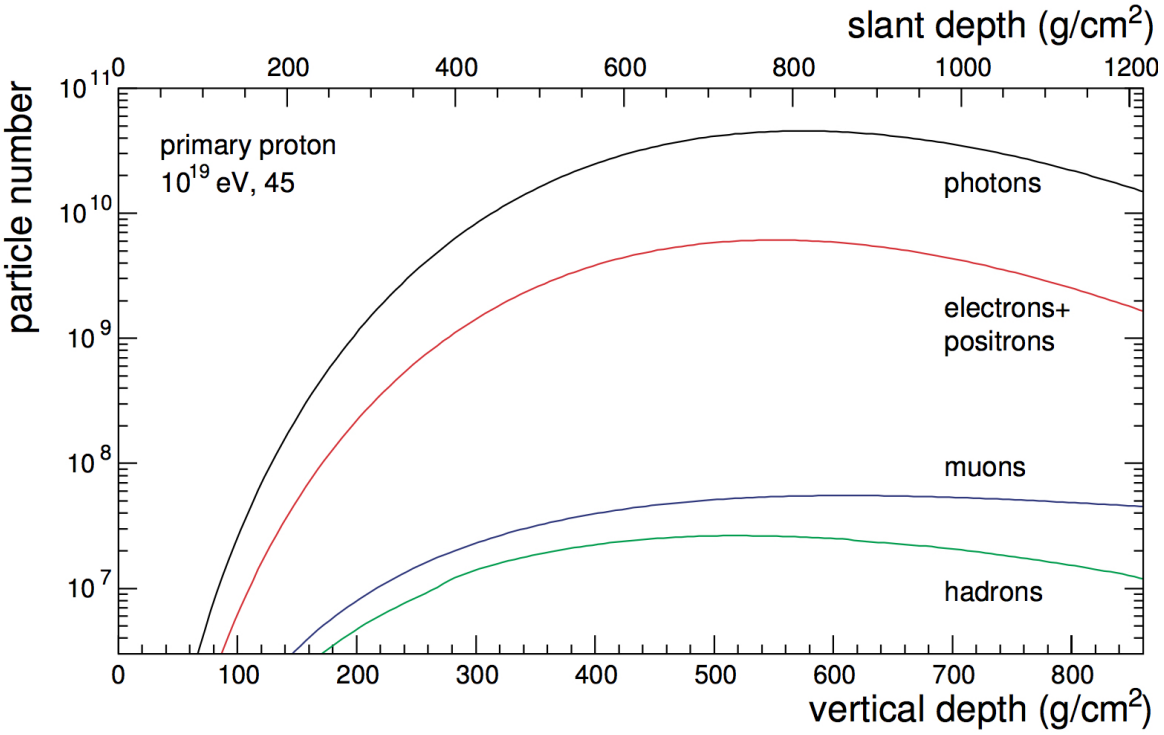

Figure 1.4: Longitudinal profile showing multiplicities of particles produced in an EAS. Figure acquired from Waldenmaier (2006).

The development of EAS in Earth's atmosphere is a complex process. However, the fundamental principles of the shower can be understood by the examination of Heitler's (1954) model, which describes the evolution of an electromagnetic shower.

1.3.1 Heitler's Model

The model, as outlined in Matthews (2005), describes the progression of the electromagnetic cascade as a 2^n process, where n is the number of interaction steps. Each interac-

tion step corresponds to a particle or group of particles traveling a characteristic interaction length, d, and then each producing two secondary particles of equal energy through either one of two processes. If the particle is an electron, half of the energy is imparted to a single photon through bremsstrahlung emission while the other half is retained by the electron. In the case of a photon, the energy is split amongst an electron/positron pair (see left pane of Figure 1.5).

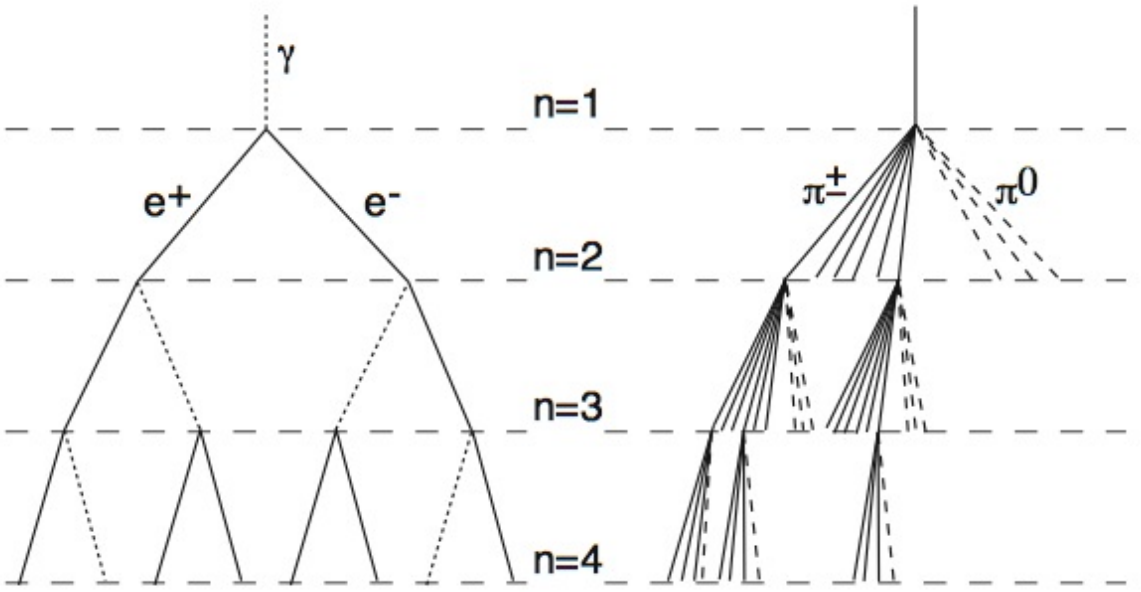

Figure 1.5: Left: Sketch of electromagnetic cascade. Right: Sketch of a hadronic cascade. Figure acquired from Hörandel (2006).

The interaction length d is determined by the equation

$$d = X_r \ln 2 \tag{1.11}$$

where X_r is the radiation length of the medium (X_r = 36.7 g cm^{-2} in air). After n steps has been achieved, the number of particles N_n and the individual particle energy E_p, given the

primary particle energy E_0, are given by

$$N_n = 2^n \tag{1.12}$$

$$E_p = \frac{E_0}{N_n}. \tag{1.13}$$

From Eq. 1.12 and Eq. 1.13 we obtain that n steps has the functional form

$$n = \frac{\ln\left(\frac{E_0}{E_p}\right)}{\ln 2}. \tag{1.14}$$

The shower reaches a maximum number of particles, i.e. electrons, when the individual particle energy is less than or equal to the critical energy, E_c^{γ}. This energy is obtained when the rate of energy loss by bremsstrahlung emission is equal to the rate of energy loss by ionization. In air this value is about E_c^{γ} = 8 x 10^7 eV.

Through Heitler's simplistic model three properties of the electromagnetic component of EAS are obtained. Firstly, the maximum number of particles accumulated, shower maximum, is given by

$$N_e^{max} = \frac{E_0}{E_c^{\gamma}}. \tag{1.15}$$

Models show that this value overestimates the maximum number of electrons at shower maximum and has a corrected form of $N_e^{max} = E_0/(gE_c^{\gamma})$ ($g \approx 13$). Secondly, the atmospheric depth, which has units of g cm^{-2}, at which the shower maximum parameter X_{max} occurs is given by

$$X_{max} = X_0 + nd = X_0 + X_r \ln\left(\frac{E_0}{E_c^{\gamma}}\right) \tag{1.16}$$

where X_0 is the initial atmospheric depth at which the shower started. Showers initiated by primaries with energies above 10^{18} eV typically have X_{max} occur at atmospheric depths

between 700 g cm^{-2} and 800 g cm^{-2}. Lastly, the rate of change of X_{max} with change in energy, known as the elongation rate, is defined as

$$D_{10} \equiv \frac{dX_{\max}}{dlog_{10}E_0} = 2.3\mathrm{X_r} \tag{1.17}$$

which corresponds to D_{10} = 84.4 g cm^{-2} in air.

1.3.2 Hadronic Showers Considerations

Heitler's model can be modified, as outline in Hörandel (2006), to analytically approximate the aforementioned parameters in the previous section, but in the case of a hadronic shower. The characteristic interaction length, d_h, is now defined by $d_h = X_h ln2$, where X_h is the hadronic interaction length of the medium (X_h = 120 g cm^{-2} in air). Each hadronic interaction is assumed to produce $2N_\pi$ charged pions and N_π neutral pions (see right pane of Figure 1.5). Each neutral pion will decay into two photons. However, high energy charged pions will continue to undergo interactions with their environment, producing more pions of lower energy, until they reach a critical energy, E_c^π, where decaying to muons and antineutrinos is the dominant process. At each step, energy is shared equally by the secondary pions. Although in this modified model the interaction length and the pion multiplicity ($3N_\pi$) are energy independent, a realistic number should be chosen for N_π. Pion energies in the range 10^9 to 10^{13} eV are represented by N_π = 5.

The maximum number of muons produced in the shower can be determined by assuming that all charged pions decay into muons when they reach the critical energy. Using a similar line of logic as used for Eqs. 1.12-1.14, the maximum number of muons is given by

$$\mathrm{N}_\mu = \left(\frac{\mathrm{E}_0}{\mathrm{E}_c^\pi}\right)^\beta \tag{1.18}$$

where $\beta = \frac{ln2N_\pi}{ln3N_\pi}$. Equation 1.18 may be extended to include the mass dependence of the muon multiplicity by invoking the superposition model which states that a primary of en-

ergy E_0 and mass A may be represented as the sum of A independent proton initiated showers each of energy $\frac{E_0}{A}$, given that they start at the same position in the atmosphere. Therefore, the mass dependent muon multiplicity is

$$N_\mu = A\left(\frac{E_0}{AE_c^\pi}\right)^\beta = \left(\frac{E_0}{E_c^\pi}\right)^\beta A^{1-\beta}. \tag{1.19}$$

Equation 1.19 shows that the muon component of the hadronic shower does not scale linearly with the primary cosmic ray energy, the muon multiplicity will increase slowly for realistic values of β (β = 0.85 for N_π = 5). Furthermore, higher mass primaries increases the muon multiplicity.

The number of electrons can be determined by examining the energy associated with the muon component of the shower, which essentially is representative of the energy stored in the hadronic portion of the shower. As energy must be conserved, the total energy of the shower is simply the sum of its electromagnetic and hadronic parts, i.e. $E_0 = E_{\text{Hadronic}} + E_{\text{Electromagnetic}}$. The hadronic energy is represented by $E_{\text{Hadronic}} = N_\mu E_c^\pi$ and may be used to yield the following relationship for the electromagnetic component

$$\frac{E_{Electromagnetic}}{E_0} = \frac{E_0 - N_\mu E_c^\pi}{E_0} = 1 - \left(\frac{E_0}{AE_c^\pi}\right)^{\beta-1}. \tag{1.20}$$

Approximating Eq. 1.20 as a power law, $\frac{E_{Electromagnetic}}{E_0} \approx a\left(\frac{E_0}{AE_c^\pi}\right)^b$, and combining it with the corrected form of Eq. 1.15 yields

$$N_e = \frac{E_0}{E_c^\gamma}\frac{E_{Electromagnetic}}{E_0} \approx a\left(gE_c^\gamma\right)^{-1}\left(AE_c^\pi\right)^{-b}\left(E_0\right)^{1+b}, \tag{1.21}$$

where $a = \left(1 - x^{\beta-1}\right) / \left(x^b\right)$, $b = (1-\beta) / \left(x^{1-\beta} - 1\right)$, and $x = E_0/(AE_c^\pi)$. Again assuming realistic values for β, this analytical result shows that the electromagnetic component of the shower will decrease with for higher mass primaries.

As suggested by Eq.1.19 and Eq.1.21, the number of muons relative to the number of

electrons produced at ground level indirectly offers information about the composition of the primary cosmic ray. Each hadronic interaction gives one third of the energy to the electromagnetic component of the cascade while the remaining 2/3rd continues as hadrons. Therefore, the longer it takes for pions to reach the critical energy E_c^{π} the larger the electromagnetic component will be. Ultimately, leading to a relatively smaller muon component. Logically, one can conclude that long developing showers are the result of the first pions having a high Lorentz factor, which is an indication that the shower was initiated by a high energy, light nucleus. In addition, primaries with smaller cross sections will have a smaller muon to electron ratio at ground.

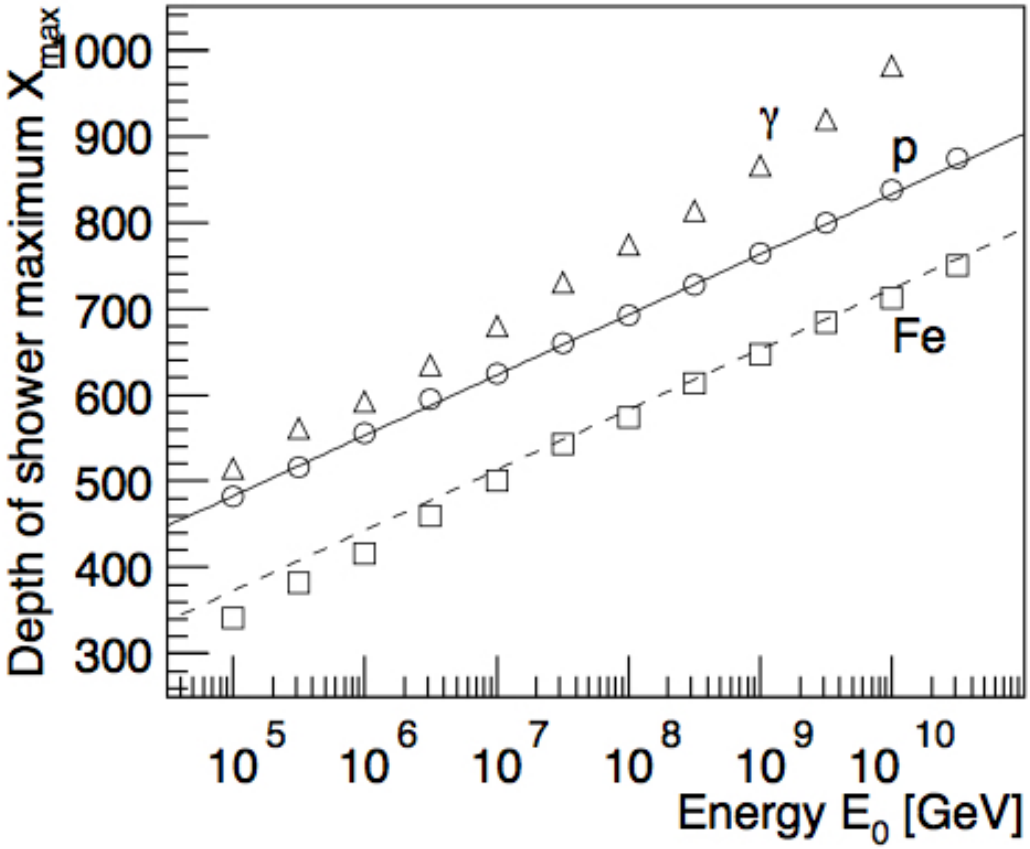

Figure 1.6: Average depth of shower maximum for primary photons, protons, and iron nuclei from CORSIKA simulations. The dashed line indicates the prediction for X^p_{max} and the solid line is the same prediction corrected by a shift of 110 g/cm^2. Figure acquired from Hörandel (2006).

The extension of Heitler's model in determining X_{max} for proton initiated hadronic showers fails by a difference of 110 g cm^{-2} compared to simulations over the energy range of $\sim 10^{13}$ eV to $\sim 10^{20}$ eV. However, the simple assumptions of the modified model do well in determining the elongation rate, which shows the change in X_{max} with respect to change in energy. Furthermore, applying the superposition model yields the following relationship for the atmospheric depth at shower maximum

$$X_{max}^{A} = X_{max}^{p} - X_r \ln A. \tag{1.22}$$

Equation 1.22 shows that X_{max} is a useful tool in determining the mass of the primary. Of course this is purely from a theoretical standpoint as X_{max} must be determined statistically due to shower-to-shower fluctuations. Comparisons between Hörandel (2006) analytic model and CORSIKA simulations are shown in Figure 1.6.

1.3.3 Nitrogen Fluorescence from Extensive Air Showers

As the cascade of shower particles travel through the atmosphere, atmospheric molecular nitrogen is ionized. The excitation of a N_2 molecule typically lasts 10 to 50 ns before emitting a ultraviolet (UV) photon through relaxation (Hanlon, 2008). The nitrogen fluorescence photons are emitted isotropically and most of the emission is between 300 to 400 nm, as seen in Figure 1.7. Most of the energy released into the atmosphere is attributed to secondary electrons and positrons with energies between 30 MeV and 1 GeV. An example of their individual and combined contributions to the energy released into the atmosphere at shower maximum is shown in Figure 1.8.

One would expect the total number of emitted fluorescence photons to be proportional to the energy deposited in the atmosphere by electrons and positrons. The total energy

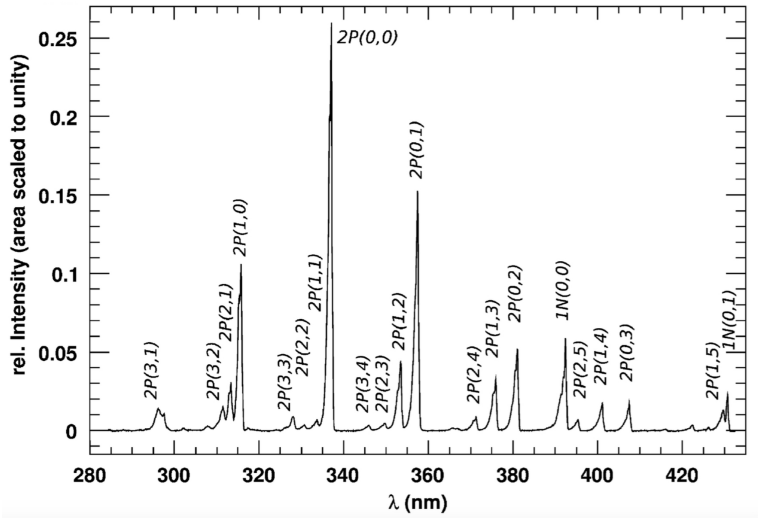

Figure 1.7: Air fluorescence spectrum excited by 3 MeV electrons at 800 hPa as measured by the AIRFLY Collaboration. Figure acquired from Arqueros, Hörandel, and Keilhauer (2008).

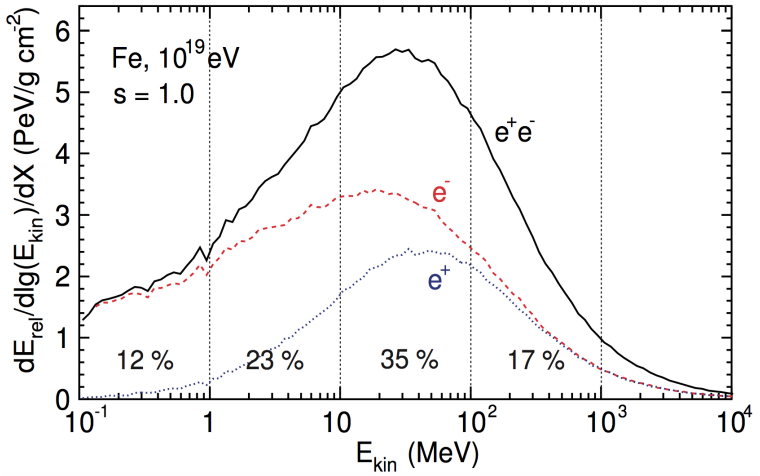

Figure 1.8: Simulation of the total contribution to the energy release per gram of traversed matter. Image from Waldenmaier (2006).

deposited in the atmosphere within a layer dX is

$$\frac{dE_{dep}^{tot}}{dX} = \int \frac{dN_e(X)}{dE_{kin}} \cdot \frac{dE_{dep}}{dX} \, dE_{kin}, \tag{1.23}$$

where $\frac{dN_e(X)}{dE_{kin}}$ is the energy distribution of electrons and positrons produced by the shower at the atmospheric depth, X, $\frac{dE_{dep}}{dX}$ is the energy deposited after traversing a layer dX, all of which is integrated over kinetic energies dE_{kin} (Waldenmaier, 2006). Assuming that the fluorescence yield, Y, is only dependent on the temperature, pressure, and humidity of the ambient medium, wavelength of the emission, and absolute fluorescence yield (Arqueros, Hörandel, and Keilhauer, 2008), the number of fluorescence photons as a function of atmospheric depth and wavelength is

$$\frac{d^2N_\gamma}{dXd\lambda} = Y(\lambda, T, p, u) \cdot \frac{dE_{dep}^{tot}}{dX}. \tag{1.24}$$

Using Eq. 1.23, the total number of photons detected by a fluorescence telescope can be calculated by

$$\begin{aligned} \frac{dN_\gamma}{dX} &= \int \frac{d^2N_\gamma}{dXd\lambda} \cdot T_{atm}(\lambda, X) \cdot \varepsilon_{FD}(\lambda) \, d\lambda \\ &= \frac{dE_{dep}^{tot}}{dX} \cdot \int Y(\lambda, T, p, u) \cdot T_{atm}(\lambda, X) \cdot \varepsilon_{FD}(\lambda) \, d\lambda \end{aligned} \tag{1.25}$$

where $T_{atm}(\lambda, X)$ and $\varepsilon_{FD}(\lambda)$ are the transmission of the atmosphere and total fluorescence telescope efficiency, respectively. We see from Eq. 1.25 that the number of photon detected at the aperture of the fluorescence telescope is proportional to the energy deposited in the atmosphere by electrons.

1.4 Extensive Air Shower Detection

At the lowest cosmic ray energies, cosmic rays may be detected directly with ballon experiments or satellites like the LEAP experiment and the Solar Heliospheric Observatory,

respectively. However, at higher primary cosmic ray energies, especially in the energy regime of the UHECRs ($> 10^{18}$ eV), detection of cosmic rays by these means are no longer feasible due to the low flux of these particles. Therefore, other means of detection must be used.

As stated in § 1.3, UHECRs produce large showers that are a combination of particles and light. Currently, there are two well established means of detection of EAS, surface particle detector arrays and fluorescence telescopes. The former utilizes the particles produced during the shower to make measurements of the fundamental shower properties, while the later uses nitrogen fluorescence emission from the shower for the same purpose.

1.4.1 Pierre Auger Observatory Surface Detector Array

The Pierre Auger Observatory, as depicted in Figure 1.9, is currently the largest cosmic ray detector in the world that observes cosmic ray events in the energy range from 10^{18} eV to 10^{20} eV. Located in the Province of Mendoza, Argentina, the Pierre Auger Observatory has 1600 Cherenkov stations each at a distance of 1500 m relative to its nearest neighbor and covering an area of 3000 km^2. As seen in Figure 1.10, each station contains 12 tons of ultra pure water and has three internal photomultiplier tubes equally spaced at a distance of 1.2 m from the center of the tank. Equipped with a solar panel, GPS timing and radio communications, each station is fully autonomous (Conceição and for the Pierre Auger Collaboration, 2013). Furthermore, the surface detector (SD) array sits at an altitude of 1400 m above sea level, corresponding to a vertical atmospheric depth of 875 g cm^{-2}, which is a great aspect of the array because it's able to detect EAS close to their maximum (Beatty and Westerhoff, 2009).

The SD samples secondary particles created during the shower by means of measuring the Cherenkov radiation signal produced by muons and electrons traveling at relativistic speeds through the Cherenkov water tanks. Particles detected by individual detectors are then used to determine the lateral distribution function (LDF), which shows how the num-

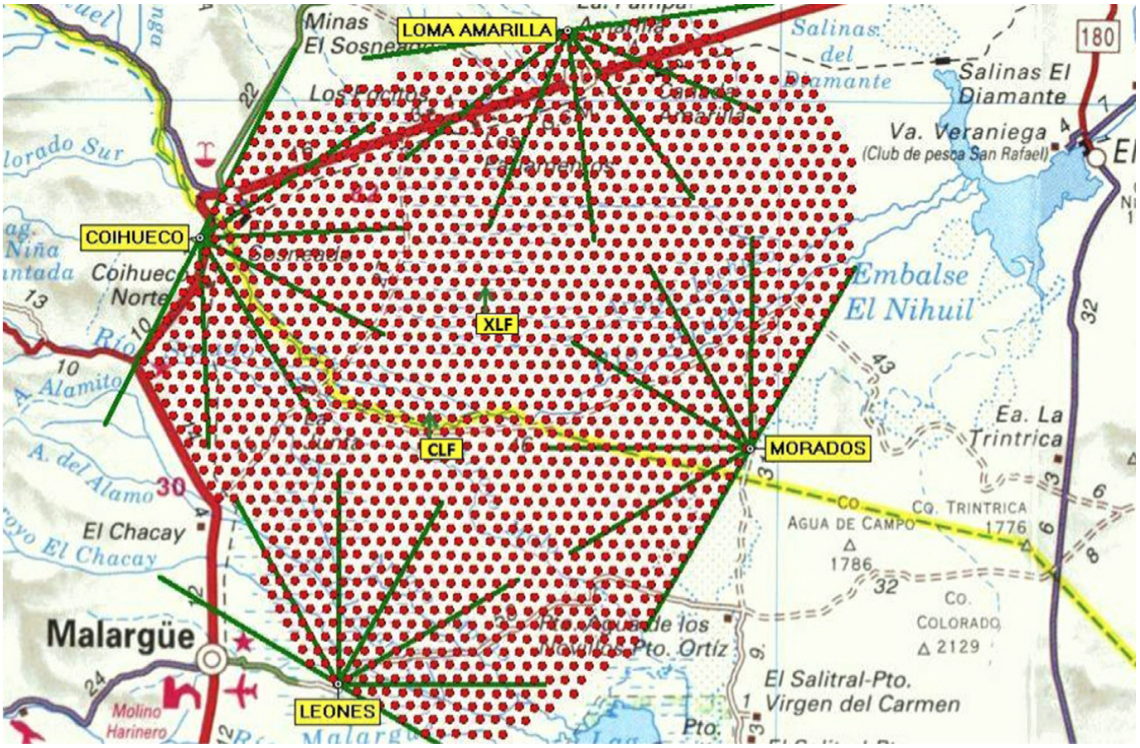

Figure 1.9: Depiction of the Pierre Auger Observatory. The red dots correspond to the 1600 surface detector stations spread over and area of 3000 km^2. The green lines indicate the 30° field of view of the 24 fluorescence detectors (four sites each with six fluorescence detectors) overlooking the array of surface detectors. Also shown are the two laser facilities, CLF and XLF. Figure acquired from The Pierre Auger Collaboration (2015).

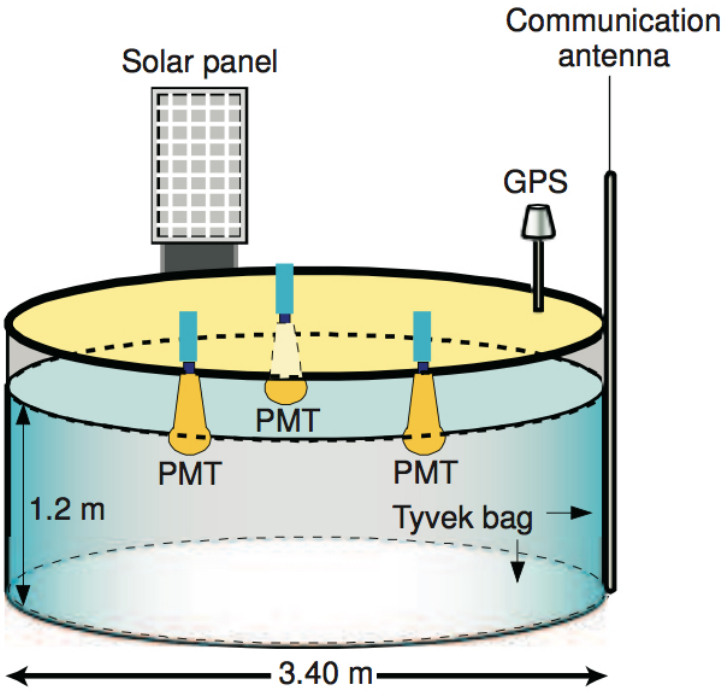

Figure 1.10: Sketch of a Cherenkov detector at the Pierre Auger Observatory. Figure acquired from Waldenmaier (2006).

ber of particles decrease as a function of distance (Barnhill *et al.*, 2005). The fit of the LDF is described by a modified Nishimura-Kamata-Greisen function

$$S(r) = S\left(r_{opt}\right)\left(\frac{r}{r_{opt}}\right)^{\beta}\left(\frac{r+r_1}{r_{opt}+r_1}\right)^{\beta+\gamma} \tag{1.26}$$

where r is the distance relative to the shower core, r_{opt} is the optimum distance, $r_1 = 700$ m, and $S\left(r_{opt}\right)$ is an estimate of the shower size at a distance of r_{opt} used in reconstructing the shower energy. Given the spacing of 1500 m between individual stations in the SD array, the parameter r_{opt} has been determined to be 1000 m, i.e. $S\left(r_{opt}\right) = S\left(1000\right)$. Parameters β and γ are determined by reconstructing the shower via simulation.

Fitting the LDF yields a determination of the core position, and fitting a plane front to the arrival times of signals at individual SD stations is used to determine the shower arrival direction. The angular resolution of the arrival direction for events above 3×10^{18} eV is a

function of shower zenith angle and station multiplicity. As seen in Figure 1.11, with three stations angular resolutions better than 1.6° are achievable. With six stations the angular resolution of arrival direction is better than 0.9°.

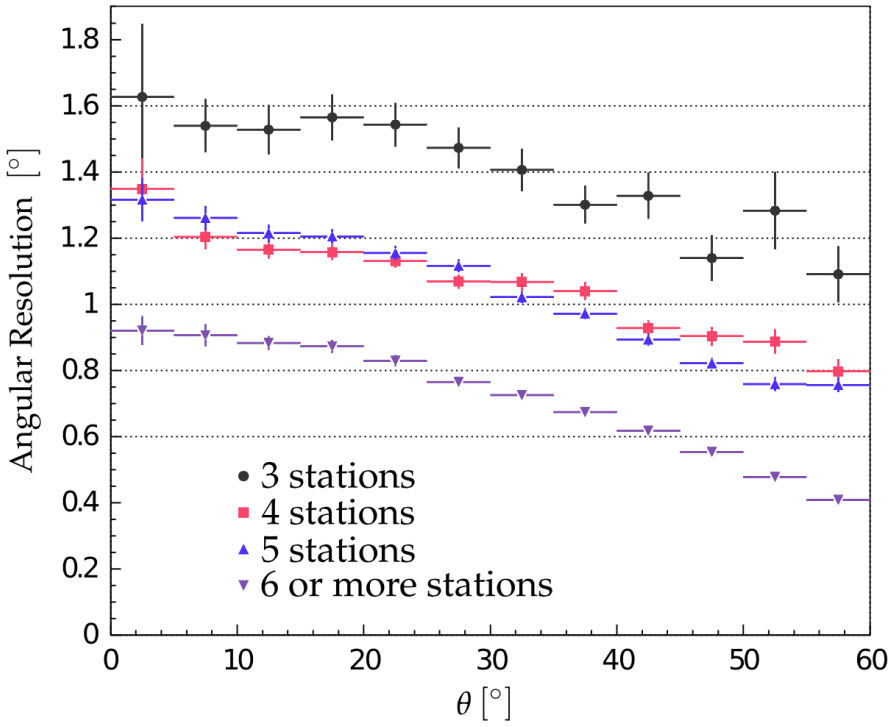

Figure 1.11: Arrival direction angular resolution as a function of the shower zenith angle θ for events with an energy above 3 EeV, and for different station multiplicities. Image from The Pierre Auger Collaboration (2015).

In addition to determining the position of the shower core, the fit $S(r)$ is used to determine the shower energy. More specifically, the parameter $S(1000)$, the signal strength of the shower 1000 m from the shower core, is used as an energy estimator due to a minimization in shower-to-shower fluctuations for showers initiated by primaries with the same energy and mass, a result solely dependent on the geometry of the Auger Observatory's SD array (Newton, Knapp, and Watson, 2007). However, showers of the same energy and primary mass will have different values of $S(1000)$ for different zenith angles, θ. To account for this discrepancy, $S(1000)$ is reinterpreted as S_{38}, the signal a shower with size $S(1000)$ would have produced had it arrived at $\theta = 38°$, by correlating high quality events

in which the shower size is given by the SD and the shower energy by Auger's fluorescence detectors. The relationship between S_{38} and the shower energy determined by the fluorescence detectors, E_{FD}, as shown in Figure 1.12, yields a SD energy resolution of $(16 \pm 1)\%$ at lower energies and $(12 \pm 1)\%$ at the highest energies (The Pierre Auger Collaboration, 2015).

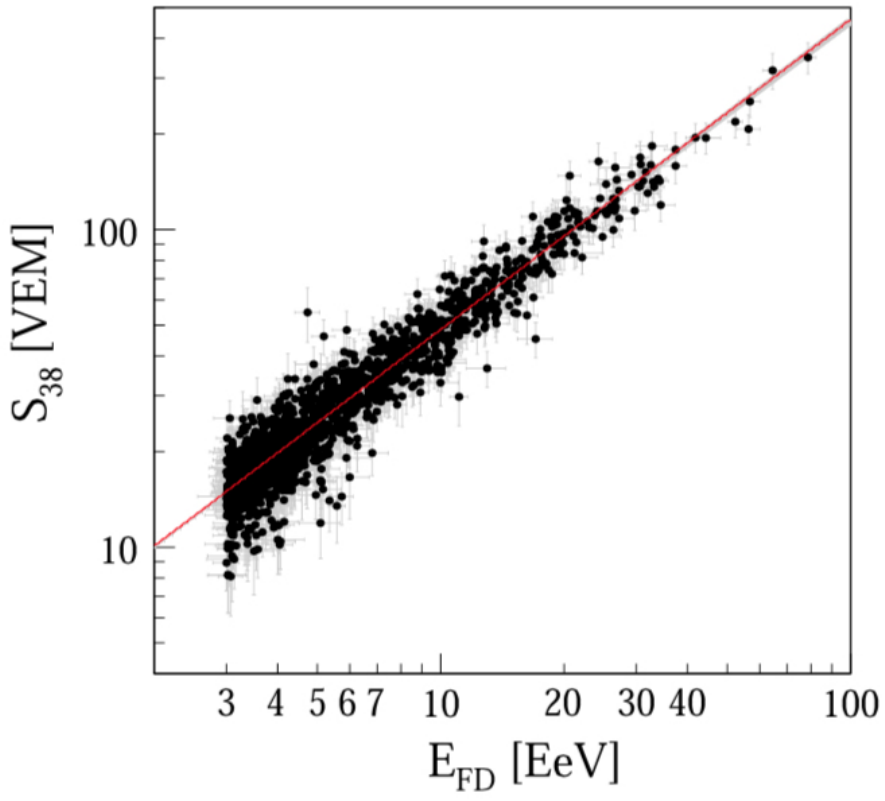

Figure 1.12: Correlation between S_{38} and E_{FD}. Figure acquired from The Pierre Auger Collaboration (2015).

1.4.2 Pierre Auger Observatory Fluorescence Detector

Another method the Pierre Auger Observatory employs to detect EAS are the fluorescence detectors. Overlooking the SD array are 24 fluorescence detectors (FDs). In groups of six, the FD telescopes are housed within four sites located along the boarder of the SD array (see Figure 1.6). Each FD has a $30^\circ \times 30^\circ$ field of view in azimuth and elevation,

with a minimum elevation of 1.5° above the horizon. Light from the shower is focused onto a spherical focal surface by a segmented spherical primary mirror 3.4 m in radius. At the focus of a FD sits a camera composed of a matrix of 440 photomultiplier tubes (PMTs) each with a field of view of 1.5°. To ensure the detection of only the isotropically emitted UV light from the shower, the 1.1m radius entrance is covered by a Schott MUG-6 filter glass window that is specifically designed to filter out all light outside of the UV range between 310 and 390 nm. As seen in Figure 1.13, shutters are used to protect the optics from undesired light and during times of poor weather conditions The Pierre Auger Collaboration (2015).

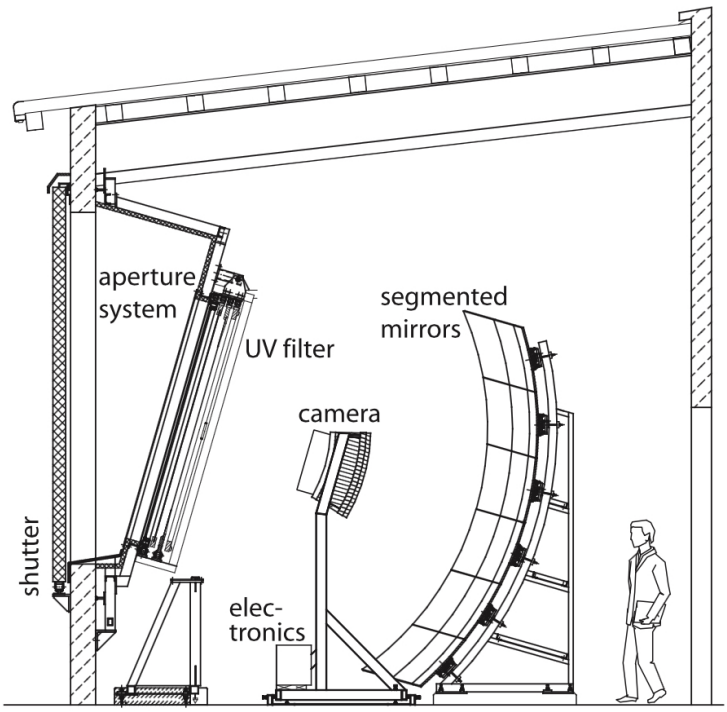

Figure 1.13: Schematic showing key components of a single FD telescope. Image from The Pierre Auger Collaboration (2015).

UV fluorescence light from a segment of the shower produces a track across the field of view of a FD, this projection of the shower segment on the camera establishes the shower-detector-plane (SDP), as seen in Figure 1.14. Each pulse from the shower detected by a pixel, single PMT, can be associated with an angle χ_i along the SDP with respect to the

horizontal axis of the FD. The geometry of the SDP yields the following relationship for the arrival time of photons from the shower detected by the i^{th} pixel

$$t_i = t_0 + \frac{R_p}{c} \tan\left(\frac{\chi_0 - \chi_i}{2}\right), \tag{1.27}$$

where t_0 is the time of emission of the UV light from a segment of the shower, R_p is the distance of closest approach between the segment of the shower and the FD in the SDP, c is the speed of light, χ_0 is the exterior angle made between the shower axis and the ground, and χ_i is the angle made between a ray of light from the shower to the i^{th} pixel and the ground. The parameters t_0, R_p, and χ_0 are determined by using a χ^2 minimization procedure that relies on timing information from both the FD and the SD station to find the best fit in the SDP.

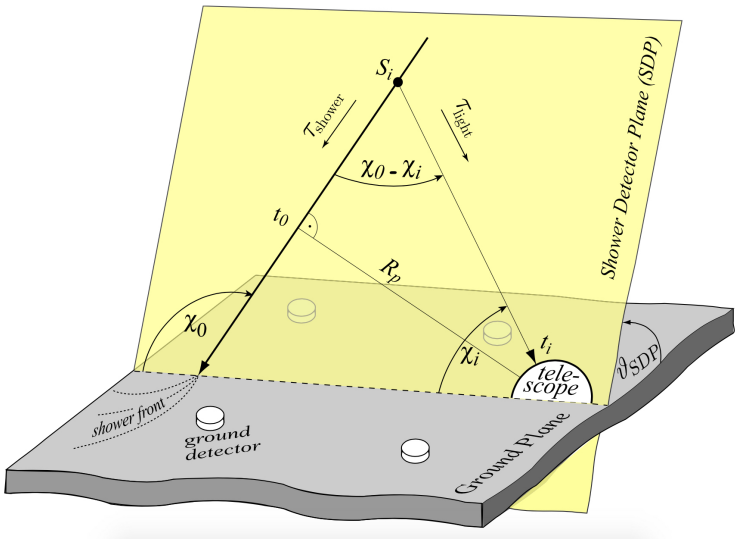

Figure 1.14: Sketch of geometrical parameters used to define the shower-detector-plane. Figure acquired from Kuempel *et al.* (2008).

Once the shower geometry has been determined, the fluorescence light collected by the FD telescopes can be used to calculate the shower energy. However, during the production of the shower, light detectable at the aperture, as seen in Figure 1.15, may be nitrogen fluorescence light, direct Cherenkov light, scattered Mie and Rayleigh Cherenkov light,

or multiple scattered fluorescence light. As there is a relationship between the energy deposited into the atmosphere and the Cherenkov and fluorescence signal detected at the telescope, a set of analytic equations, similar to Eq. 1.23, are used to estimate the energy deposit (Unger *et al.*, 2008).

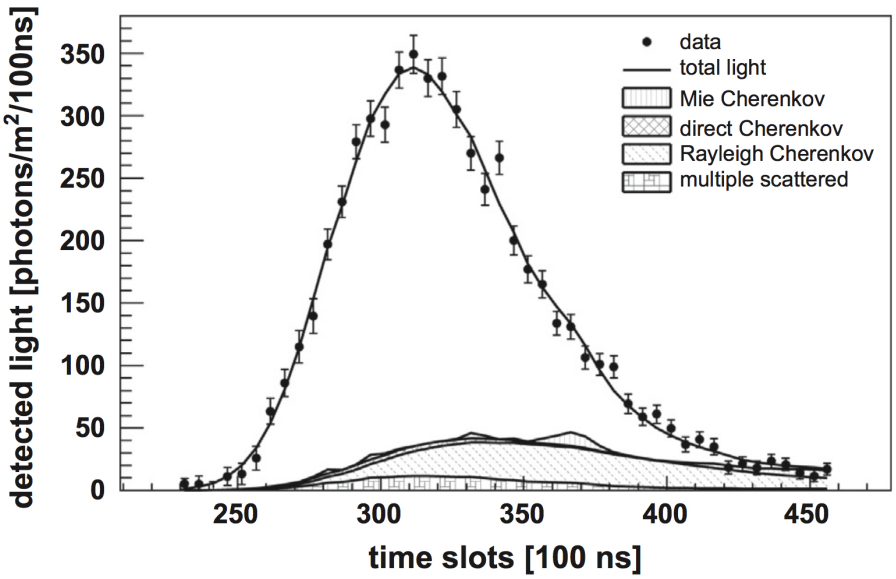

Figure 1.15: Simulated example of reconstructed light distributions detected at the aperture. Image from The Pierre Auger Collaboration (2015).

After decomposing the signal from the various sources of light, the longitudinal energy deposit profile, $f_{GH}(X)$, and its maximum, $\left(\frac{dE}{dX}\right)_{max}$, can be estimated by fitting a Gaisser-Hillas function

$$f_{GH}(X) = \left(\frac{dE}{dX}\right)_{max} \left(\frac{X - X_0}{X_{max} - X_0}\right)^{\frac{X_{max}-X_0}{\lambda}} e^{\frac{X_{max}-X_0}{\lambda}} \tag{1.28}$$

to the signal detected by the PMTs of the FD cameras. However, the data must be corrected for the aforementioned contributions to the fluorescence signal by direct and scattered Cherenkov light and fluorescence light that has undergone multiple scatterings. In addition, corrections must be made for the attenuation of light by the atmosphere between the detector and shower as well as light outside of the collection area of the detector. Fur-

thermore, the parameters X_0 and λ are shape parameters sensitive to the energy and mass of the primary, and are typically constrained to their average values determined by hadronic simulations (Unger *et al.*, 2008).

The calorimetric energy is determined by integrating Eq. 1.28 with respect to atmospheric depth; however, the shower energy is not wholly encompassed within the fluorescence light signal. Therefore, the energy of the primary is estimated by multiplying the calorimetric energy by a correction factor that accounts for energy carried away by neutrinos and high energy muons. The reconstruction process yields an energy resolution of 7.6%, angular resolution of 0.6%, and X_{max} error less than 20 g/cm^2 in hybrid mode.

1.5 Anisotropy of the Ultra High Energy Cosmic Rays

The Hillas plot (see Figure 1.1) offers a great starting point in determining the origin of the UHECRs, as the simple logic upon which it is based does well at restricting various types of sources as a function of cosmic ray energy and mass; however, this theoretical perspective it is not enough. Cosmic ray experiments with the goal of measuring the energy, composition, and arrival direction of the UHECRs are vital to this endeavor because their measurements allow for solutions to this problem from different points of view. One particularly straightforward means of determining the sources of the UHECRs is through comparisons between their arrival directions on the sky and the positions of catalogued astrophysical sources. At energies near 10^{18} eV, the distribution of the UHECRs is isotropic due to significant magnetic deflections that occur on the way from their source to Earth. As cosmic ray energies approach values upward of 40 EeV, magnetic deflections are on the order of a few degrees for primaries with low charge. This characteristic of the highest energy cosmic rays make them the perfect study set for the determination of sources. In addition, the GZK effect (see § 1.2.2) limits the distance over which an UHECR with energy greater than 5×10^{19} eV can travel, further reducing source candidates.

In an early analysis conducted by the Pierre Auger Collaboration, the arrival directions

of cosmic rays above 57 EeV was reported to exhibit an anisotropic distribution with a rejection of the null hypothesis of an isotropic distribution at a confidence level of at least 99% (Abraham *et al.*, 2007, 2008). The claim was based on angular separations, no greater than 3.1°, between the arrival directions of 27 Auger events above 57 EeV and AGN closer than 75 Mpc in the Veron-Cetty and Veron (VCV) catalog. However, in 2010 Abreu *et al.* (2010) reported a diminished correlation, $\sim 3\sigma$, with the accumulation of more events (69 events) above 57 EeV. A more recent update to this analysis has been conducted with 146 events above 53 EeV reporting an even lower correlation of 2 standard deviations above the null hypothesis, which lead to the conclusion that the initial result was a statistical fluctuation (Aab *et al.*, 2015). On the contrary, in the northern hemisphere with 5 years of data for events above 57 EeV, the Telescope Array (TA) has detected a signature of anisotropy at a significance of 5.1σ relative to the null hypothesis (Abbasi *et al.*, 2014). However, they await more data to see if the anisotropy holds.

As indicated by the Hillas plot, there exists several different types of astronomical objects that may serve as cosmic ray accelerators. The Pierre Auger Observatory has also utilized the 2MASS Redshift Survey, the Swift-BAT X-ray catalog, and a catalog composed of radio emitting sources to find excesses in the arrival directions of the UHECR distribution above a minimum energy of 40 EeV. The 2MASS Redshift Survey maps the distribution of normal galaxies in the nearby universe which may serve as a road map for gamma ray bursts or highly energetic neutron stars. The Swift-BAT X-ray catalog maps the distribution of high energy events like AGN in spiral galaxies. Lastly, the radio emission catalog traces extended jets and radio lobes of AGN within elliptical galaxies. Analysis with each catalog is conducted by counting the number of pairs between UHECR events and objects in a given catalog at a specific energy and angular separation, and then is compared against what would be expected from an isotropic distribution of arrival directions. This process is repeated for different values of energy (40 EeV $\leq$ E $\leq$ 80 Eev), different values of separation angle ($1^\circ \leq \Delta\theta \leq 30^\circ$), and different values of distance from 10 Mpc

to 200 Mpc in steps of 10 Mpc. The results that yield the highest correlation, as shown in Figure 1.16, all paint the same picture, that there is no significant correlation between the Auger events and possible sources in the nearby universe. If indeed the source distribution is anisotropic, the results could be explained by the presence of heavier cosmic rays with increasing energy (see e.g. Settimo and Pierre Auger Collaboration, 2016), as their deflections in magnetic fields would be larger leading to an isotropization of the arrival directions.

1.6 Improving the Statistics of the UHECR

Since the first observation of a cosmic ray particle with an energy exceeding 10^{20} eV (Linsley, 1963), much progress has been made in the examination of the UHECRs. State of the art cosmic ray observatories like the Pierre Auger Observatory and the TA as well as cosmic ray models analyzed via simulation by software suites like CORSIKA have allowed us to better understand the nature of the UHECRs by providing measurements of cosmic ray energy, composition, arrival direction at unprecedented statistics. Nonetheless, fundamental questions regarding their origin and acceleration mechanism still remain unanswered, indicating that the current state of experiments is not enough to handle the task.

While future space-based experiments like the Extreme Universe Space Observatory in the Japanese Experiment Module (JEM-EUSO) will provide a significant increase in the number of detections above 10^{19} eV (Adams *et al.*, 2015), with an aperture that is estimated to be $\geq 2\times10^5$ km^2 sr, there is still room for low cost ground-based experiments that may prove to be complementary to the currently established techniques or standalone methods capable of producing high-quality data. In the next chapter, we explore the idea of detecting air showers through isotropic microwave emission.

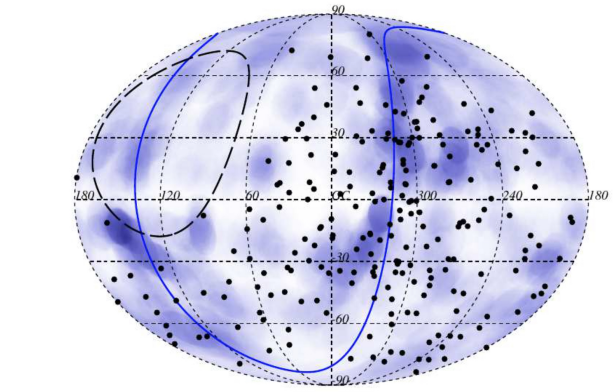

(a)

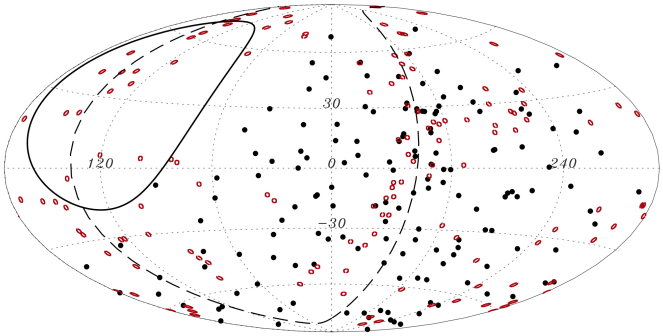

(b)

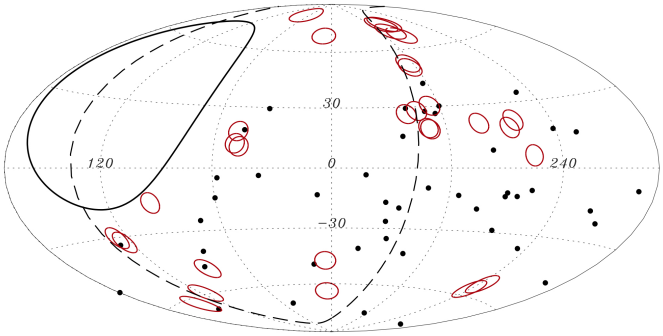

(c)

Figure 1.16: (a): Cross-correlation of events (black dots) with E $\geq$ 52 EeV with galaxies in the 2 Mass Redshift Survey. Blue fuzzy circles of 9° radius are drawn around all objects closer than 90 Mpc. Region within dashed line is outside of Auger's field of view and blue solid line represents the Super-Galactic Plane. (b): Cross-correlation of events (black dots) with E $\geq$ 58 EeV with BAT AGN in the Swift-BAT catalog. Red circles of 1° radius are drawn around all objects closer than 80 Mpc. Region within solid line is outside of Auger's field of view and dashed line represents the Super-Galactic Plane. (c): Cross-correlation of events (black dots) with E $\geq$ 72 EeV with AGN in the catalog of radio galaxies. Red circles of 4.75° radius are drawn around all objects closer than 90 Mpc. Region within solid line is outside of Auger's field of view and dashed line represents the Super-Galactic Plane. Image from Aab *et al.* (2015).

CHAPTER 2

EXTENSIVE AIR SHOWER MICROWAVE EMISSION

2.1 Motivation Behind Observing Microwave Emission from EAS

Experiments like the Pierre Auger Observatory and the Telescope Array (TA) (Kawai *et al.*, 2008) utilize two well established techniques in hopes of identifying the origin of the UHECRs as well as determine the physics behind acceleration mechanisms. To achieve this goal, precise measurements of the primary energy, direction, and composition are required at the highest energies observed. Outlined in § 1.4 are the basic principles of the successful methods of detection; however, they have their disadvantages. While a SD array offers a duty cycle close to 100 %, has an easily calculated aperture, and can reconstruct arrival directions to within a degree, a SD array is only able to sparsely measure secondary particle densities at a single stage of shower development. This particular disadvantage coupled with shower-to-shower fluctuations and the necessity to use hadronic models results in relatively large systematic uncertainties when reconstructing the shower energy. Similar consideration applies to the SD sensitivity to the mass of the primary. Lastly, sampling secondary particles from an EAS is expensive as a SD array requires a large observing area and many particle detectors due to the lateral extent of the showers.

The FD technique allows for the observation of the longitudinal development of an EAS. Given the relationship between the energy deposited in the atmosphere and the number of particles produced in a shower, determination of the shower maximum and shower energy are relatively easy and have higher accuracy. However, determination of shower geometry can be problematic in cases where only a single FD telescope observes and EAS, which is commonly referred to as a monocular observation. This problem is diminished for

events observed by multiple FD telescopes, commonly referred to as stereo observations. A significant disadvantage of the FD technique is that observations can only be made on moonless nights with good weather conditions, resulting in a duty cycle of about 10%.

The disadvantages of the two techniques, the FD and SD, are reduced by observing events using both techniques simultaneously. This method of detection is referred to as hybrid observations and has been shown to yield high quality results relative to observations performed by either technique alone (see e.g. The Pierre Auger Collaboration (2015)). However, this method is only viable during periods of time when the FD is operational. Therefore, it unfortunately inherits the FD's limited duty cycle. To help answer fundamental questions in regards to the origin and energy of the UHECRs, high quality results at a cadence much higher than what is provided by current hybrid observations are needed.

A possible solution may be observing EAS in the radio regime of the electromagnetic spectrum. Credence was given to this idea decades ago due to experiments conducted in the 1960s looking for signatures of radio emission from air showers. The first experiment to detect radio emission from an EAS was Jelley *et al.* (1965) at a frequency of 44 MHz. Following this initial discovery were several experiments that successfully observed radio emission in the frequency range from 2 MHz up to 520 MHz (Falcke, Gorham, and Protheroe, 2004). These studies primarily focused on polarized, beamed coherent emission in the forward direction of showers and is now primarily attributed to the superposition of two effects: geomagnetic deflection and the Askaryan effect (Schröder, 2016). However, during the 1970s studying radio emission from air showers came to a halt and other, more favorable, avenues of detection were able to flourish.

In the early 2000s, interest in radio detection of cosmic rays was renewed due to technological advancements in digital signal processing techniques. Over the past decade, many experiments have been conducted and have also successfully detected the beamed radio emission from EAS (see e.g. Huege and the LOPES Collaboration (2008), Belletoile (2011), Hörandel (2016), and Schröder (2016) and references therein). Given the nature of

the emission, i.e. forward beamed emission, radio detectors need to observe the emission very close to the shower core. Therefore, needing an array of radio stations spread over a large area, a radio analogue to the SD technique. While studies show that this form of detection does relatively well in determining key shower properties, it has also been suggested that there may exists a form of detection akin to the FD technique.

Molecular bremsstrahlung radiation is isotropic radio emission theorized to produce a signal in the GHz range as a result of the dynamics of electrons in the wake of and EAS. Like the forward beamed emission, a key component of this emission is that it is expected to exhibit some degree of coherence. Furthermore, as the emission is isotropic it would provide a means of detection similar to that of the FD technique at a duty cycle close to 100% as a radio detector is capable of operating during the night, the day, and during poor weather conditions.

2.2 Theory of Isotropic Microwave Emission

As an EAS propagates through the atmosphere, the ionization of atmospheric molecules produces a weakly ionized plasma composed of free electrons, ions, and neutral molecules (Gorham *et al.*, 2008). Under these conditions, and assuming that the velocity distribution of the free electrons can be described by a Maxwell-Boltzmann distribution and are distributed uniformly in space, interactions between the free electrons and fields produced by neutral molecules in the surrounding medium can lead to the isotropic emission of bremsstrahlung radiation. As first discovered by Bekefi (1966), such emission from a region of a given temperature should give rise to a flat spectrum below the spectrum produced by a black body of the same temperature.

To determine the intensity of the emission observed at the detector we can start by examining the emissivity of the region of emission given by

$$\eta_{\omega}(\mathrm{u}) = \frac{\mathrm{e}^2}{24\pi^3\varepsilon_0\mathrm{c}^3}\mathrm{u}^2\nu(\mathrm{u}), \tag{2.1}$$

where e is the charge of an electron, ε_0 is the permittivity of free space, c is the speed of light, u is the electron velocity, and $\nu(\mathrm{u})$ is the velocity dependent electron-neutral collision frequency. The emission coefficient is determined by integrating Eq. 2.1 and the distribution of electron velocities over momentum phase space yielding

$$\mathrm{j}_\omega = \frac{\mathrm{m}\omega_\mathrm{p}}{6\pi^2\mathrm{c}^3}\int_0^\infty \nu(\mathrm{u})\,\mathrm{f}(\mathrm{u})\,\mathrm{u}^4\mathrm{du}, \tag{2.2}$$

where $\mathrm{f}(\mathrm{u})$ is the velocity dependent electron distribution, and $\omega_\mathrm{p} = \sqrt{\mathrm{n_e e^2/m_e}\varepsilon_0}$ is the plasma frequency. As the velocity distribution has been assumed to be Maxwellian, the function $\mathrm{f}(\mathrm{u})$ is given by

$$\mathrm{f}(\mathrm{u}) = \left(\frac{\mathrm{m}_e}{2\pi\mathrm{k}_b\mathrm{T_e}}\right)^{\frac{3}{2}} \mathrm{e}^{-\frac{\mathrm{m}_e\mathrm{u}^2}{2\mathrm{k}_b}\mathrm{T_e}}, \tag{2.3}$$

where k_b is Boltzmann's constant and $\mathrm{T_e}$ is the thermodynamic temperature of the electrons. In a similar fashion, the emissivity can be used to determine the absorption coefficient which is given by

$$\alpha_\omega = -\frac{4\pi}{3\mathrm{c}}\frac{\omega_\mathrm{p}^2}{\omega^2}\int_0^\infty \nu(\mathrm{u})\,\frac{\partial \mathrm{f}(\mathrm{u})}{\partial \mathrm{u}}\mathrm{u}^3\mathrm{du}, \tag{2.4}$$

While traversing an arbitrary region of space from the source to the detector over a path s, the intensity, I_ω, of the emission can be altered. This change in intensity with respect to infinitesimal changes in path length, ds, is defined by the radiative transport equation:

$$\frac{\mathrm{dI}_\omega}{\mathrm{ds}} = \mathrm{j}_\omega - \alpha_\omega \mathrm{I}_\omega. \tag{2.5}$$

We may redefine Eq. 2.5 by defining and substituting the source function, $\mathrm{S}_\omega = \mathrm{j}_\omega/\alpha_\omega$, and

the optical depth, $\tau = \int \alpha_\omega \mathrm{ds}$, to yield

$$\frac{\mathrm{dI}_\omega}{\mathrm{d}\tau} = \mathrm{S}_\omega - \mathrm{I}_\omega. \tag{2.6}$$

Upon integrating Eq. 2.6 along a path s through the region in the direction of the detector yields the formal solution for the intensity:

$$\mathrm{I}_\omega(\tau) = \mathrm{I}_{\omega,0}\mathrm{e}^{-\tau} + \int_0^\tau \mathrm{S}_\omega \mathrm{e}^{(\tau'-\tau)}\mathrm{d}\tau', \tag{2.7}$$

where $\mathrm{I}_{\omega,0}$ is the intensity of the emission prior to enter the region.

While this mechanism of emission was successfully detected from a uniform slab of plasma (Bekefi, 1966), it must be noted that the conditions under which the bremsstrahlung emission occurs are not compatible with conditions in an EAS (Gorham *et al.*, 2008). One particular theory of interest that is still under investigation is the relationship between the expected power at the aperture of a detector relative to the power of emission from electrons within the plasma, see § 2.3 for further discussion.

2.3 Detectability of Isotropic Microwave Emission

The total field strength at a specific point in time and space relative to an ensemble of radiating charged particles is simply the superposition of the fields from each emitter:

$$\overrightarrow{\mathrm{E}} = \sum_{\mathrm{i}=1}^{\mathrm{N_e}} \mathrm{E_i}\cos(\phi_\mathrm{i})\ \hat{\mathrm{k}}, \tag{2.8}$$

where $\mathrm{N_e}$ is the total number of electrons, i.e. emitters, $\mathrm{E_i}$ is the amplitude of the field generated by the i^{th} electron, ϕ_i is the phase of emission from the i^{th} electron, which takes into account the position of the electron relative to the point of evaluation. Furthermore, emission has been chosen to be along a single axis for simplicity and without loss in generality.

At the aperture of a detector, the power associated with the field may be determined by applying Poynting's theorem:

$$\left|\overrightarrow{S}\right| = \frac{P}{A} = \varepsilon_0 c \left|\overrightarrow{E}\right|^2, \tag{2.9}$$

where ε_0 is the permittivity of free space. Equation 2.9 shows that the power scales quadratically with the total field. Under the assumption that the emission from the electrons is completely coherent (i.e. $\phi_i = \phi_0$) and that the amplitude of emission is the same for each electron (i.e. $E_i = E_0$), Eq. 2.8 reduces to $\overrightarrow{E} = N_e E_0 \cos(\phi_0)\hat{k}$. As these conditions yield a linear relationship between the total field and number of particle, it immediately follows that the detected power would be a coherent sum described by

$$P_{coh} = N_e^2 P_1, \tag{2.10}$$

where P_1 is the power emitted by a single electron. In the case where the emission exhibits no coherence, resulting from a random distribution of phase angles, the detected power scales linearly with N_e:

$$P_{incoh} = N_e P_1. \tag{2.11}$$

Between the boundaries set by Eqs. 2.14 and 2.15, rests the scenario of partially coherent emission. Let us start by assuming that there are M subgroups of coherent emitters where each group has a total of μ_e members, $N_e = M\mu_e$. The power from such a subgroup would be

$$P_{coh,\,sub} = \mu_e^2 \, P_1. \tag{2.12}$$

Given that there are M total subgroups, then the detected power is defined by

$$P_{part} = M\mu_e^2 P_1. \tag{2.13}$$

As it would be most convenient to describe the coherence in terms of a single variable, as done in Alvarez-Muñiz *et al.* (2012), we may state that the total power detected is given by

$$P_{tot} = N_e^{\alpha} P_1, \tag{2.14}$$

where $\alpha = 1 + \frac{\log \mu_e}{\log N_e}$ quantitatively describes the degree of coherence, and is bounded on the interval [1, 2].

2.4 On the Measurements of Isotropic Microwave Emission from Air Showers

To establish a measurement of the microwave emission from an EAS, Gorham *et al.* (2008) performed a laboratory experiment at the Stanford Linear Accelerator Center using an electron particle beam to produce controlled showers with equivalent shower energies up to 10^{18} eV. One of the results from this analysis suggests that the microwave emission, in the extended C band (3.4 to 4.2 GHz), from an air shower should be coherent and yielded a reference flux density of $F_{ref} = 1.85 \times 10^{-15}$ W/m^2/Hz at shower maximum for a shower equivalent energy of $E_{ref} = 3.36 \times 10^{17}$ eV at a distance of 0.5 m. The minimum detectable flux of a receiver is given by

$$\Delta I_{\omega,\,min} = \frac{k_B T_{sys}}{A_{eff}\sqrt{\Delta t \Delta \nu}}, \tag{2.15}$$

where k_B is Boltzmann's constant, T_{sys} is the noise temperature of the receiver system, A_{Jeff} is the effective area of the antenna, Δt is the receiver sampling time constant, and $\Delta\nu$ is the receiver bandwidth. With the technology that is commercially available today, a minimum flux on the order of $\Delta I_{\omega,\,min} \propto 10^{-23}$ should be achievable, and a shower with a

flux density equal to the reference flux density, F_{ref}, should be detectable on the order of a few kilometers (i.e. assuming low anthropogenic noise).

Gorham *et al.* (2008) realized this and constructed a prototype detector named Air shower Microwave Bremsstrahlung Experimental Radiometer (AMBER) at the University of Hawaii at Manoa in hopes of observing isotropic microwave emission from EAS. Calibrations and a preliminary analysis were conducted and resulted in 10 candidate events considered to be consistent with expectations from an EAS; however, they could not be proven to be EAS without verification from a particle detector array. The AMBER detector is now stationed at the Pierre Auger Observatory and has yet to observed any signatures of isotropic microwave emission from EAS.

Two other experiments observing EAS in the microwave regime of the electromagnetic spectrum are the Cosmic-Ray Observation via Microwave Emission (CROME) experiment (Šmída, 2011) and the Extensive Air-Shower Identification using Electron Radiometer (EASIER) experiment (Williams, 2012). The experimental setups of both the CROME detector and the EASIER detector are very different from the AMBER detector. Nonetheless, they are also able to observe microwave emission in the extended C band. While both CROME and EASIER have detected microwave emission from EAS, the characteristics of the emission are attributed to the beamed emission resulting from the geomagnetic field and Askaryan effect. The detectors have yielded no evidence in support of isotropic microwave emission (Šmída *et al.*, 2014 and Gaior, 2013).

A similar analysis to the AMBER experiment, initiated at the University of Chicago, named the Microwave Detection of Air Showers (MIDAS) experiment constructed a detector to search for microwave emission from EAS (Williams, 2012, Alvarez-Muñiz *et al.*, 2012, and Alvarez-Muiz *et al.*, 2013). With a duty cycle estimated to be better than 95%, the detector's commissioning phase lasted several months consisting of the successful testing of components and calibration of the detector, a detailed account of which can be found in Alvarez-Muiz *et al.* (2013). In spite of a noisy urban environment, a science analysis was

also conducted and an initial constraint was established on the microwave emission from air showers (see Figure 2.1). After relocating the MIDAS experiment to the Pierre Auger Observatory in 2012, a second constraint, serving as a preliminary analysis, was set using 61 days of data while at the Pierre Auger Observatory (Williams, 2013). The results from this analysis are shown in Figure 2.2.

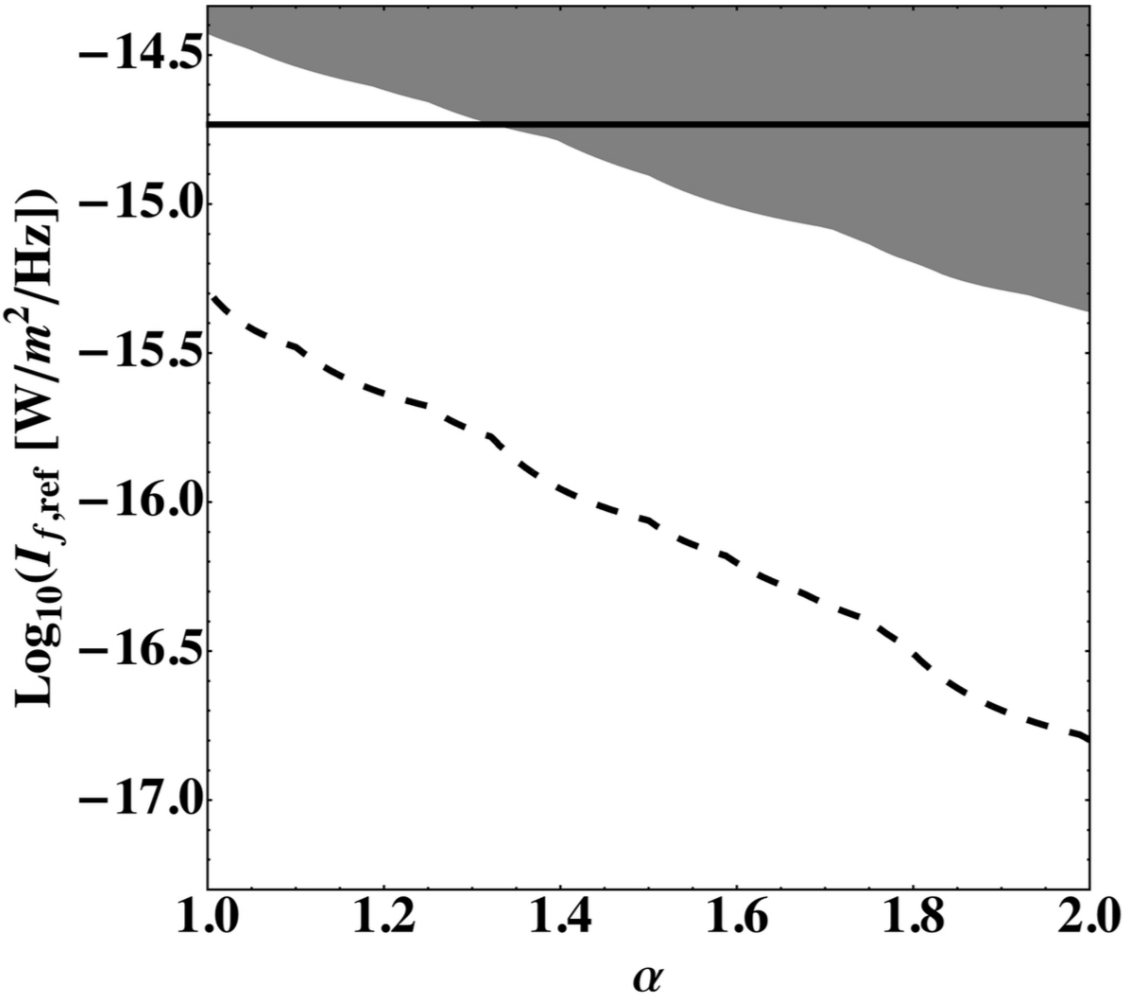

Figure 2.1: Exclusion limits on the microwave emission from UHECRs, obtained with 61 days of live time measurements with the MIDAS detector. The power flux $I_{f,\,ref}$ corresponds to a reference shower of 3.36×10^{17} eV, and the α parameter characterizes the possible coherence of the emission. The shaded area is excluded with greater than 95% confidence. The horizontal line indicates the reference power flux suggested by laboratory measurements (Gorham *et al.*, 2008). The projected 95% CL sensitivity after collection of one year of coincident operation data of the MIDAS detector at the Pierre Auger Observatory is represented by the dashed line. Figure acquired from Alvarez-Muñiz *et al.* (2012).

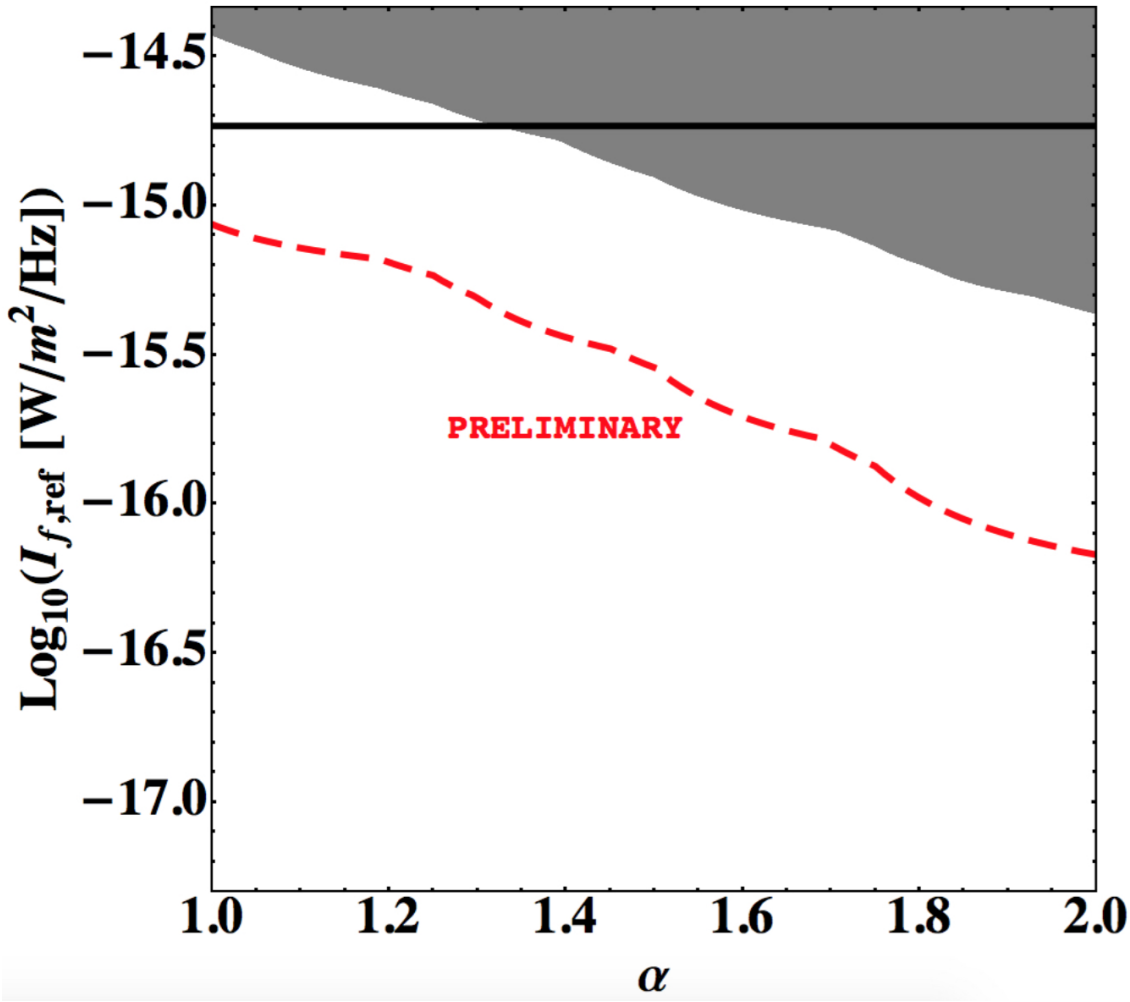

Figure 2.2: Same as previous plot but for 66 days of live time measurements taken with the MIDAS detector at the Pierre Auger Observatory (Red Dashed Line). Figure acquired from Williams (2013).

The MIDAS experiment has been stationed at the Pierre Auger Observatory since late 2012, and has been able to collect data in an environment of relatively low anthropogenic noise. In the next section, we present the defining traits of the MIDAS detector and report our updated constraint on microwave emission from EAS.

CHAPTER 3

MICROWAVE DETECTION OF AIR SHOWERS ANALYSIS

3.1 MIDAS Detector

The MIDAS detector, first commissioned at the University of Chicago in 2010 and currently installed at the Pierre Auger Observatory as seen in Figure 3.1, is a wide field of view telescope specifically designed for the purpose of detecting and characterizing the microwave emission from extensive air showers. A detailed description of the instrument can be found in Alvarez-Muiz *et al.* (2013). Equipped with a 5 m diameter parabolic antenna with a 53 pixel camera at its focus (3.2), the design of the MIDAS telescope is analogous to the design of one of the FDs at the Auger observatory as explained in § 1.3.1. Collectively, the 53 pixel ensemble covers approximately a $20^\circ \times 10^\circ$ field of view, and works together to observe microwave emission in the extended C band (3.4 to 4.2 GHz). Individually, each pixel is a channel composed of a feed horn, a low noise amplifier, and a frequency down converter. Radio waves detected by a channel are transformed into a radio equivalent analog signal which then undergoes digitization by one of four analog-to-digital converter (ADC) boards at a sampling rate of 20 MHz.

The four ADC boards are designed to accommodate 16 channels each and store a total of 2048 samples in a circular buffer per channel. In addition, each ADC board allows for a first level trigger (FLT) algorithm for each channel through an on-board field programmable gate array (FPGA). A Master Trigger board, which is connected to each ADC board, is equipped with its own FPGA which can execute a second level trigger (SLT) algorithm and read data from the ADC boards via a VME under the conditions outlined in § 3.1.1.

Figure 3.1: The MIDAS telescope at the Pierre Auger Observatory, with the 53-pixel camera mounted at the prime focus of the 5 m diameter parabolic dish reflector. Figure acquired from Williams (2013).

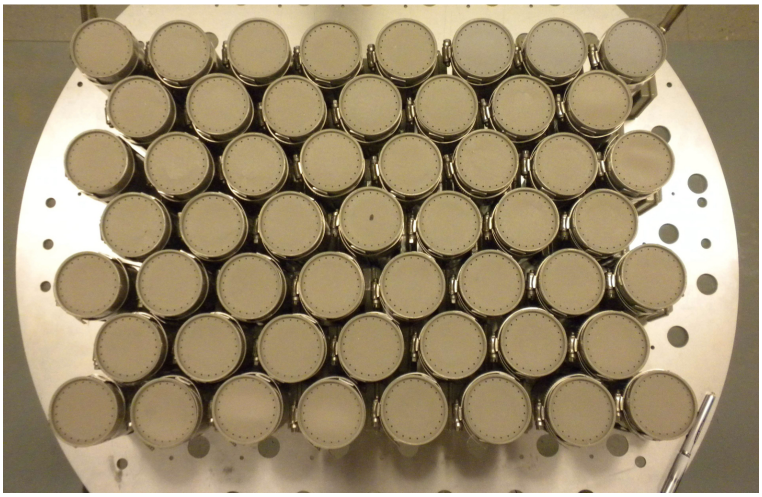

Figure 3.2: Image of the 53-pixel camera at the focus of the MIDAS telescope. Figure acquired from Alvarez-Muiz *et al.* (2013).

3.1.1 MIDAS FLT and SLT Triggers

Like the physical design of the MIDAS detector, the MIDAS triggering system is similar to the triggering system implemented in the Auger FDs. Each channel continuously detects microwaves in the frequency range from 3.4 to 4.2 GHz. Microwave emission detected during quiescent times help build baselines for background emission within each channel's FOV. The baselines are then used to set each channel's first level trigger threshold. As background signals fluctuate, the thresholds are quickly regulated to maintain a FLT rate close to 100 Hz per channel. To activate a channel's FLT, the detection of a microwave pulse with a moving average less than the channel's FLT threshold and a minimum width of 20 consecutive ADC sample counts (1 μs pulse) is required (see Figure 3.3). Upon triggering a FLT, a subsequent 10 μs window becomes active allowing for coincident FLT detections of the pulse of the shower by other channels. The data from the FLT channels are then transferred to the Master Trigger board for further analysis.

The FLT data sent to the Master Trigger board are used by the SLT algorithm to identify one of 767 possible 4-pixel patterns that have been deemed typical patterns resulting from EAS (see Figure 3.4). If one of the patterns is determined to be present within the FLT

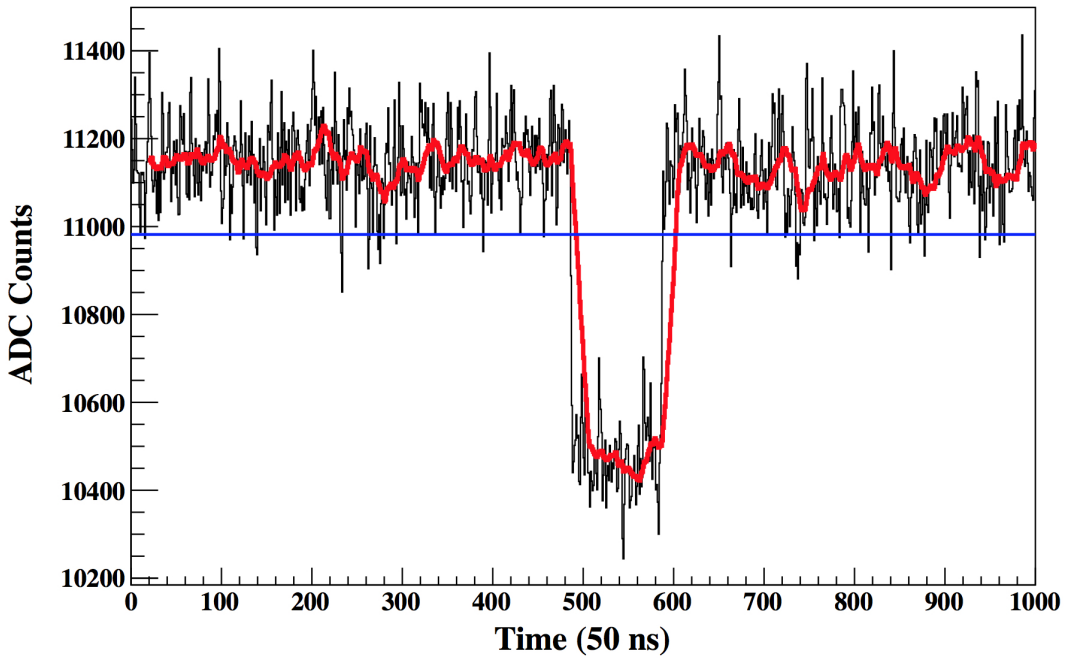

Figure 3.3: Illustration of the FLT. The digitized time trace for a 5 μs RF pulse, with the ADC running average of 20 consecutive time samples superimposed as a red histogram. An FLT is issued when the running average falls below the threshold, indicated by the horizontal line. Figure acquired from Alvarez-Muiz *et al.* (2013).

data, observation is temporarily halted and the data within each of the 53 channels' memory buffers are read out via the VME. A GPS unit tags each SLT events with a 10 ns precision timestamp.

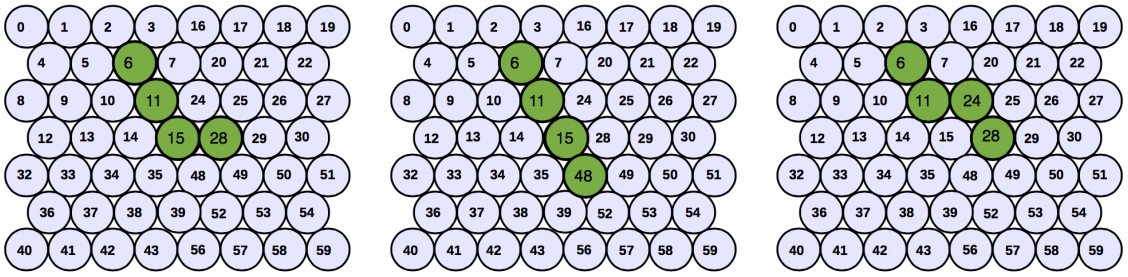

Figure 3.4: The basic patterns from which the 767 second level trigger patterns are composed. Figure acquired from Williams (2013).

3.2 MIDAS-Auger Time Coincidence Analysis

Candidate EAS events were searched for in the MIDAS dataset taken in the time interval from September 14, 2012 to September 26, 2014. Accounting for downtime of the MIDAS detector, the initial observational time window is 404 days and encompasses a total of 3,659,031 SLT events. The expected SLT rate due to accidental triggers, r_{bkg}, is estimated to be 0.3 mHz:

$$r_{bkg} = N_{patt} \cdot n_{pix} \cdot (r_{FLT})^{n_{pix}} (\tau)^{n_{pix}-1}, \tag{3.1}$$

where N_{patt} = 767 is the number of SLT patterns, n_{pix} = 53 is the number of pixels in the MIDAS camera, r_{FLT} = 100 Hz is the pixel FLT rate, and τ = 10 μs is the coincidence time window. However, rates as high as several kilohertz were observed during limited periods of time. The origin of these high rates were anthropogenic, e.g. from cars passing nearby, airplanes in the field of view, and the LIDAR atmospheric detector collocated with the MIDAS telescope. To decrease the number of chance coincidences resulting from periods of high ambient noise, we impose an event frequency no greater than 1 event per 2 seconds.

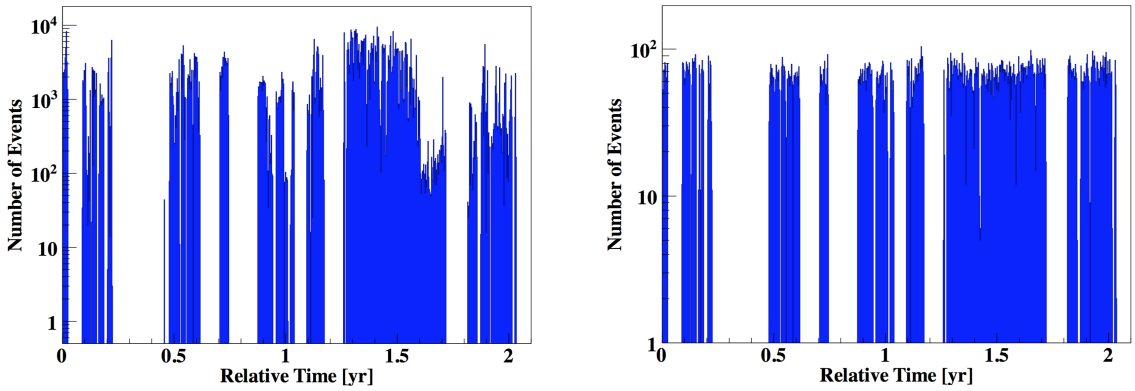

Figure 3.5: Left pane corresponds to the daily number of events detected by the MIDAS detector, and the right pane shows the daily number of events detected by the Auger SD.

Therefore, all events that occurred within a two second time window were removed from the analysis, which resulted in a remainder of 819,911 SLT events. This condition coupled with the time required to write SLT events to file and excluding time intervals corresponding to FLT rates exceeding 2.4 kHz yielded a total observational time window of about 359 days.

We proceed with the selection of events acquired by the Auger SD. Firstly, we require that all events have an energy greater than 10^{18} eV. As the Auger events are to be matched in time against the MIDAS dataset, removing events below 10^{18} eV is justified due to the low sensitivity of the MIDAS detector to events below this energy. Secondly, we require that the events satisfy the 6T5 condition, which is met if a T5 triggered station is surrounded by a hexagonal shape of 6 active stations that have passed trigger levels T3 or T4 (Sato, 2011). Thirdly, we require that the events' reconstructed cores are within $\pm$ 10 degrees of the MIDAS detector opening angle overlooking the Auger SD array. This requirement is essential as we want to eliminate the number of coincident detections with Auger events outside of the MIDAS detector's field of view. Lastly, we require that the timestamps of the selected Auger events overlap the periods in time in which the MIDAS detector was actively observing (see Figure 3.5). A total of 27,898 Auger events passed these selection criteria. Figure 3.6 shows the core positions of all Auger events considered for the analysis

in green and the events that passed event selection in blue.

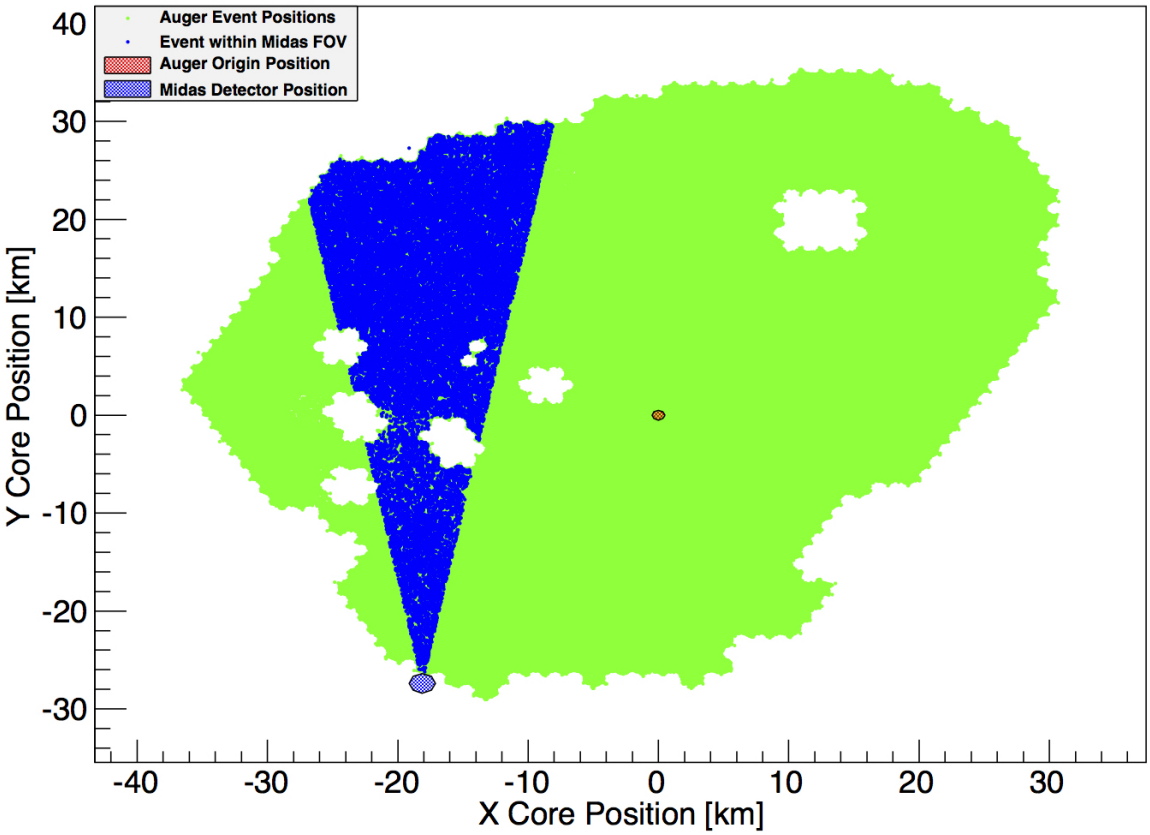

Figure 3.6: Core positions of all Auger events considered for analysis are represented by the green dots. The blue dots correspond to Auger events that passed the event selection process. The red-white checkered patch corresponds to the point of reference for all Auger SD events, and the blue-white checkered patch corresponds to the location of the MIDAS detector.

With events selected from both the Auger and MIDAS datasets, we performed a temporal event matching analysis. However, before beginning event matching, we corrected the timestamps of the MIDAS dataset by the appropriate amount of leap seconds as the time coordinates of the MIDAS and Auger datasets are UTC and GPS, respectively. We used the nanosecond precision timestamp of a single MIDAS event and found the nearest Auger event in time. The Auger event was considered to be coincident with the MIDAS event if the time difference, $\Delta t = t_{MIDAS} - t_{Auger}$, was in the interval of [-300, 300] μs, where negative differences in time correspond to the MIDAS event occurring before the Auger event.

This time interval was chosen to ensure that all showers landing on the SD array matched to events detected in the field of view of the MIDAS telescope would yield realistic time differences. Only one event fulfilled the Δt requirement and thus was considered to be a candidate shower. The distribution of time difference on the interval [-1, 1] for the entire MIDAS dataset is shown in Figure 3.7. Notice that the Δt distribution is flat as expected from random coincidence, and that no accumulation is observed around $\Delta t = 0$ as expected for true showers.

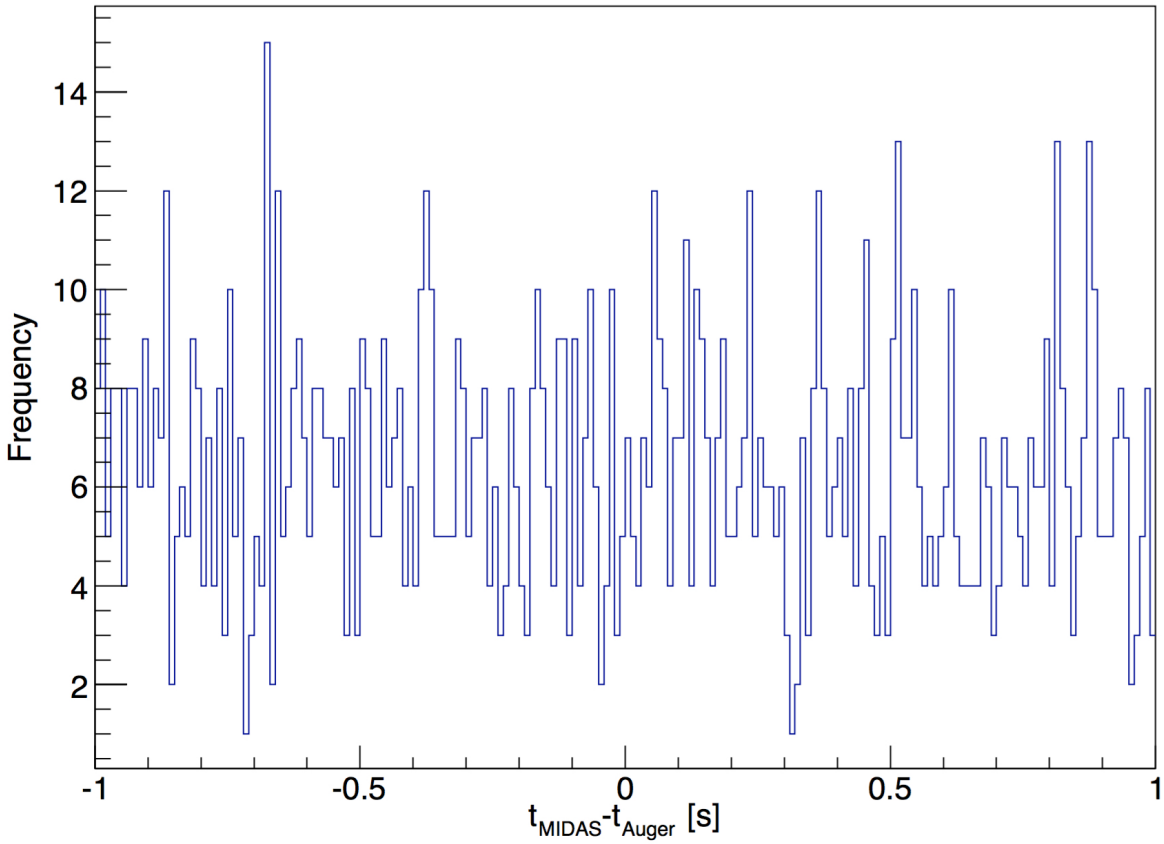

Figure 3.7: Distribution of time differences between matched MIDAS SLT event and Auger SD event in a 2 second window. Negative differences in time correspond to the MIDAS event occurring before the Auger event. Note that the shower geometry determines whether the SLT time occurs before or after the SD time.

To ascertain the validity of our single coincident event we used two independent methods to determine the number of coincident detections expected by chance. The first of the two methods starts with the assumptions that the Auger and MIDAS datasets are indepen-

dent of each other and are Poisson distributed. Under these assumptions, the probability of a single chance coincident event is given by,

$$P_c = P_A \cdot P_M = r_A r_M \tau^2 e^{-\tau(r_A + r_M)} \tag{3.2}$$

where the probabilities P_A and P_M are the respective probabilities of an Auger event and a MIDAS event, r_A and r_M are the event rates of the Auger SD and MIDAS detector, and τ is the window of time in which the coincident event occurs. We determined the event rates of both the Auger and Midas detectors by examining their respective distribution of average daily event rates seen in Figure 3.8. Due to periods of abnormally high event rates, we use the medians of the aforementioned distributions and find an Auger event rate of, $r_A = 8.86 \times 10^{-4}$ Hz, and a MIDAS event rate of, $r_M = 1.78 \times 10^{-2}$ Hz. Given the low values we obtain for r_A and r_M and the low value we adopt for our time window, $\tau = 600$ μs, the exponential in Eq. 3.2 approximately equals one, as can be determined by Taylor expansion, and we obtain a simpler form for the probability of a single chance coincident event, $P_c \approx r_A r_M \tau^2$. The chance coincidence rate is then given by $r_c = r_A r_M \tau$, and this yields a total number of chance coincidence given by the equation,

$$N_c = r_c \cdot t_{obs} = r_A r_M \tau t_{obs} \tag{3.3}$$

where t_{obs} is the total observational window of the MIDAS detector. Our analytical result yields an expected number of $N_c = 0.30$ (+0.55/-0.30) chance coincident events within a 359 day observational window, and indicates that our single coincident event agrees to within 2σ of the expected value resulting from chance coincidences.

For our second method of estimating the number of chance coincidences we shifted the timestamps of all Auger events by the same randomly generated constant; however, the shifting of the timestamps was performed in a manner that maintained the same number of events within a given day, as to not remove any clustering that may occur on the timescale

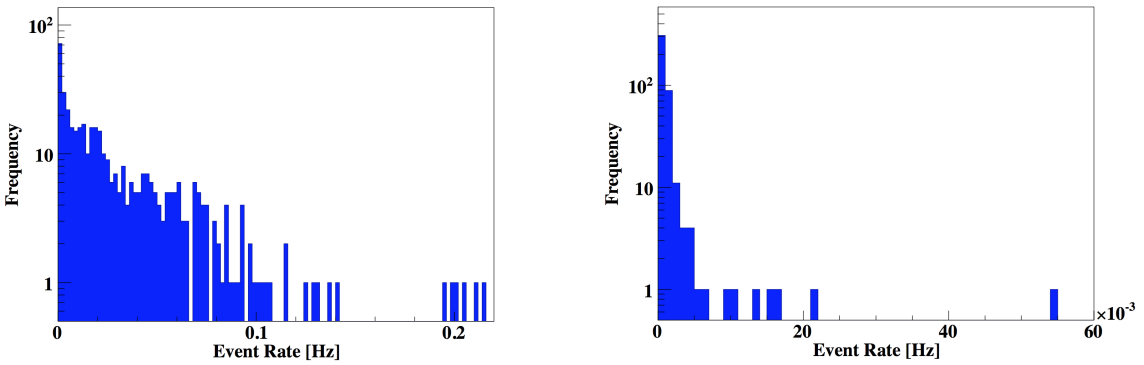

Figure 3.8: Left pane corresponds to the MIDAS daily average event rate, and the right pane shows the daily average event rate of the Auger SD.

of a single day. We repeated this process 10,000 times to build the probability distribution of chance coincidences as seen in Figure 3.9. The result we obtain from this method, N_c = 0.30 (+0.57/-0.30), not only agrees well with our analytical result but once again supports the idea the our single coincident event is most likely a statistical fluctuation.

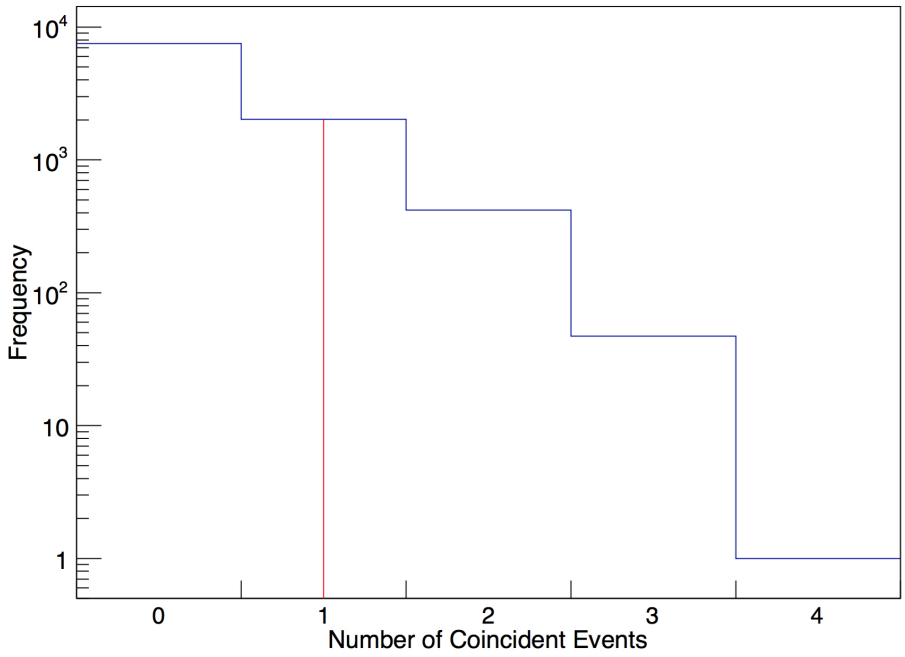

Figure 3.9: Distribution of chance coincidences. The red line indicates the number of coincident events determined in the real analysis.

For a final confirmation, we examine the properties of the coincident event. The re-

constructed core is at a distance of 52.94 km relative to the MIDAS detector, the energy of the event is 2.5 EeV, and the time difference between detection by the Auger and MIDAS detectors is 182 μs. While the reconstructed core distance yields a light travel time of 176 μs, justifying the time difference between the detections, an event of this energy at a distance of roughly 53 km should not produce a measurable signal at the aperture of the MIDAS detector. Furthermore, the track of the event across the MIDAS detector, shown in Figure 3.10, does not agree with any of the expected patterns produced by an EAS (see Figure 3.4). The evidence gathered from this analysis indicates that we have found no real coincidences and leads us to conclude that we have obtained a null result.

3.3 MIDAS Simulation

A Monte Carlo (MC) simulation was constructed to evaluate the sensitivity of the MIDAS detector to microwave emission from EAS. To provide a realistic simulation, data from solar calibrations performed in the analysis of Alvarez-Muiz *et al.* (2013) have been used to establish the optical characteristics of the MIDAS telescope. For a given assumption about the microwave reference flux, F_{ref}, and coherence scaling power, α, the simulation starts by generating the basic properties of an EAS: the shower energy and shower geometry. The shower energy is given by a user-defined fixed value. While the shower arrival direction is selected from a uniform distribution in both azimuthal and zenith angle, and the core position is randomly selected from a large area centered on the MIDAS telescope, both of which make up the shower geometry. With a shower energy and geometry selected, the simulation then models the development of an EAS through the Earth's atmosphere, where the development of the shower is determined by the number of charged particles generated at a given atmospheric depth. For this task, the simulation utilizes the Gaisser-Hillas function taking into account fluctuations that occur during the development of the shower.

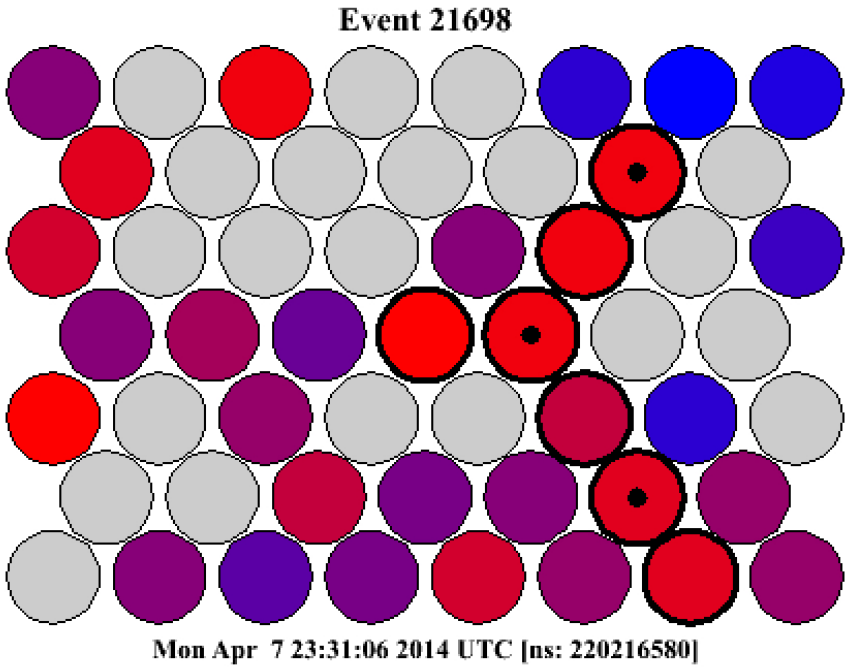

(a)

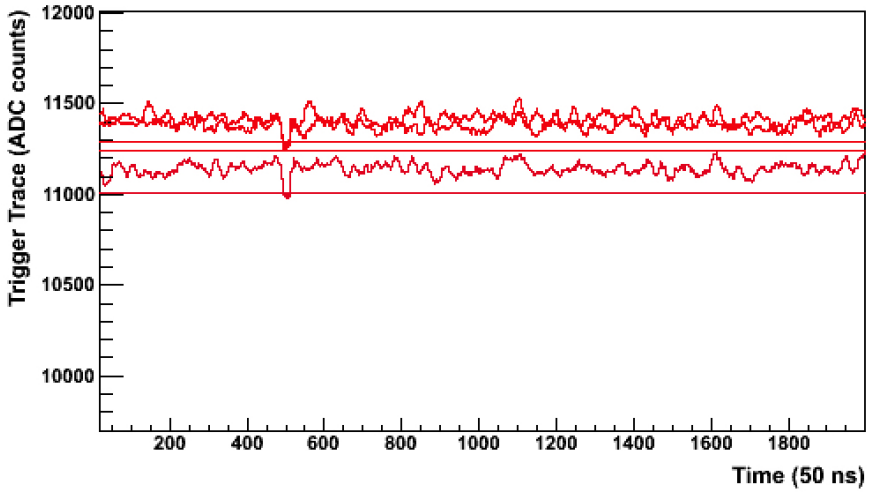

(b)

Figure 3.10: (a): Event display of the single event detected by the MIDAS telescope determined to be temporarily correlated with an Auger event by a time difference of 182 μ. (b): Trace of the detected pulse measured by the three selected detector pixels (pixels with black dots in (a)). Horizontal lines correspond to the selected pixels FLT thresholds.

The time dependent microwave flux observed by the detector is given by

$$F(t) = F_{ref} \cdot \frac{\rho(t)}{\rho_0} \cdot \left(\frac{d}{R(t)}\right)^2 \cdot \left(\frac{N(t)}{N_{ref}}\right)^{\alpha} \tag{3.4}$$

where F_{ref} is the microwave flux density of an air shower with energy $E_{ref} = 3.36 \times 10^{17}$ eV at a distance of d = 0.5 m, and produces an average of N_{ref} particles at shower maximum for a proton primary. The ratio $\rho(t)/\rho_0$ is the atmospheric density at the altitude of the EAS with respect to the density at sea level. R(t) is the distance between the detector and the segment of the EAS from which the detected emission originated, and N(t) is the number of particles generated by the shower at the time of emission. The simulation samples the number of particles generated, N(t), in time steps of 50 ns, calculates the microwave flux density across the MIDAS camera, and converts the flux into ADC counts per channel. Lastly, in accordance with the MIDAS detector, the simulation employs the first and second level trigger algorithms to determine if the generated shower would be detected by the MIDAS detector. This process is repeated until a statistically significant sample of random showers are generated or pass the SLT for energy bins greater than 10^{18} eV. An example of a simulated event is shown in Figure 3.11.

The method outlined above, along with the measured Auger energy spectrum and MIDAS exposure, could be used to estimate the number of expected events above 10^{18} eV that would be detected by the MIDAS detector. We have implemented a more precise approach by simulating showers that have the same energy and geometry as the selected T6 SD events described in § 3.2. For each shower we assume a pair of $\{I_{f,\,ref}, \alpha\}$ values and simulate the corresponding microwave emission and telescope response up to the SLT as previously described. For a given $\{I_{f,\,ref}, \alpha\}$ pair, this procedure determines the number of expected MIDAS SLT events for the set of selected SD events. Simulations were performed for a grid of values varying in logarithmic microwave flux density, $\log_{10}(I_{f,\,ref})$, from -17.3 to -14.3 in logarithmic steps of 0.1 and the coherence scaling power from 1 to 2 in steps of

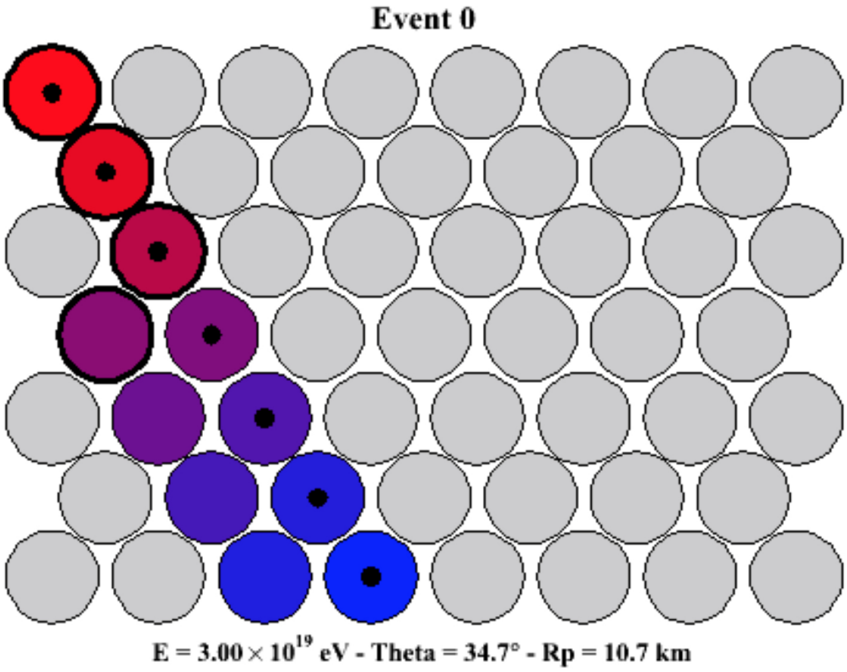

(a)

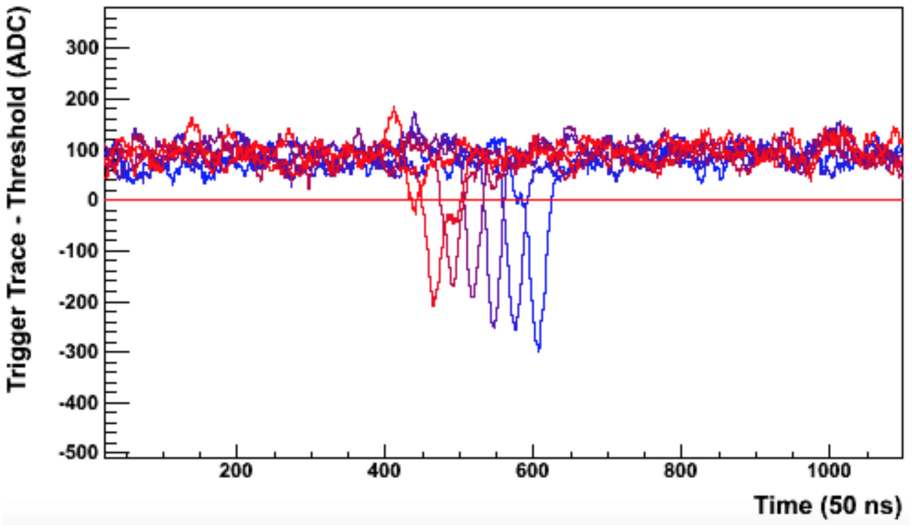

(b)

Figure 3.11: (a): Event display of the simulated event detected by the MIDAS telescope. (b): Trace of the detected pulse measured by several selected detector pixels (pixels with black dots in (a)). Horizontal line corresponds to the selected pixels FLT thresholds.

0.05.

3.4 Updated Constraints on Microwave Emission from Air Showers

Using the null result obtained in § 3.2, we update the constraints on the microwave emission from EAS established by Williams (2013) (see Figure 2.2). We calculate the 95% upper limit for the expected number of events using the confidence belt construction for a Poisson process with a background signal as outlined in Feldman and Cousins (1998). This classical approach to calculating confidence belts requires the mean background signal to be a known quantity. As shown in § 3.2, we have used two independent methods that agree well with each other and have determined the background signal to be $N_c = 0.30$ chance coincident events. The number of events obtained for each $\{I_{f,\,ref}, \alpha\}$ pair is compared to the corresponding number of events obtained by the MC explained in § 3.3. $\{I_{f,\,ref}, \alpha\}$ pairs where the MC derived number of events exceeds the statistical upper limit are ruled out, as shown in Figure 3.12.

As expected, we see that the updated constraints on the microwave emission from EAS excludes much more $\{I_{f,\,ref}, \alpha\}$ parameter space than that obtained in Williams (2012) preliminary analysis (see Figure 2.1). Also, the new constraints significantly exceeds the predicted estimate for one year of coincident data at the Pierre Auger Observatory by the MIDAS detector estimated in Alvarez-Muñiz *et al.* (2012) (see Figure 2.2). This improvement in the present analysis is due to a tighter coincident window ($\pm$ 300 μs versus $\pm$ 1 s) and to the lower background actually observed at the Pierre Auger Observatory. Notice that the present result unequivocally excludes the microwave flux claimed in the original paper of Gorham *et al.* (2008).

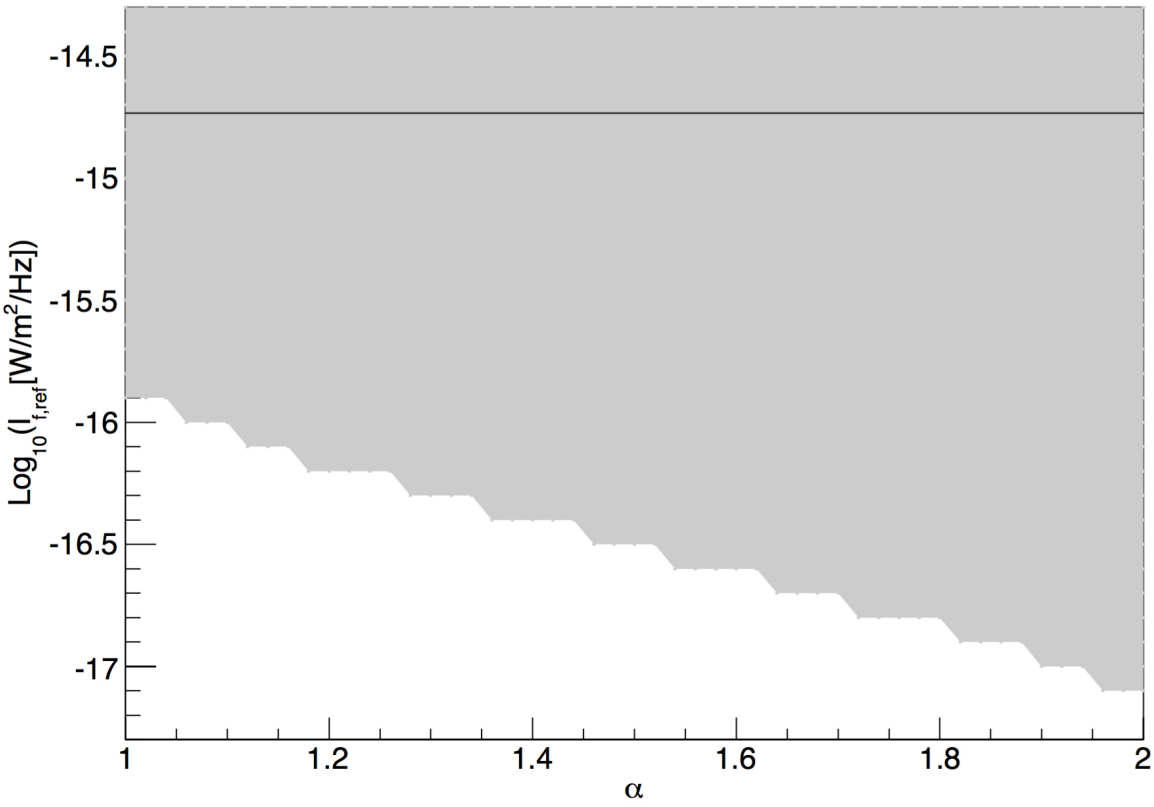

Figure 3.12: Updated exclusion limits on the microwave emission from EAS for an observational window of 359 days of data taken with the MIDAS detector at the Pierre Auger Observatory. Shaded region corresponds to ($I_{f,\,ref}$, α) pairs that have been rejected at least at a 95% confidence level. The horizontal line indicates the reference power flux suggested by laboratory measurements (Gorham *et al.*, 2008).

CHAPTER 4

CONSTRUCTION OF MOCK COSMIC RAY CATALOGS FOR FORWARD MODELING OF THE COSMIC RAY ENERGY SPECTRUM AND CLUSTERING

The cosmic ray energy spectrum exhibits a near perfect power law over many orders of magnitude in energy; however, as can be seen in Figure 1.1, the power law is broken multiple times: once at $\sim 3 \times 10^{15}$ eV, again at $\sim 4 \times 10^{18}$ eV, and, although not identified in Figure 1.1, at $\sim 5 \times 10^{19}$ eV. These features can only be explained by the intrinsic properties of the sources or by phenomena occurring during propagation.

With this fact in mind, many experiments have constructed models to explain these characteristic changes in the energy spectrum (see e.g. Blanton *et al.*, 2001, Alosio *et al.*, 2011, and Kido *et al.*, 2013). One particularly interesting approach is the use of forward modeling to produce mock cosmic ray catalogs. Under the assumption that the observed cosmic ray energy spectrum primarily results from knowledge of the source distribution, source injection spectrum, energy loss mechanisms during propagation, and the exposure and efficiency of a given detector, we may generate such catalogs via Monte Carlo simulation. Generally speaking, this can be done by starting at some defined initial state for the distribution of sources and their injection spectra, calculating energy losses during propagation, and ending with a record of "detected" cosmic rays yielding information in regards to the cosmic rays' source distances, arrival directions, and calculated final energies used to reconstruct the energy spectrum. The beauty of this approach is that it also allows for ancillary analyses such as the examination of the distribution of arrival directions of cosmic rays possibly helping to elucidate the suggested anisotropy of cosmic rays at the highest energies observed. In this chapter, we present the methodology of our model with the anticipation of using it in future analyses to not only reproduce features in the energy spectrum

at energies exceeding 3×10^{19} eV, but also provide a statistical analysis of the clustering of sources.

4.1 Energy Loss Calculations

Cosmic ray protons traversing the intergalactic medium interact with the photons of the cosmic microwave background resulting in the attenuation of energy (see § 1.2). As outlined in Achterberg *et al.* (1999) the mean energy loss can be calculated through a parameterization of the attenuation length, $\ell(\mathrm{E})$, defined by the equation

$$\ell(\mathrm{E}) = \left| \frac{1}{\mathrm{E}} \frac{\mathrm{dE}}{\mathrm{ds}} \right|^{-1} \tag{4.1}$$

for pair production, photo-pion production, and energy losses due to the expansion of the universe.

In the energy range $10^{17} \leq \mathrm{E} \leq 10^{18}$ eV, the dominant means of energy loss is due to propagation through an expanding universe. For this energy loss mechanism, the energy loss length, shown in Figure 4.1, is given by the Hubble length

$$\ell_{\mathrm{H}} = \frac{\mathrm{c}}{\mathrm{H}_0} = 4000 \text{ Mpc}, \tag{4.2}$$

where c is the speed of light and H_0 is the Hubble constant. The aforementioned energy range is not examined in our analysis, and is negligible compared to other energy loss mechanism. Nonetheless, we still compute the energy loss from this effect using a continuous energy loss approximation, $(\mathrm{dE/ds})_{\mathrm{H}}$ = -E/ℓ_{H}.

In the energy range $10^{18.5} \leq \mathrm{E} \leq 10^{19.5}$ eV, the dominant means of energy loss is due to the production of electron-positron pairs via interactions between cosmic ray protons and CMB photons (see Eq. 1.8). For this energy loss mechanism, we use the calculations presented in Blumenthal (1970) for the determination of the attenuation length ℓ_{p}. With an energy loss length no less than $\sim$ 1 Gpc, as seen in Figure 4.1, the reaction only produces a

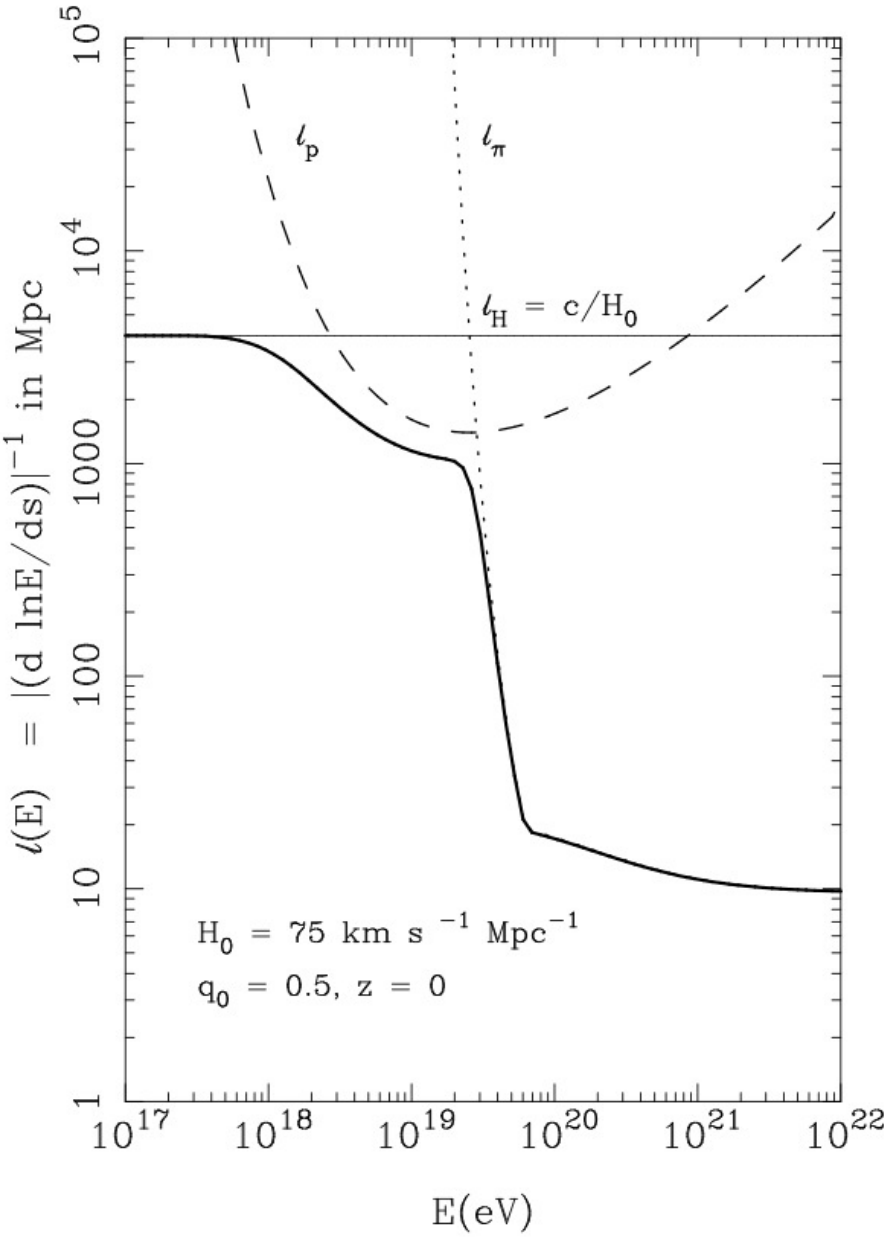

Figure 4.1: The energy loss length due to pion production (dotted curve), energy loss length due to pair production losses (dashed curve), and the energy loss length due to expansion of the universe (thin sold line), assuming that the universe is flat. The thick solid curve is the overall energy loss length considering all energy loss mechanisms. Figure acquired from Achterberg *et al.* (1999).

feeble change in the particle's energy (e.g. ℓ_p = 2 Gpc, $dE/E = 5\times10^{-4}$ % per megaparsec) and may be treated as a continuous energy loss mechanism, i.e. $(dE/ds)_p$ = -E/ℓ_p, at all energies of interest.

At the highest energies, $10^{19.5} < E$, cosmic ray protons have enough energy to produce pions through interactions with the CMB photons (see Eq. 1.9). Given the nature of this interaction, energy loss calculations from this effect must be treated differently than the continuous energy loss approximations used in determining energy losses due to the expansion of the universe and the production of electron-positron pairs. The amount of energy loss by this mechanism is significantly affected by the angular change in the trajectory of the cosmic ray proton as well as the number of incident CMB photons within a segment Δs.

We may start with the examination of the interaction in the observer's frame of reference. The total 4-vector momentum before the interaction, which is the sum of the 4-vector momenta of the CMB photon and proton, can most conveniently be described by

$$P_{before} = \left(\frac{i}{c}(\varepsilon + E_p), 0, 0, \frac{1}{c}\sqrt{\varepsilon^2 + E_p^2 - (m_p c^2)^2 + 2\varepsilon\cos\theta\sqrt{E_p^2 - (m_p c^2)^2}}\right) \tag{4.3}$$

where ε is the energy of the photon, E_p is the energy of the proton, and θ is the angle of incidence. The dot product of Eq. 4.3 with itself is invariant in all frames of reference. Therefore, examining the dot product in the proton rest frame (PRF), yields the invariant total energy

$$E_t^2 = P_{before} \cdot P_{before} = (m_p c^2)^2 + 2 m_p c^2 \varepsilon_0 \tag{4.4}$$

where ε_0 is the boosted photon energy in the PRF and, through Lorentz transformation back to the observer's frame, has the relationship $\varepsilon_0 = \gamma_p \varepsilon (1 - \beta_p cos\theta)$.

Upon evaluating the state of the resulting particles in the center of mass reference frame followed by Lorentz transformation back to the observer's frame of reference, the change

in the proton's energy per pion-producing interaction may be represented by

$$\Delta E_p^{\pi} = -E_p \left(K_p - \tilde{K} \cos\theta_{if} \right), \tag{4.5}$$

where θ_{if} is the angular change in the proton's trajectory after the collision, and $\cos\theta_{if}$ is uniformly distributed on the interval [-1, 1]. Equation 4.5 yields the change in energy of the proton as a function of the mean elasticity, K_p, and the intrinsic spread around the mean $\tilde{K}$. The mean elasticity may be approximated by

$$K_p = 0.2 \left(\frac{E_{th} + 2.5E_p}{E_{th} + E_p} \right), \tag{4.6}$$

where the proton threshold energy of the interaction is $E_{th} = \left(m_p m_\pi c^4 \right) / \left(2k_b T \right)$. The spread in energy has an approximation given by

$$\tilde{K} = \sqrt{\left(K_p + K_+ \right) \left(K_p - K_- \right)}, \tag{4.7}$$

with $K_\pm = m_\pi / \left(m_p \mp m_\pi \right)$. The approximations of K_p and $\tilde{K}$ as a function of proton energy are shown in Figure 4.2.

While Eq. 4.5 allows for the determination of the change in energy for each interaction, the total energy loss over a path length Δs is determined by the number of CMB photons encountered. For a sufficiently small path length Δs, the number of photons encountered is quite small and is subject to Poisson statistics. The average number of CMB photons along a path Δs capable of producing pions is given by

$$< N_{CMB} > (\Delta s) = \frac{\Delta s}{K_p \ell_\pi}, \tag{4.8}$$

with $\ell_\pi = c / \left(R_\pi \left(E_p \right) K_p \right)$ being the attenuation length associated with the production of pions. To calculate ℓ_π we use an approximation for the photo-pion interaction rate, R_π,

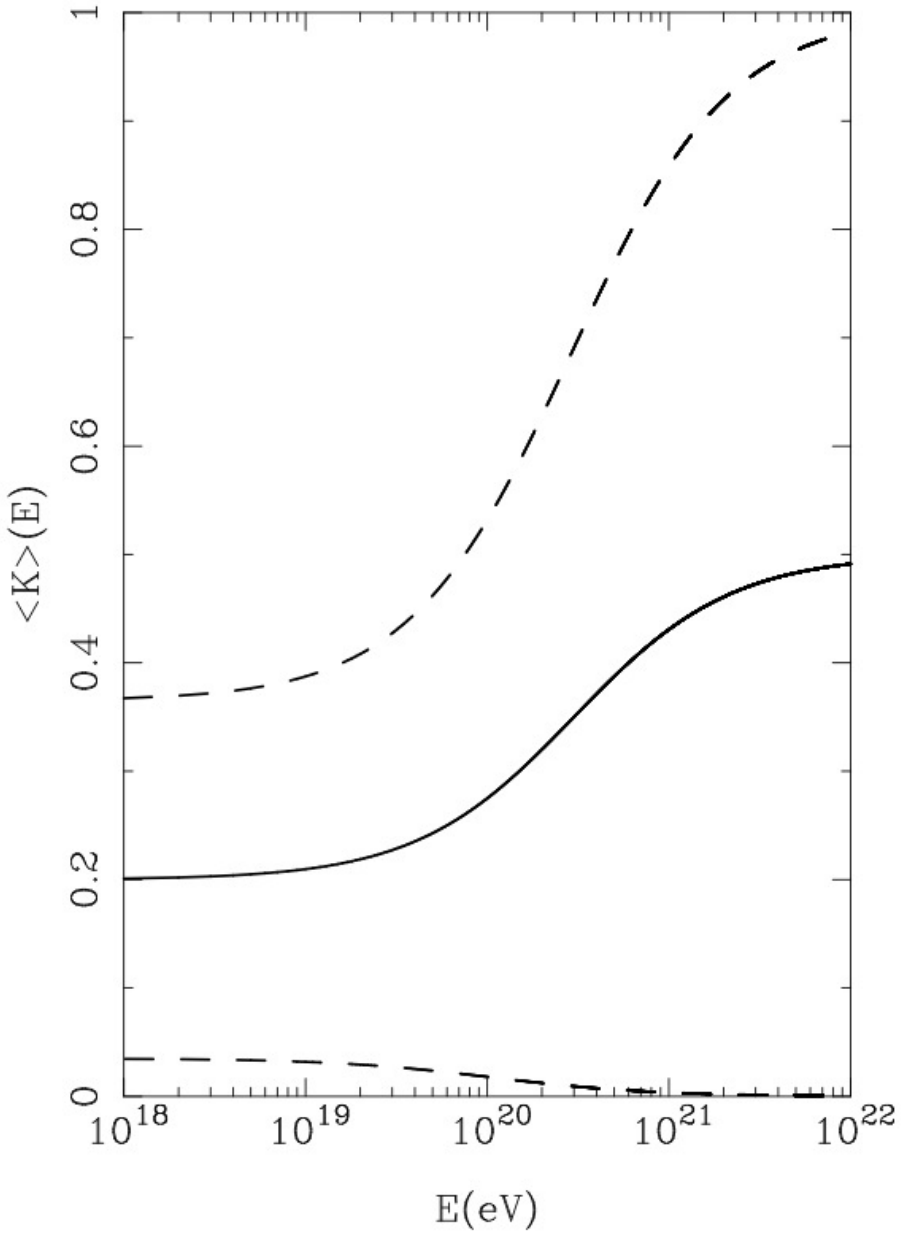

Figure 4.2: The mean inelasticity K_p (solid line) and the spread in energy, $\tilde{K}$ (dashed lines), resulting from the variance in the angular change in the proton's trajectory θ_{if}. Figure acquired from Achterberg *et al.* (1999).

given by the following piece-wise function

$$R_{\pi}\left(E_p\right) = \begin{cases} \frac{4}{\pi^2}\left(\frac{k_b T}{\hbar c}\right)^3 c\sigma_m \left(\frac{E_{th}}{E_p}\right)^2 e^{-\frac{E_{th}}{E_p}} & E_p \leq 0.2E_{th}, \\ 0.244\left(\frac{k_b T}{\hbar c}\right)^3 c\sigma_0 & E_p > 0.2E_{th}. \end{cases} \tag{4.9}$$

Corrections are applied to the aforementioned energy loss lengths due to physical differences in the past universe. Cosmic rays traversing the universe from large cosmological distances are exposed to a higher density of CMB photons at a higher temperature, i.e. $n_{CMB} \propto (1+z)^3$ and $T_{CMB} \propto (1+z)$. The corrected energy loss lengths associated with pair-production and pion-production is given by the scaling law

$$\ell\left(E, z\right) = \frac{\ell\left((1+z)E,\, z=0\right)}{(1+z)^3}, \tag{4.10}$$

where z is the redshift. Whereas the corrected energy loss length for expansion is given by

$$\ell_H = \left(\frac{c}{H_0}\right)(1+z)^{-\frac{3}{2}}. \tag{4.11}$$

4.2 Propagation Code

We have constructed a propagation code that computes the energy losses suffered by UHECR protons propagating through intergalactic space. Using the equations stated in § 4.1, the computation is performed only for cosmic rays with energies greater than or equal to 3×10^{19} eV (30 EeV) under the assumption that at these energies the cosmic ray energy spectrum is dominated by proton primaries.

For a cosmic ray of initial energy E traversing a distance L, the cosmic ray's change in energy is determined in steps of Δs, which we have chosen to be 200 kpc. Within the first step, the contribution from each energy loss mechanism is determined separately. In the cases where energy is attenuated by the expansion of the universe and the production of electron-positron pairs, the energy loss is determined by using continuous energy loss

approximations, such that $\Delta E_H = -E\left(\Delta s/\ell_H\right)$ and $\Delta E_p = -E\left(\Delta s/\ell_p\right)$. In the case where the energy loss mechanism is due to the production of pions, the average number of CMB photons within a segment Δs is first determined by using Eq. 4.8. The average number of CMB photons is then used to determine the total number of CMB photons, N_{CMB}, encountered by randomly drawing this value from a poisson distribution.

With the total number of CMB photons known, the change in energy is calculated for N_{CMB} encounters. The first encounter yields a change in energy determined by Eq. 4.5 and can be denoted as ΔE_1^{π}. The final energy obtained from the first interaction is then used as the initial energy in determining the change in energy for the second encounter yielding ΔE_2^{π}. This process is repeated until energy losses have been calculated for N_{CMB} encounters, and can be summarized as $\Delta E_{\pi} = \sum_{j=1}^{N_{CMB}} \Delta E_j^{\pi}$.

Once all energy loss mechanisms have been accounted for, their individual contributions are then added together to determine the total energy loss $\Delta E_i = \left(\Delta E_H + \Delta E_p + \Delta E_{\pi}\right)_i$ within the i^{th} length segment Δs. The final energy from the i^{th} step is then used as the initial energy for the subsequent step and energy loss calculations are performed as outlined above. This process is repeated until energy losses have been summed over the path length L yielding the total energy loss $\Delta E_{tot} = \sum_{i=1}^{n} \Delta E_i$, where $n = L/\Delta s$. In cases where Δs is not an integer multiple of L, n is increase by 1 to include the remaining segment and the value of Δs is set equal to the remaining path length and calculations proceed as outlined above.

A result from the process outline above is shown in Figure 4.3. As expected UHECR protons will gradually lose energy from the production of electron-positron pairs and expansion of the universe while propagating through intergalactic space; however, much of their energy (in the case of the scenario given by Figure 4.3 $\Delta E_{tot} \sim 2/3 E_{init}$) is diminished by the infrequent production of pions (see bottom pane of Figure 4.3). Significant energy losses by this process will continue until the cosmic ray reaches an energy $\sim E_{GZK}$. As this is expected to be the fate of all UHECR protons traveling over large cosmological distances, the highest energy cosmic rays (i.e. cosmic ray protons with $E > E_{GZK}$) observed

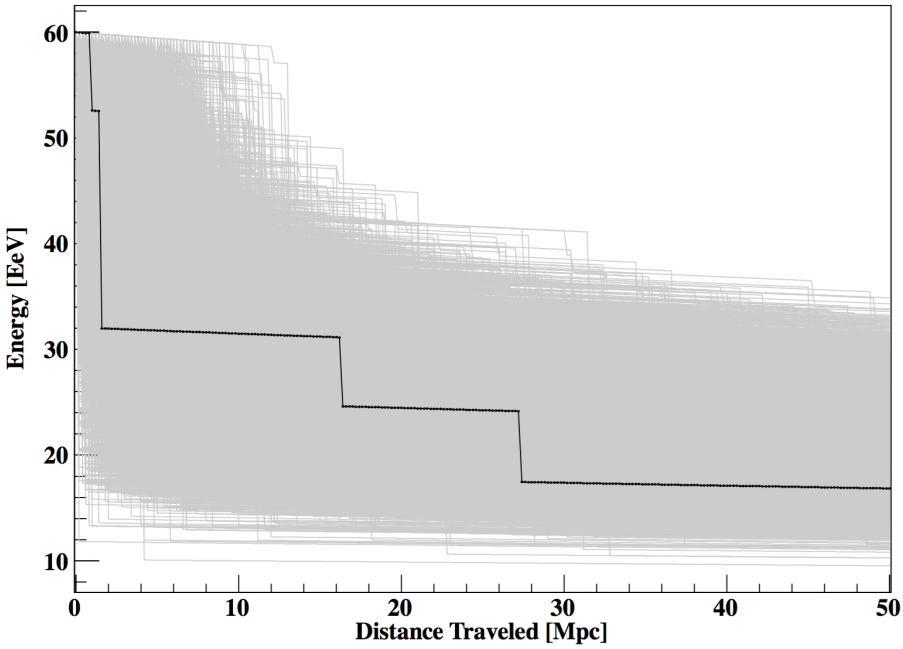

(a)

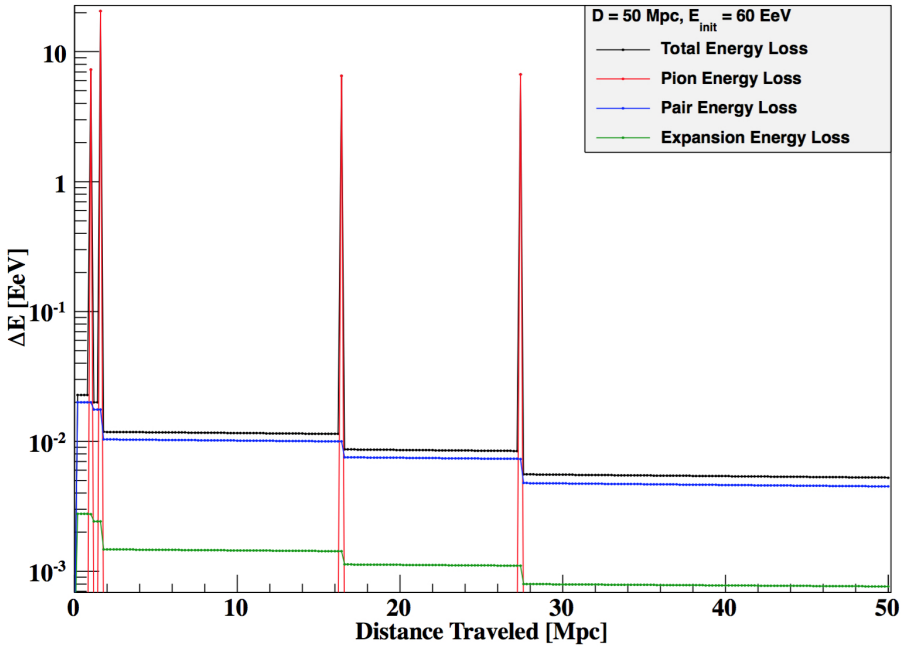

(b)

Figure 4.3: (a): Energy loss profiles (gray curves) for cosmic rays of initial energy 60 EeV traveling over a distance of 50 Mpc. The black curve corresponds to one of the profiles. Furthermore, the distribution of final energies can be obtained by taking the histogram of energies at 50 Mpc. (b): The total change in energy per 200 kpc (black line) for the black curve shown in (a). Individual contributions to the total change in energy are the result of losses due to pion production (red line), pair production (blue), and expansion of the Universe (green line).

must come from nearby sources.

4.3 Final Energy Probability Table

To increase the computational speed of our model, we have computed cumulative distribution functions from the final energy distributions for a grid of source distances and cosmic ray initial energies. For a given distance and initial energy we use the propagation code discussed in § 4.2 to obtain a final energy. As the energy loss due to pion-production is a stochastic process, different but similar final energy values can be obtained for the same source distance and cosmic ray initial energy by simply changing the seed to the random number generator per execution of the propagation code (see Figure 4.3). This action is performed 10,000 times and the resulting final energy distribution is then normalized to obtain the probability distribution function (PDF), several of which are shown in Figure 4.4. The PDF is then integrated to obtain the cumulative distribution function (CDF). This process is done for combinations of source distances between 0 to 250 Mpc in steps of 1 Mpc and cosmic ray initial energies between 30 EeV to 500 EeV in steps of 1 EeV. The result is a cube with dimensional coordinates of cosmic ray initial energy, source distance, and cosmic ray final energy, where a point within this space corresponds to a CDF value.

To obtain a final energy for a given source distance D and cosmic ray initial energy E, a random number is drawn from a uniform distribution and is then compared to the cumulative probability distribution for source distance D and initial energy E. The smallest final energy with CDF value greater than or equal to a number drawn from a uniform random distribution is chosen as the cosmic rays final energy. As seen in Figure 4.4, this method is in good agreement with final energies produced via the propagation code. Furthermore, final energies drawn from the table can be a factor of 100 times faster than final energies determined by the propagation code.

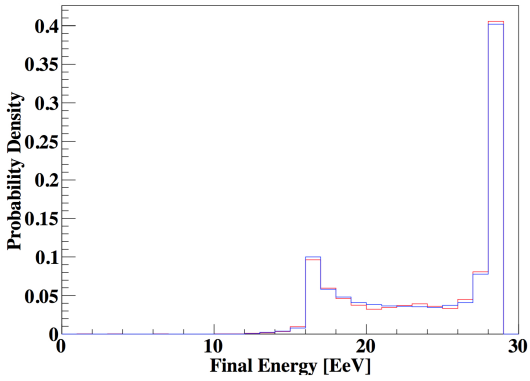

D = 25 Mpc, E_{init} = 30 EeV

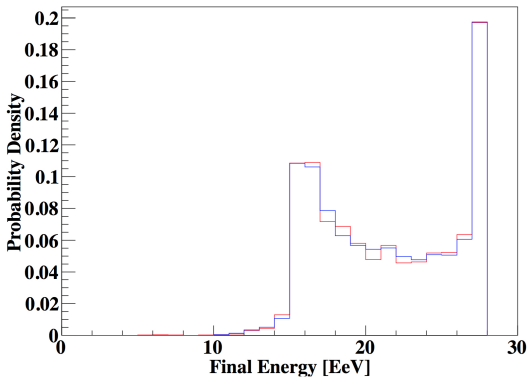

D = 50 Mpc, E_{init} = 30 EeV

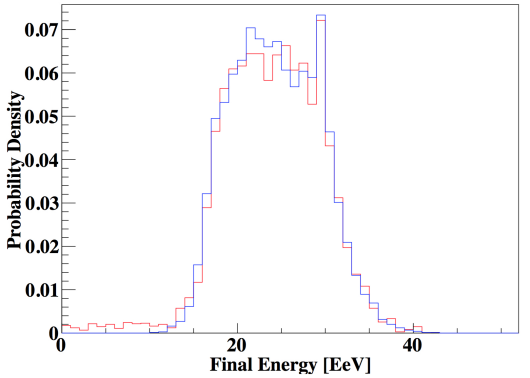

D = 25 Mpc, E_{init} = 60 EeV

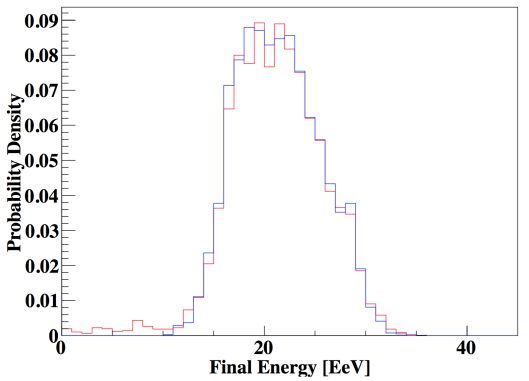

D = 50 Mpc, E_{init} = 60 EeV

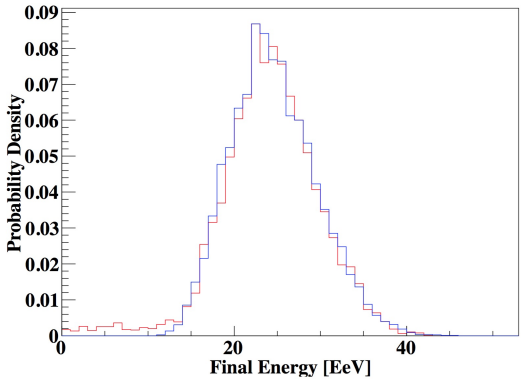

D = 25 Mpc, E_{init} = 90 EeV

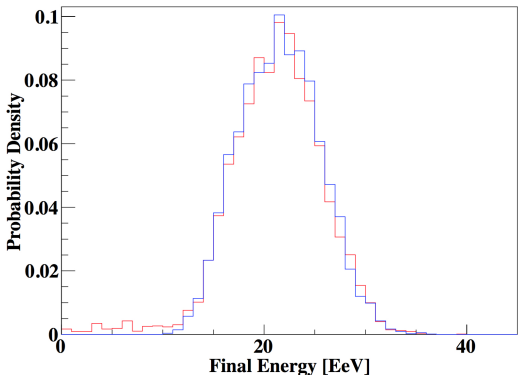

D = 50 Mpc, E_{init} = 90 EeV

Figure 4.4: Final energy probability distribution functions derived from the propagation code (blue curve) and the probability table (red curve) for several combinations of source distance, D, and cosmic ray proton initial energy, E_{init}.

4.4 Reconstruction of Cosmic Ray Energy Spectrum via Cosmic Ray Mock Catalogs

To better understand the features seen in the ultra high energy regime of the cosmic ray energy spectrum observed at Earth, we have constructed a Monte Carlo simulation that models the distribution of the cosmic ray sources, their injection spectra, and energy loss mechanisms encountered during propagation through intergalactic space. While our simulation is readily capable of evaluating a uniform source distribution and realistic distributions like the 2 Mass Redshift Survey catalog, we have selected a gaussian distribution of sources for testing purposes. Furthermore, we assume that the injection of cosmic rays from all sources follows a power-law spectrum, and that all cosmic rays generated are protons.

Firstly, the simulation randomly selects a source distance from a gaussian distribution of mean μ and standard deviation σ, both of which are free parameters. The source is then assigned a right ascension (RA), declination (DEC), and source ID. The right ascension is drawn from a uniform distribution, and the declination is drawn from the arcsine distribution to account for the skew in polar declination. The number of cosmic rays generated, N_{cr}, by the source is then determined by random selection from a poisson distribution where the mean is proportional to $\frac{1}{z^2}$, where z is the source redshift. An initial energy is then chosen for N_{cr} number of cosmic rays from a power-law distribution of the form $E^{-\gamma}$, where γ is a free parameter. Each cosmic ray's source ID, source distance, source RA, source DEC, and initial energy are then recorded. This process is used to generate three million events so that the source distribution is a good approximation of a gaussian, and to reduce the chance of selecting the same set events per mock energy spectrum explained below.

Once a list of generated comic rays has been compiled, the simulation proceeds by randomly drawing an event from the list. The event's final energy is randomly drawn from the probability distribution table based on source distance and initial energy as discussed in § 4.3. If a final energy can not be determined by the probability distribution table, which only occurs for the rare case when the initial energy is outside the range of initial energies

included in the table, the propagation code discussed in § 4.2 is used to obtain a final energy. After a final energy has been determined, it is then tested against our imposed minimum final energy of 30 EeV. Events that pass all selection criteria are considered "detected" events and are retained for the mock cosmic ray energy spectrum. It must be noted that we apply an arrival direction error of 1° to mimic the angular errors associated with events detected by Auger and that for testing purposes we use an all sky exposure.

For a given parameter set $\{\mu, \sigma, \gamma\}$, the process outlined above is repeated to produce 100 mock cosmic ray energy spectra using the same event list of three million events. The resulting energy spectra are then averaged together. This not only reduces statistical fluctuations but also allows us to estimate the uncertainty in the mock energy spectra we create. As we currently use 500 events per mock energy spectrum, which is similar to the number of events above 30 EeV reported in D'Urso (2014), an event list of 3 million events is enough to produce 100 mock energy spectra that are fairly independent of one another. Different parameter sets of $\{\mu, \sigma, \gamma\}$ use the same procedure outline above but with a newly generated event list.

Figure 4.5 shows mock energy spectra for several different combinations of mean source distance, μ, and injection spectral slope, γ, note that the standard deviation, σ, has been kept constant for all mock spectra. Under the assumption that our simulation correctly models the production, propagation, and detection of UHECRs, the scatter among the 100 mocks represents the observational error that would be achieved by 500 events above 30 EeV. We see that the generated mean spectra at high energies undergoes a suppression as the mean source distance is increased, this is an expected result due to the GZK effect. Additionally, the difference between the spectral slopes of mean mock energy spectrum at a μ value of 5 versus one produced at a μ value of 15, for constant γ, is larger than the scatter of either spectrum alone, indicating that 500 events is enough to distinguish between these two mean source distances. Lastly, when comparing differences between mean mock spectra with γ values of 2.1 to 2.5 but the same μ value, the mean spectra only show feeble

differences, which means that 500 events is not enough to examine differences between γ values of 2.1 to 2.5.

4.5 Probing Event Arrival Direction Distribution

One key observable obtained from cosmic ray air showers is the distribution of event arrival directions. As this is a property simulated in the construction of our mock energy spectra, we may perform an additional evaluation of the level of clustering of events on the sky. As a proof of concept, Figure 4.6 shows two independent distributions of the RAs and DECs of simulated events used to construct energy spectra, where the upper panel corresponds to 500 events arriving from sources that are uniform in RA and DEC and the lower panel corresponds to 500 events arriving from sources mapping the distribution of a sample of galaxies within the 2 Mass Redshift Survey. It is possible to take the analysis a step further by examining how these distributions change with increasing the number of events. In comparison to the upper panel of Figure 4.6, the upper panel of Figure 4.7 has a factor of four more events and clearly shows multiple clusters of events on the sky; however, the clusters are fairly uniform. In the lower panel of Figure 4.7, we see that the increase in the number of events served as a means of accentuating the clustering of events seen in the lower panel of Figure 4.6. The differences that can be seen between Figure 4.6 and Figure 4.7 is a perfect example of a plausible scenario arising from comparing the results obtained by a cosmic ray observatory at two distinct points in time. Lastly, we may enhance our examination of the clustering by examining how the distributions change as a function of source distance. As can be seen in both panels of Figure 4.8, most of the clustering appears to be associated with events from the nearest sources. The figures demonstrate that through the use of mocks catalogs we can explore different predictions of clustering for different source models and distances. Therefore, we can use clustering, in addition to the energy spectrum, to constrain source parameters.

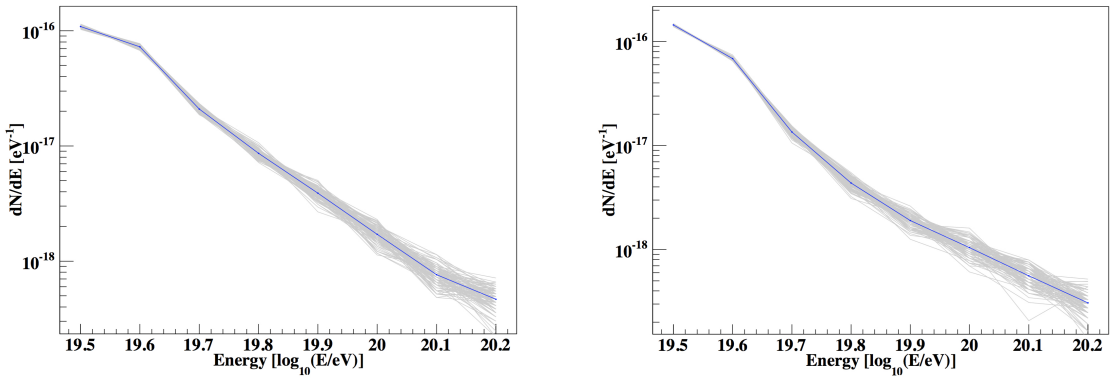

μ = 5 Mpc, γ = 2.1

μ = 15 Mpc, γ = 2.1

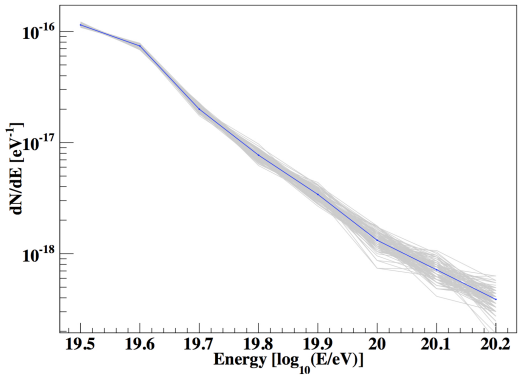

μ = 5 Mpc, γ = 2.3

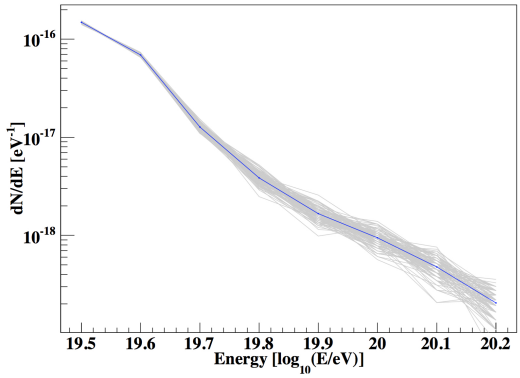

μ = 15 Mpc, γ = 2.3

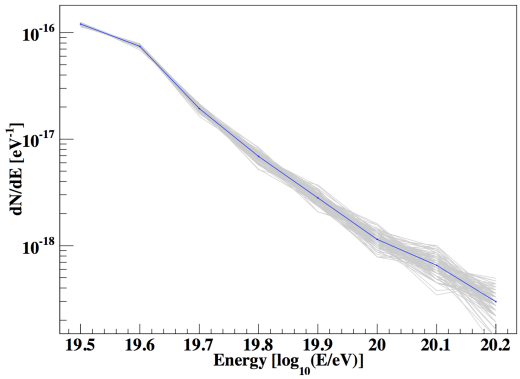

μ = 5 Mpc, γ = 2.5

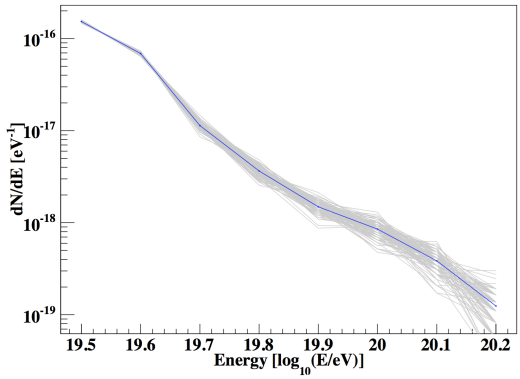

μ = 15 Mpc, γ = 2.5

Figure 4.5: Mock cosmic ray energy spectra (gray curves) for several combinations of mean source distance, μ, and injection spectral slope, γ. The source distance standard deviation, σ, has been kept at a constant value of 5 Mpc. The mean mock energy spectrum for a given value of μ and γ is given by a blue curve. Each mock spectrum is composed of 500 events above 3×10^{19} eV.

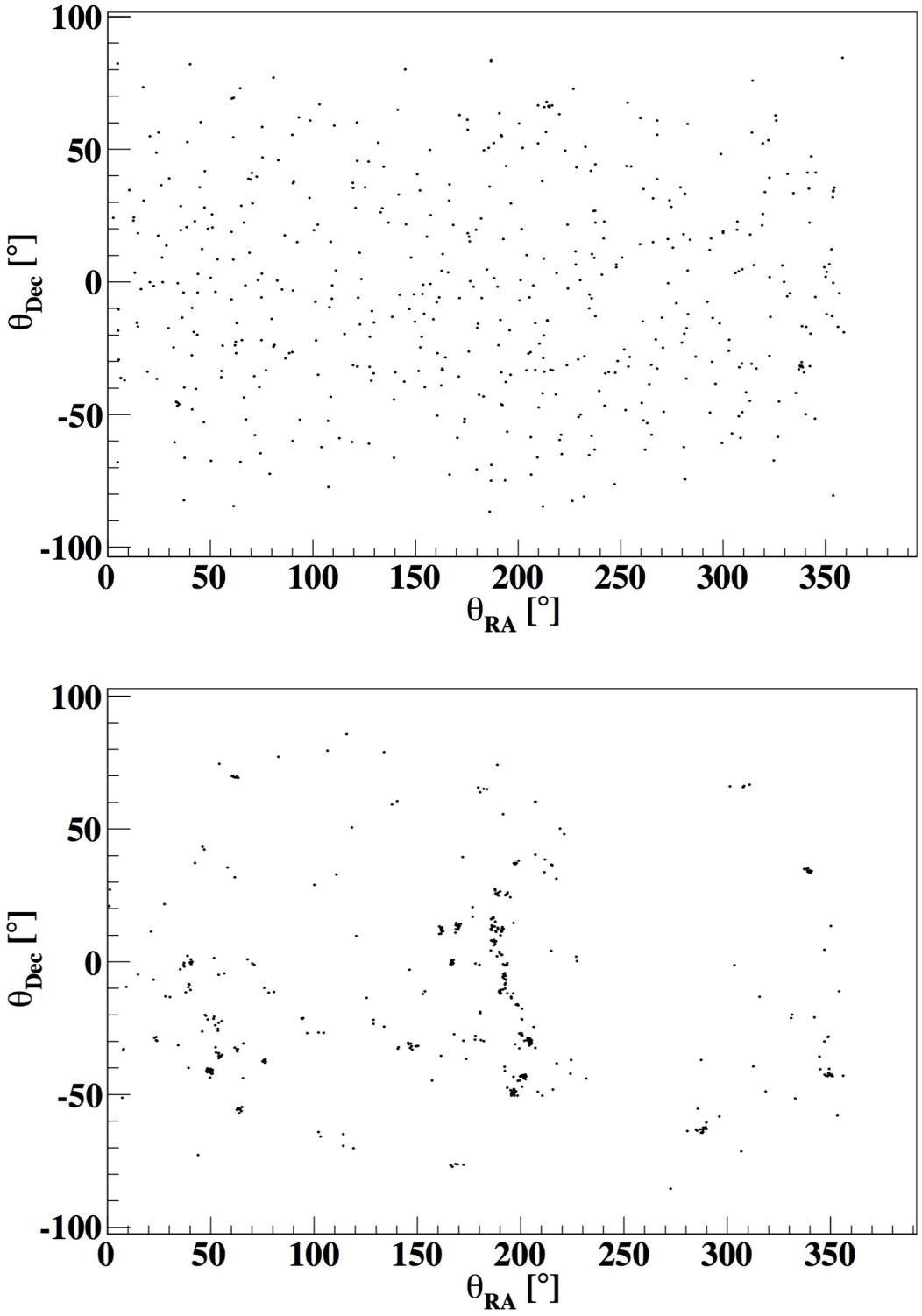

Figure 4.6: Right ascension and declination of simulated cosmic ray events. Upper panel plots the (RA, DEC) distribution of 500 generated events arriving from sources that are distributed uniformly in RA and DEC. Lower panel plots the (RA, DEC) distribution of 500 generated events arriving from sources that map a subset of galaxies from the 2 Mass Redshift Survey.

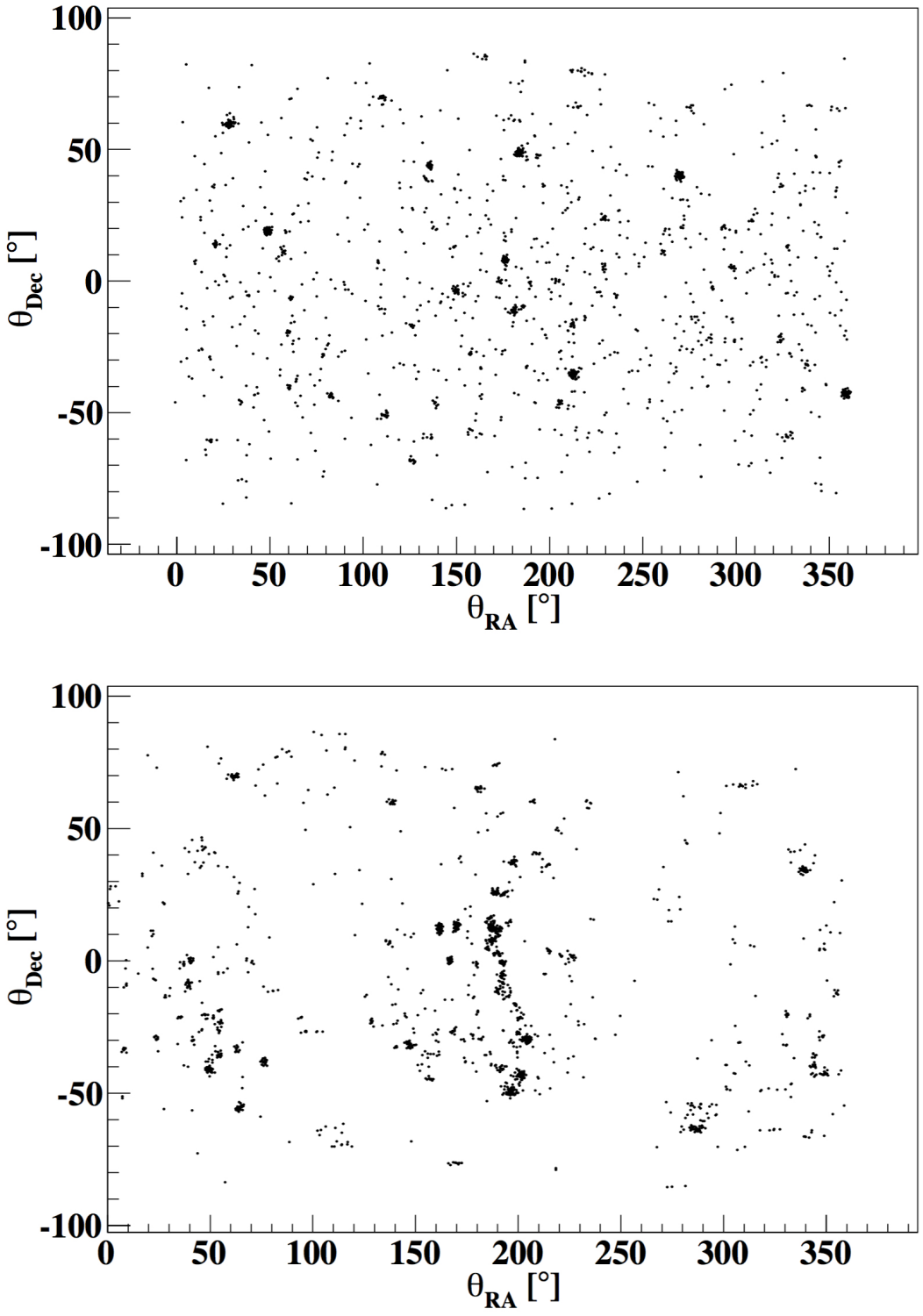

Figure 4.7: Same as Figure 4.6 but generated with 2000 events per distribution. Refer to Figure 4.6 for further explanation.

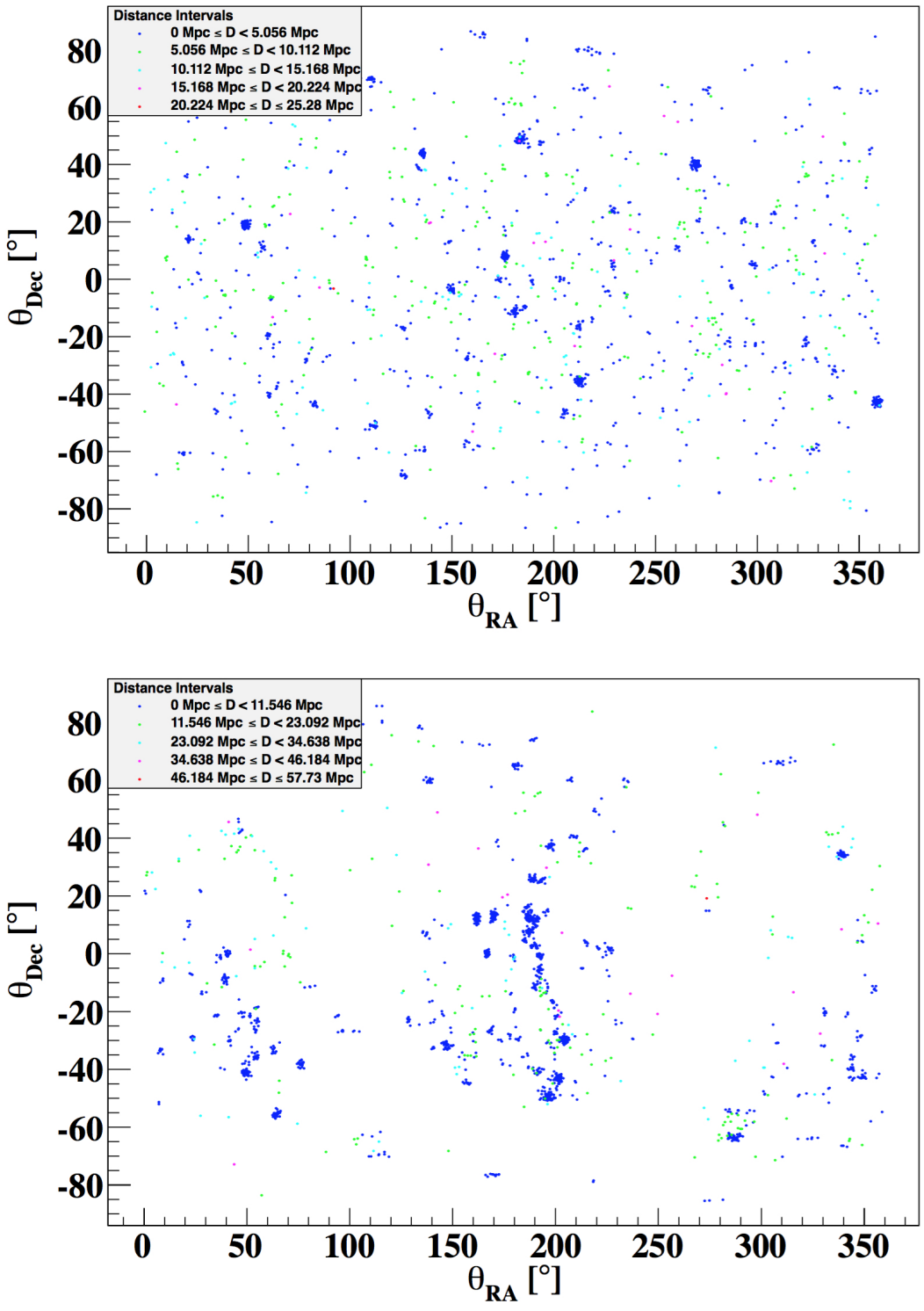

Figure 4.8: Same as Figure 4.7 with the addition of events color coded based on source distance. Refer to Figure 4.7 for further explanation.

4.6 Future Studies of UHECR Properties Using UHECR Mock Catalogs

Over the past century much has been learned about the UHECRs; however, their most fundamental properties (i.e., what are the sources and how do these sources accelerate the cosmic rays to such high energies) still remains a mystery. As we do not know what the sources are or the physics involved with injecting these particles into the universe, it is our hope that the construction and analysis of the mock catalogs we generate will elucidate parameters such as the source distance distribution, types of objects (e.g., AGN), and the shape of the injection spectrum. Since we know that these parameters will impact the observables like the energy spectrum and the anisotropy of samples like Auger, it brings much comfort in knowing that we have built a simulation that uses an ideal method by starting from the source parameters, constructing mock data, and predicting observables like the energy spectrum and anisotropy. We have built and tested the machinery of the model. In its current state, this model can be used in a parameter search to constrain parameters given any observed sample of UHECRs.

CHAPTER 5

CONCLUSIONS

5.1 Plausibility of Detection of EAS via Isotropic Microwave Emission

The constraint obtain from the time coincidence analysis between the MIDAS and Auger datasets has established stringent limits on isotropic microwave emission from EASs in the most ideal way. Figure 3.12 strongly suggests, at all possible levels of coherent emission from EASs, that the reference flux established by the laboratory experiment of Gorham *et al.* (2008) is not possible. The discrepancy between the results of our analysis and the results generated from Gorham *et al.* (2008) is most likely due to inconsistencies between the physical conditions of laboratory showers to that of real EASs. Very recent studies by Samarai *et al.* (2015) and Samarai *et al.* (2016) indicate that the expected isotropic microwave signal scaled to ten kilometers for a proton induced $10^{17.5}$ eV vertical shower measured in Gorham *et al.* (2008) is too high and have computationally calculated estimates that are up to two orders of magnitude lower. If valid, these estimated intensities would require detectors with significant enhancements in sensitivity, far beyond the sensitivity achievable by the current configuration of the MIDAS detector.

BIBLIOGRAPHY

[1] Aab, A., Abreu, P., Aglietta, M., Ahn, E.J., Samarai, I.A., Albuquerque, I.F.M., Allekotte, I., Allen, J., Allison, P., Almela, A., et al.: 2015, Searches for anisotropies in the arrival directions of the highest energy cosmic rays detected by the pierre auger observatory. *Astrophys. J.* **804**, 15. doi:10.1088/0004-637X/804/1/15.

[2] Abbasi, R.U., Abe, M., Abu-Zayyad, T., Allen, M., Anderson, R., Azuma, R., Barcikowski, E., Belz, J.W., Bergman, D.R., Blake, S.A., Cady, R., Chae, M.J., Cheon, B.G., Chiba, J., Chikawa, M., Cho, W.R., Fujii, T., Fukushima, M., Goto, T., Hanlon, W., Hayashi, Y., Hayashida, N., Hibino, K., Honda, K., Ikeda, D., Inoue, N., Ishii, T., Ishimori, R., Ito, H., Ivanov, D., Jui, C.C.H., Kadota, K., Kakimoto, F., Kalashev, O., Kasahara, K., Kawai, H., Kawakami, S., Kawana, S., Kawata, K., Kido, E., Kim, H.B., Kim, J.H., Kim, J.H., Kitamura, S., Kitamura, Y., Kuzmin, V., Kwon, Y.J., Lan, J., Lim, S.I., Lundquist, J.P., Machida, K., Martens, K., Matsuda, T., Matsuyama, T., Matthews, J.N., Minamino, M., Mukai, K., Myers, I., Nagasawa, K., Nagataki, S., Nakamura, T., Nonaka, T., Nozato, A., Ogio, S., Ogura, J., Ohnishi, M., Ohoka, H., Oki, K., Okuda, T., Ono, M., Oshima, A., Ozawa, S., Park, I.H., Pshirkov, M.S., Rodriguez, D.C., Rubtsov, G., Ryu, D., Sagawa, H., Sakurai, N., Sampson, A.L., Scott, L.M., Shah, P.D., Shibata, F., Shibata, T., Shimodaira, H., Shin, B.K., Smith, J.D., Sokolsky, P., Springer, R.W., Stokes, B.T., Stratton, S.R., Stroman, T.A., Suzawa, T., Takamura, M., Takeda, M., Takeishi, R., Taketa, A., Takita, M., Tameda, Y., Tanaka, H., Tanaka, K., Tanaka, M., Thomas, S.B., Thomson, G.B., Tinyakov, P., Tkachev, I., Tokuno, H., Tomida, T., Troitsky, S., Tsunesada, Y., Tsutsumi, K., Uchihori, Y., Udo,

S., Urban, F., Vasiloff, G., Wong, T., Yamane, R., Yamaoka, H., Yamazaki, K., Yang, J., Yashiro, K., Yoneda, Y., Yoshida, S., Yoshii, H., Zollinger, R., Zundel, Z., The Telescope Array Collaboration: 2014, Indications of intermediate-scale anisotropy of cosmic rays with energy greater than 57 eev in the northern sky measured with the surface detector of the telescope array experiment. *ArXiv e-prints*.

[3] Abraham, J., Abreu, P., Aglietta, M., Aguirre, C., Allard, D., Allekotte, I., Allen, J., Allison, P., Alvarez, C., Pierre Auger Collaboration: 2007, Correlation of the highest-energy cosmic rays with nearby extragalactic objects. *Science* **318**, 938. doi:10.1126/science.1151124.

[4] Abraham, J., Abreu, P., Aglietta, M., Aguirre, C., Allard, D., Allekotte, I., Allen, J., Allison, P., Alvarez-Muñiz, J., Pierre Auger Collaboration: 2008, Correlation of the highest-energy cosmic rays with the positions of nearby active galactic nuclei. *Astroparticle Physics* **29**, 188 – 204. doi:10.1016/j.astropartphys.2008.01.002.

[5] Abreu, P., Aglietta, M., Ahn, E.J., Allard, D., Allekotte, I., Allen, J., Alvarez Castillo, J., Alvarez-Muñiz, J., Ambrosio, M., Aminaei, A., et al.: 2010, Update on the correlation of the highest energy cosmic rays with nearby extragalactic matter. *Astroparticle Physics* **34**, 314 – 326. doi:10.1016/j.astropartphys.2010.08.010.

[6] Achterberg, A., Gallant, Y.A., Norman, C.A., Melrose, D.B.: 1999, Intergalactic propagation of uhe cosmic rays. In: Paul, J., Montmerle, T., Aubourg, E. (eds.) *19th Texas Symposium on Relativistic Astrophysics and Cosmology*.

[7] Ackermann, M., Ajello, M., Allafort, A., Baldini, L., Ballet, J., Barbiellini, G., Baring, M., Bastieri, D., Bechtol, K., Bellazzini, R., *et al.*: 2013, Detection of the characteristic pion-decay signature in supernova remnants. *Science* **339**(6121), 807 – 811.

[8] Adams, J.H., Ahmad, S., Albert, J.-N., Allard, D., Anchordoqui, L., Andreev, V., Anzalone, A., Arai, Y., Asano, K., Ave Pernas, M., Baragatti, P., Barrillon, P., Batsch, T.,

Bayer, J., Bechini, R., Belenguer, T., Bellotti, R., Belov, K., Berlind, A.A., Bertaina, M., Biermann, P.L., Biktemerova, S., Blaksley, C., Blanc, N., Błęcki, J., Blin-Bondil, S., Blümer, J., Bobik, P., Bogomilov, M., Bonamente, M., Briggs, M.S., Briz, S., Bruno, A., Cafagna, F., Campana, D., Capdevielle, J.-N., Caruso, R., Casolino, M., Cassardo, C., Castellini, G., Catalano, C., Catalano, O., Cellino, A., Chikawa, M., Christl, M.J., Cline, D., Connaughton, V., Conti, L., Cordero, G., Crawford, H.J., Cremonini, R., Csorna, S., Dagoret-Campagne, S., de Castro, A.J., De Donato, C., de la Taille, C., De Santis, C., del Peral, L., Dell'Oro, A., De Simone, N., Di Martino, M., Distratis, G., Dulucq, F., Dupieux, M., Ebersoldt, A., Ebisuzaki, T., Engel, R., Falk, S., Fang, K., Fenu, F., Fernández-Gómez, I., Ferrarese, S., Finco, D., Flamini, M., Fornaro, C., Franceschi, A., Fujimoto, J., Fukushima, M., Galeotti, P., Garipov, G., Geary, J., Gelmini, G., Giraudo, G., Gonchar, M., González Alvarado, C., Gorodetzky, P., Guarino, F., Guzmán, A., Hachisu, Y., Harlov, B., Haungs, A., Hernández Carretero, J., Higashide, K., Ikeda, D., Ikeda, H., Inoue, N., Inoue, S., Insolia, A., Isgrò, F., Itow, Y., Joven, E., Judd, E.G., Jung, A., Kajino, F., Kajino, T., Kaneko, I., Karadzhov, Y., Karczmarczyk, J., Karus, M., Katahira, K., Kawai, K., Kawasaki, Y., Keilhauer, B., Khrenov, B.A., Kim, J.-S., Kim, S.-W., Kim, S.-W., Kleifges, M., Klimov, P.A., Kolev, D., Kreykenbohm, I., Kudela, K., Kurihara, Y., Kusenko, A., Kuznetsov, E., Lacombe, M., Lachaud, C., Lee, J., Licandro, J., Lim, H., López, F., Maccarone, M.C., Mannheim, K., Maravilla, D., Marcelli, L., Marini, A., Martinez, O., Masciantonio, G., Mase, K., Matev, R., Medina-Tanco, G., Mernik, T., Miyamoto, H., Miyazaki, Y., Mizumoto, Y., Modestino, G., Monaco, A., Monnier-Ragaigne, D., Morales de los Ríos, J.A., Moretto, C., Morozenko, V.S., Mot, B., Murakami, T., Nagano, M., Nagata, M., Nagataki, S., Nakamura, T., Napolitano, T., Naumov, D., Nava, R., Neronov, A., Nomoto, K., Nonaka, T., Ogawa, T., Ogio, S., Ohmori, H., Olinto, A.V., Orleański, P., Osteria, G., Panasyuk, M.I., Parizot, E., Park, I.H., Park, H.W., Pastircak, B., Patzak, T., Paul, T., Pennypacker, C.,

Perez Cano, S., Peter, T., Picozza, P., Pierog, T., Piotrowski, L.W., Piraino, S., Plebaniak, Z., Pollini, A., Prat, P., Prévôt, G., Prieto, H., Putis, M., Reardon, P., Reyes, M., Ricci, M., Rodríguez, I., Frías, M.D.R., Ronga, F., Roth, M., Rothkaehl, H., Roudil, G., Rusinov, I., Rybczyński, M., Sabau, M.D., Sáez Cano, G., Sagawa, H., Saito, A., Sakaki, N., Sakata, M., Salazar, H., Sánchez, S., Santangelo, A., Santiago Crúz, L., Sanz Palomino, M., Saprykin, O., Sarazin, F., Sato, H., Sato, M., Schanz, T., Schieler, H., Scotti, V., Segreto, A., Selmane, S., Semikoz, D., Serra, M., Sharakin, S., Shibata, T., Shimizu, H.M., Shinozaki, K., Shirahama, T., Siemieniec-Oziębło, G., Silva López, H.H., Sledd, J., Słomińska, K., Sobey, A., Sugiyama, T., Supanitsky, D., Suzuki, M., Szabelska, B., Szabelski, J., Tajima, F., Tajima, N., Tajima, T., Takahashi, Y., Takami, H., Takeda, M., Takizawa, Y., Tenzer, C., Tibolla, O., Tkachev, L., Tokuno, H., Tomida, T., Tone, N., Toscano, S., Trillaud, F., Tsenov, R., Tsunesada, Y., Tsuno, K., Tymieniecka, T., Uchihori, Y., Unger, M., Vaduvescu, O., Valdés-Galicia, J.F., Vallania, P., Valore, L., Vankova, G., Vigorito, C., Villaseñor, L., von Ballmoos, P., Wada, S., Watanabe, J., Watanabe, S., Watts, J., Weber, M., Weiler, T.J., Wibig, T., Wiencke, L., Wille, M., Wilms, J., Włodarczyk, Z., Yamamoto, T., Yamamoto, Y., Yang, J., Yano, H., Yashin, I.V., Yonetoku, D., Yoshida, K., Yoshida, S., Young, R., Zotov, M.Y., Zuccaro Marchi, A.: 2015, The jem-euso mission: An introduction. *Experimental Astronomy* **40**(1), 3 – 17. doi:10.1007/s10686-015-9482-x. http://dx.doi.org/10.1007/s10686-015-9482-x.

[9] Alosio, R., Berezinsky, V., Gazizo, A., *et al.*: 2011, Ultra high energy cosmic rays: The disappointing model. *Astropart. Phys.* **34**, 620 – 626.

[10] Alvarez-Muñiz, J., Berlin, A., Bogdan, M., Boháčová, M., Bonifazi, C., Carvalho Jr, W., de Mello Neto, J., San Luis, P.F., Genat, J., Hollon, N., *et al.*: 2012, Search for microwave emission from ultrahigh energy cosmic rays. *Physical Review D* **86**(5), 051104.

[11] Alvarez-Muiz, J., Soares, E.A., Berlin, A., Bogdan, M., Bohov, M., Bonifazi, C., Jr., W.R.C., de Mello Neto, J.R.T., Luis, P.F.S., Genat, J.F., Hollon, N., Mills, E., Monasor, M., Privitera, P., de Castro, A.R., Reyes, L.C., Richardson, M., d'Orfeuil, B.R., Santos, E.M., Wayne, S., Williams, C., Zas, E., Zhou, J.: 2013, The MIDAS telescope for microwave detection of ultra-high energy cosmic rays. *Nuclear Instruments and Methods in Physics Research Section A: Accelerators, Spectrometers, Detectors and Associated Equipment* **719**, 70 – 80. doi:http://dx.doi.org/10.1016/j.nima.2013.03.030. http://www.sciencedirect.com/science/article/pii/S0168900213003185.

[12] Arqueros, F., Hörandel, J.R., Keilhauer, B.: 2008, Air fluorescence relevant for cosmic-ray detection — summary of the 5th fluorescence workshop, el escorial 2007. *Nuclear Instruments and Methods in Physics Research A* **597**, 1 – 22. doi:10.1016/j.nima.2008.08.056.

[13] Barnhill, D., Baulea, P., Dova, M.T., Harton, J., Knapik, R., Knapp, J., Lee, J., Mancenido, M., Mariazzi, A.G., Maris, I.C., Newton, D., Roth, M., Schmidt, T., Watson, A.A., Collaboration, P.A.: 2005, Measurement of the lateral distribution function of uhecr air showers with the pierre auger observatory. *International Cosmic Ray Conference* **7**, 291.

[14] Beatty, J.J., Westerhoff, S.: 2009, The highest-energy cosmic rays. *Annu. Rev. Nucl. Part. Sci.* **59**, 319 – 345.

[15] Bekefi, G.: 1966, *Radiation processes in plasmas*, *Wiley series in plasma physics*, Wiley, ??? https://books.google.com/books?id=UuNEAAAAIAAJ.

[16] Belletoile, A.: 2011, First results of the new autonomous antenna array of the codalema radio detection experiment. *International Cosmic Ray Conference* **1**, 231. doi:10.7529/ICRC2011/V01/0299.

[17] Bhattacharjee, P., Sigl, U.: 2000, Origin and propagation of extremely high-energy cosmic rays. *Physics Reports* **327**, 109 – 247.

[18] Blanton, M., Blasi, P., Olinto, A.V., *et al.*: 2001, The gzk feature in our neighborhood of the universe. *Astropart. Phys.* **15**, 275 – 286.

[19] Blumenthal, G.R.: 1970, Energy loss of high-energy cosmic rays in pair-producing collisions with ambient photons. *Phys. Rev. D* **1**, 1596 – 1602. doi:10.1103/PhysRevD.1.1596. http://link.aps.org/doi/10.1103/PhysRevD.1.1596.

[20] Conceição, R., for the Pierre Auger Collaboration: 2013, The pierre auger observatory: results on the highest energy particles. *ArXiv e-prints*.

[21] D'Urso, D.: 2014, Cosmic ray physics. *ArXiv e-prints*.

[22] Elyiv, A.A., Hnatyk, B.I.: 2004, The time delay of extragalactic cosmic rays in the galactic magnetic field. *Odessa Astronomical Publications* **17**(3), 30.

[23] Falcke, H., Gorham, P., Protheroe, R.J.: 2004, Prospects for radio detection of ultra-high energy cosmic rays and neutrinos. *New Astron. Rev.* **48**, 1487 – 1510. doi:10.1016/j.newar.2004.09.028.

[24] Feldman, G.J., Cousins, R.D.: 1998, Unified approach to the classical statistical analysis of small signals. *Phys. Rev. D* **57**, 3873 – 3889. doi:10.1103/PhysRevD.57.3873.

[25] Fermi, E.: 1949, On the origin of the cosmic radiation. *Phys. Rev.* **75**, 1169 – 1174.

[26] Fraschetti, F.: 2008, On the acceleration of ultra-high-energy cosmic rays. *Phil. Trans. R. Soc.* **366**, 4417 – 4428.

[27] Fraschetti, F., Melia, F.: 2008, Ultra-high-energy cosmic rays from the radio lobes of active galactic nuclei. *Mon. Not. Roy. Astron. Soc.* **391**, 1100 – 1106.

[28] Gaior, R.: 2013, Detection of cosmic rays using microwave radiation at the pierre auger observatory. In: *Proceedings, 33rd International Cosmic Ray Conference (ICRC2013): Rio de Janeiro, Brazil, July 2-9, 2013*, 0883. http://www.cbpf.br/%7Eicrc2013/papers/icrc2013-0883.pdf.

[29] Gorham, P.W., Lehtinen, N.G., Varner, G.S., Beatty, J.J., Connolly, A., Chen, P., Conde, M.E., Gai, W., Hast, C., Hebert, C.L., Miki, C., Konecny, R., Kowalski, J., Ng, J., Power, J.G., Reil, K., Ruckman, L., Saltzberg, D., Stokes, B.T., Walz, D.: 2008, Observations of microwave continuum emission from air shower plasmas. *Phys. Rev. D* **78**, 032007. doi:10.1103/PhysRevD.78.032007. http://link.aps.org/doi/10.1103/PhysRevD.78.032007.

[30] Hanlon, W.F.: 2008, The energy spectrum of ultra high energy cosmic rays measured by the high resolution fly's eye observatory in stereoscopic mode. PhD thesis, The University of Utah.

[31] Heitler, W.: 1954, *The quantum theory of radiation*, Courier Dover, N. Chemsford, MA.

[32] Hillas, A.M.: 1984, The origin of ultra-high-energy cosmic rays. *Astron. Astrophys. Rev.* **22**, 425 – 444.

[33] Hörandel, J.: 2006, Cosmic rays from the knee to the second knee: 10^{14} to 10^{18} ev. arXiv:astro-ph/0611387.

[34] Hörandel, J.R.: 2016, Radio detection of air showers with lofar and aera. In: *Proceedings of International Symposium for Ultra-High Energy Cosmic Rays (UHECR2014), id.010004, ¡NUMPAGES¿8¡/NUMPAGES¿ pp.*, 010004. doi:10.7566/JPSCP.9.010004.

[35] Huege, T., the LOPES Collaboration: 2008, Radio detection of cosmic ray air showers with the lopes experiment. *Journal of Physics: Conference Series* **110**(6), 062012. http://stacks.iop.org/1742-6596/110/i=6/a=062012.

[36] Jelley, J.V., Fruin, J.H., Porter, N.A., Weekes, T.C., Smith, F.G., Porter, R.A.: 1965, Radio pulses from extensive cosmic-ray air showers. *Nature* **205**(4969), 327 – 328. http://dx.doi.org/10.1038/205327a0.

[37] Kawai, H., Cheng, K.S., Engel, R., Ma, Y.Q., Pattison, B., Yao, Z.G., Zhu, Q.Q., Yoshida, S., Yoshii, H., Tanaka, K., Cohen, F., Fukushima, M., Hayashida, N., Hiyama, K., Ikeda, D., Kido, E., Kondo, Y., Nonaka, T., Ohnishi, M., Ohoka, H., Ozawa, S., Sagawa, H., Sakurai, N., Shibata, T., Shimodaira, H., Takeda, M., Taketa, A., Takita, M., Tokuno, H., Torii, R., Udo, S., Yamakawa, Y., Fujii, H., Matsuda, T., Tanaka, M., Yamaoka, H., Hibino, K., Benno, T., Doura, K., Chikawa, M., Nakamura, T., Teshima, M., Kadota, K., Uchihori, Y., Hayashi, K., Hayashi, Y., Kawakami, S., Matsuyama, T., Minamino, M., Ogio, S., Ohshima, A., Okuda, T., Shimizu, N., Tanaka, H., Bergman, D.R., Hughes, G., Stratton, S., Thomson, G.B., Endo, A., Inoue, N., Kawana, S., Wada, Y., Kasahara, K., Azuma, R., Iguchi, T., Kakimoto, F., Machida, S., Misumi, K., Murano, Y., Tameda, Y., Tsunesada, Y., Chiba, J., Miyata, K., Abu-Zayyad, T., Belz, J.W., Cady, R., Cao, Z., Huentemeyer, P., Jui, C.C.H., Martens, K., Matthews, J.N., Mostofa, M., Smith, J.D., Sokolsky, P., Springer, R.W., Thomas, J.R., Thomas, S.B., Wiencke, L.R., Doyle, T., Taylor, M.J., Wickwar, V.B., Wilkerson, T.D., Hashimoto, K., Honda, K., Ikuta, K., Ishii, T., Kanbe, T., Tomida, T.: 2008, Proceedings of the xiv international symposium on very high energy cosmic ray interactions telescope array experiment. *Nuclear Physics B - Proceedings Supplements* **175**, 221 – 226. doi:http://dx.doi.org/10.1016/j.nuclphysbps.2007.11.002. http://www.sciencedirect.com/science/article/pii/S0920563207007992.

[38] Kido, E., Kalashev, O.E., for the Telescope Array Collaboration, et al.: 2013, Constraining uhecr source models by the ta sd energy spectrum. *ArXiv e-prints*.

[39] Kotera, K., Olinto, A.V.: 2011, The astrophysics of ultrahigh-energy cosmic rays. *Ann. Rev. Astron. Astrophys.* **49**, 119 – 153. doi:10.1146/annurev-astro-081710-102620.

[40] Kuempel, D., Kampert, K.-H., Risse, M., *et al.*: 2008, Geometry reconstruction of fluorescence detectors revisited. *Astroparticle Physics* **30**, 167 – 174. doi:10.1016/j.astropartphys.2008.08.003.

[41] Letessier-Selvon, A., Stanev, T.: 2011, Ultrahigh energy cosmic rays. *Rev. Mod. Phys.* **83**, 907 – 942.

[42] Linsley, J.: 1963, Evidence for a primary cosmic-ray particle with energy 10^{20} ev. *Physical Review Letters* **10**, 146 – 148. doi:10.1103/PhysRevLett.10.146.

[43] Lipari, P.: 2014, The lifetime of cosmic rays in the milky way. *ArXiv e-prints*.

[44] Matthews, J.: 2005, A heitler model of extensive air showers. *Astroparticle Physics* **22**, 387 – 397. doi:10.1016/j.astropartphys.2004.09.003.

[45] Newton, D., Knapp, J., Watson, A.A.: 2007, The optimum distance at which to determine the size of a giant air shower. *Astroparticle Physics* **26**, 414 – 419. doi:10.1016/j.astropartphys.2006.08.003.

[46] Ptitsyna, K.V., Troitsky, S.V.: 2010, Physics of our days physical conditions in potential accelerators of ultra-high-energy cosmic rays: updated hillas plot and radiation-loss constraints. *Physics Uspekhi* **53**, 691 – 701. doi:10.3367/UFNe.0180.201007c.0723.

[47] Rieger, F.M.: 2008, Cosmic ray acceleration in active galactic nuclei - on centaurus a as a possible uhecr source.

[48] Samarai, A., Imen, Bérat, C., Deligny, O., Letessier-Selvon, A., Montanet, F.m.c., Settimo, M., Stassi, P.: 2016, Molecular bremsstrahlung radiation at ghz frequencies in air. *Phys. Rev. D* **93**, 052004. doi:10.1103/PhysRevD.93.052004. http://link.aps.org/doi/10.1103/PhysRevD.93.052004.

[49] Samarai, I.A., Deligny, O., Lebrun, D., Letessier-Selvon, A., Salamida, F.: 2015, An estimate of the spectral intensity expected from the molecular bremsstrahlung radiation in extensive air showers. *Astroparticle Physics* **67**, 26 – 32. doi:http://dx.doi.org/10.1016/j.astropartphys.2015.01.004. http://www.sciencedirect.com/science/article/pii/S0927650515000146.

[50] Sato, R.: 2011, Long term performance of surface detectors of the pierre auger observatory. In: *The Pierre Auger Observatory IV: Operation and Monitoring*.

[51] Schröder, F.G.: 2016, Radio detection of cosmic-ray air showers and high-energy neutrinos. *ArXiv e-prints*.

[52] Settimo, M., Pierre Auger Collaboration: 2016, Measurement of the mass composition of ultra-high energy cosmic rays with the pierre auger observatory. *Journal of Physics: Conference Series* **718**(5), 052037. http://stacks.iop.org/1742-6596/718/i=5/a=052037.

[53] Sharma, S.K.: 2008, *Atomic and nuclear physics*, Pearson Education, Upper Saddle, NJ.

[54] The Pierre Auger Collaboration: 2015, The pierre auger cosmic ray observatory. *ArXiv e-prints*.

[55] Unger, M., Dawson, B.R., Engel, R., Schüssler, F., Ulrich, R.: 2008, Reconstruction of longitudinal profiles of ultra-high energy cosmic ray showers from fluorescence and cherenkov light measurements. *Nuclear Instruments and Methods in Physics Research A* **588**, 433 – 441. doi:10.1016/j.nima.2008.01.100.

[56] Šmída, R.: 2011, First results of the crome experiment. *International Cosmic Ray Conference* **3**, 17. doi:10.7529/ICRC2011/V03/0177.

[57] Šmída, R., Werner, F., Engel, R., Arteaga-Velázquez, J.C., Bekk, K., Bertaina, M., Blümer, J., Bozdog, H., Brancus, I.M., Chiavassa, A., Cossavella, F., Di Pierro, F., Doll, P., Fuchs, B., Fuhrmann, D., Grupen, C., Haungs, A., Heck, D., Hörandel, J.R., Huber, D., Huege, T., Kampert, K.-H., Kang, D., Klages, H., Kleifges, M., Krömer, O., Link, K., Łuczak, P., Ludwig, M., Mathes, H.J., Mathys, S., Mayer, H.J., Melissas, M., Morello, C., Neunteufel, P., Oehlschläger, J., Palmieri, N., Pekala, J., Pierog, T., Rautenberg, J., Rebel, H., Riegel, M., Roth, M., Salamida, F., Schieler, H., Schoo, S., Schröder, F.G., Sima, O., Stasielak, J., Toma, G., Trinchero, G.C., Unger, M., Weber, M., Weindl, A., Wilczyński, H., Will, M., Wochele, J., Zabierowski, J.: 2014, First experimental characterization of microwave emission from cosmic ray air showers. *Physical Review Letters* **113**(22), 221101. doi:10.1103/PhysRevLett.113.221101.

[58] Waldenmaier, T.: 2006, *Spectral resolved measurement of the nitrogen fluorescence yield in air induced by electrons* **7209**, FZKA, ???.

[59] Williams, C.L.: 2013, A search for microwave emission from cosmic ray air showers. PhD thesis, University of Chicago. unpublished thesis.

[60] Williams, C.: 2012, Microwave detection of cosmic ray air showers at the pierre auger observatory, an r&d effort. *Physics Procedia* **37**, 1341 – 1348. doi:http://dx.doi.org/10.1016/j.phpro.2012.03.739. http://www.sciencedirect.com/science/article/pii/S1875389212018408.